Bio-inspired control concepts for elastic rotatory joint drives

PhD thesis submitted for the degree of

DOCTOR OF ENGINEERING

by

Salvatore Annunziata

Supervisor:

Prof. Dr. Axel Schneider

University of Bielefeld, Faculty of Technology

Reviewer:

Prof. Dr.-Ing. Ralf Möller

University of Bielefeld, Faculty of Technology

Bielefeld University
Faculty of Technology
Universitätsstr. 25
33615 Bielefeld
Germany

December, 2013

Bio-inspired control concepts for elastic rotatory joint drives

PhD thesis submitted for the degree of

DOCTOR OF ENGINEERING

by

Salvatore Annunziata

Supervisor:

Prof. Dr. Axel Schneider

University of Bielefeld, Faculty of Technology

Reviewer:

Prof. Dr.-Ing. Ralf Möller

University of Bielefeld, Faculty of Technology

Bielefeld University
Faculty of Technology
Universitätsstr. 25
33615 Bielefeld
Germany

December, 2013

Acknowledgments

The way that leads to complete a PhD is an amazing journey and I would not have been able to success in this adventure without the support of countless people over the past years.

I would like to express my deepest gratitude to my principal supervisor, Professor Axel Schneider, for guiding me during this time and inspiring me to explore far beyond my own expectations. As an excellent supervisor he has not given me ready solutions but hints that have made it possible for me to learn how to perform successfully research.

I also want to thank my second supervisor, Professor Ralf Möller, for showing his interest and for his assistance and guidance with this thesis.

Of course, I cannot forget my colleagues at the Biomechatronics Group. Filip Szufnarowski, Jan Paskarbeit, Daniel Basa and Mattias Schäffersmann, it was a pleasure to work with you guys. My sincere thanks also goes to Angelika Deister and Anja Lübke for their assistance and help in these years spent at the university.

I want to thank all my friends too for all their love and support over the years spent in Bielefeld.

Of course I give my deepest gratitude to my family, especially to my parents, for their endless love.

Last but not least, I want to thank Sara for being there whenever necessary and for her love, kindness and support she has shown during these years.

Bielefeld, 09.12.2013 Salvatore Annunziata

Bio-inspired control concepts for elastic rotatory joint drives

by
Salvatore Annunziata

Research Group *Biomechatronics*
Faculty of Technology
Bielefeld University
Universitätsstr. 25
33615 Bielefeld
Germany
December, 2013

ABSTRACT

Recent research in robotics focuses the attention on the control of compliant actuators to improve safety and to make the interaction with humans more natural. Lightweight construction, real elasticity directly integrated into the joint and control of joint compliance seem to play the most important role for improving safety in human-machine interaction. Humans are intrinsically elastic and the Central Nervous System (CNS) takes advantage of the nonlinear muscle properties to modulate joint stiffness through co-contraction of antagonistic muscles.
If alterable compliance in robotic systems is desirable, its introduction can be achieved in two fundamentally different ways. The first way is a technical approach based on the idea of impedance control as formulated by Hogan (1985). The second approach is bio-inspired and introduces physiological control mechanisms, muscle models and virtual antagonistic actuation into the control system of a robotics joint drive.

Recently, biological models for the control of muscles in vertebrates have been developed (Franklin et al., 2008; Yang et al., 2011). Still, the question remains, how a control algorithm, acting on two or even more muscles, can be implemented in a technical joint. With the objective to implement bio-inspired control strategies on a robotic joint drive, in this thesis, musculoskeletal models, biological parameters and bio-inspired control laws are analyzed and tested. A simplified model of the human elbow joint is used to analyze muscle-like actuation and stiffness properties at the joint. Based on recent results related to how the CNS controls antagonistic muscles, a biological control pattern based on reciprocal activation and co-activation is tested for the control of torque and stiffness at the joint. However, a closer analysis of the musculoskeletal parameters reveals that, despite antagonistic co-activation, domains in the joint range of motion might occur for which stiffness variation is limited (low stiffness variability) or even impossible (stiffness nodes).

The first part of this thesis presents novel strategies for simultaneous control of torque and stiffness in a hinge joint actuated by two antagonistic muscle pairs. One strategy handles stiffness nodes by shifting them away from the current joint position and thus regaining stiffness controllability. To prevent domains of low stiffness variation, an optimal biomechanical setup is sought and finally defined which allows for a maximal stiffness variation across a wide angular joint range. Based on this optimal setup, four additional control approaches are designed and tested in simulation which deliver stiffnesses and torques comparable to those obtained in the optimal case. The control approaches combine biologically justified aspects, like reciprocal activation and co-activation, with novel ideas like inverse dynamics model and activation overflow.

The second part of the thesis focuses on the design, test and validation of a bio-inspired position and stiffness control strategy for a lightweight, intrinsically elastic, robotics joint drive. Reciprocal activation and co-activation are used here as a starting point to concurrently control stiffness and position (instead of torque). A stability analysis, performed on the human elbow joint model, confirms that the co-activation level (and, as a consequence, the stiffness level) affects the reaction of the joint to external perturbations in terms of oscillations and settling time. To account for the stability aspects and implement further mechanisms found in the CNS of vertebrates, models of the muscle spindles, Golgi tendon organs, α-motor neurons and Renshaw cells, are added to the control algorithm.

Nevertheless, while in many biological systems, antagonistic muscles generate the movement of the joint, in simple robotic systems, the movement is generated by only one actuator. Therefore, in order to transmit the desired bio-inspired movement to the technical elbow, the sum of all muscle-torques acting on the joint (i.e. the net-torque at the joint), has to be transmitted to the lightweight, inherently elastic, joint drive and controlled. A speed-torque control cascade is designed, implemented and tested on the robotics joint drive.

The impedance range of the human elbow joint is evaluated in simulation and compared to the range obtained when the technical joint drive is acting instead of its biological counterpart. The bio-inspired controlled joint drive is able to reach the desired position and modulate joint compliance according to the disturbance like humans do, both in static cases and during movements, while keeping stability.

Table of Contents

Chapter 1

Introduction

Traditionally, the robotics community favors stiff joints for accurate and fast positioning tasks in perfectly known environments. Stiff robots, however, present a danger for humans when an interaction takes place. For robotics applications such as prostheses, rehabilitation devices, domestic and entertainment robots, the classical stiff actuation is inappropriate as it does not give or comply in a collision.
Biological systems are intrinsically elastic and are able to adjust the compliance (or its inverse, the stiffness) at the joint through co-activation of antagonistic muscles, i.e. pairs of muscles (or groups of muscles) that pull in opposite directions. With the objective to supply robotic joints with a similar compliant behavior, in this thesis the biological example is analyzed and biologically inspired control strategies are designed. Since the field of assistive robotic arms is broad, in this work we concentrate on two fundamental areas. The first is the area of **joint control**. Here the research is related to the control of compliant rotatory robotics joints. Though, while the control of a single physical parameter is simple (e.g. the joint position), the simultaneous control of torque (or position) and stiffness at the joint needs a more accurate analysis, which leads to the second fundamental area: **muscle biomimetics**. In this case the research is focused on the design and implementation of bio-inspired control concepts that feature muscle-like virtual antagonistic actuation. Starting from classical control approaches [such as impedance control (Hogan, 1985)], novel bio-inspired strategies are evaluated, tested and validated on a robotics joint prototype.

In many biological systems, antagonistic muscles generate the movement of the joint. In simple robotic systems, the movement is generated by only one actuator. Therefore, virtual muscles are integrated into the control system, to take advantage of their properties. Although biological models concerning the control of muscles in vertebrates have been developed (Franklin et al., 2008; Yang et al., 2011), still, the question remains, how a control algorithm acting on two or even more virtual muscles can be developed in a technical joint in order to perform like in biological systems.

On the way to find such a control algorithm, in this thesis the following questions are investigated:

- How can muscle-like actuation be achieved in a technical joint?
- What facets of the biological actuation system are of interest in order to accomplish a control task?

- How can the elasticity of an antagonistically driven joint based on virtual muscles be tuned?
- How can a system of virtual muscles be integrated into the control system of a robotic joint drive?
- What kind of technical control schemes can be adopted to control the virtual antagonistic system?

Muscle-like actuation and stiffness properties at the joint are analyzed adopting a simplified model of the musculoskeletal joint. Based on recent results related to how the central nervous system (CNS) controls the muscles, a biological control pattern is implemented for the activation of the virtual muscles. This pattern makes use of reciprocal activation (i.e. only one muscle is activated at a time) and co-activation (i.e. all antagonistic muscles are activated at the same time) and is adopted as base for all simultaneous torque (or position) and stiffness control presented in this work. It will be shown that the implementation of such a biological control pattern, coupled with a model of a musculoskeletal setup, allows the modulation of the stiffness at the joint. However, some limitations related to the selection of muscle and joint model parameters affect the behavior of the controller. In particular, the concept of stiffness nodes is introduced for which, despite muscle co-contraction, the stiffness variability results limited. Novel technical control schemes are designed and multi-muscle solutions are adopted in order to solve the problem. Finally, stability analysis and interaction tests on the robotics prototype demonstrate that the control strategy designed in this thesis fulfills the requirements.

In this chapter, the contributions of this work are outlined. Afterwards, a literature review of the different approaches which have been adopted over the past years to improve safety in the interaction between humans and robotic systems is discussed. Starting from classical stiff joint actuators, different solutions have been introduced for increasing the safety performances and realizing a compliant interaction. A further section is dedicated to the analysis of biological systems and to the recent research on bio-inspired control approaches as a basis for safe robot construction. The last section of this chapter illustrates the thesis organization.

Contributions of this work

People with upper and lower limb motor impairment and physical disabilities (e.g., caused by spinal cord injury or disease) and even elderly people with decreased movement capability need assistance to perform their daily tasks. As a consequence, an increasing number of caregivers are needed to help such people in their everyday life. The adoption of assistive robotic systems might improve the independence and the quality of life of these people and at the same time reduce societal costs. Therefore, in the last few years, the development of assistive robotic arms, prostheses and orthoses has

been gaining more and more popularity in the robotics community. Examples of recent artificial limbs are the Modular Prosthetic Limb (Johannes et al., 2011) and the Boston Digital Arm (Liberating Technologies, Inc., 2012).
With the objective to provide control schemes that can be adopted in applications which combine technical and biological systems in areas such as prosthetics and orthotics, in this work, the mechanical impedance of a robotic joint is analyzed and bio-inspired solutions for impedance control are evaluated. The use of these control approaches could be advantageous not only to make human-machine interaction more intuitive, for example when the actuators are used in prosthetic or orthetic devices, but also to make it safer.

The scientific results presented in this thesis contain material from already published papers (Annunziata et al., 2010, 2011; Annunziata and Schneider, 2012).
The original contributions can be grouped in four topics: (1) characterization of joint impedance in a biological system; (2) introduction of the stiffness node–concept; (3) evaluation of control strategies to achieve an optimal joint stiffness variation; (4) application of the bio-inspired impedance control on a robotic drive. A short comment on each of the original contributions is presented below.

Characterization of joint impedance in a biological system:
The first contribution of this thesis is a methodology to analyze the stiffness and viscosity at the joint of a biological system. It is based on the model of the musculoskeletal setup. This description allows to examine the joint stability properties and evaluate the mechanical impedance response of a virtual biological joint when coupled with a drive.

Introduction of stiffness nodes:
Generally, biological systems change joint stiffness through co-activation of antagonistic muscles. The second contribution is the detection of angular positions in the joint range of motion for which stiffness does not vary with co-activation. We called these points *stiffness nodes*. A mathematical description of the conditions of existence, the formulation of their position and their investigation for different musculoskeletal parameters is performed.

Evaluation of control strategies to achieve an optimal joint stiffness variation:
A third important contribution is directly related to the former one and refers to the evaluation of an optimal musculoskeletal setup to increase the joint stiffness variation for a wide angular range and the testing of different control laws to realize an optimal muscle activation pattern.

Application of the bio-inspired impedance control on a robotic drive:
With the objective to realize a robotics joint with improved safety characteristics for human-machine interaction, a control approach which combines technical and biological properties was implemented and tested in a real joint. The technical drive is a high-performance lightweight system with inherent elasticity. The fourth contribution made in this thesis is that the mechanical impedance at the joint is controlled by adopting nonlinear muscle models, virtual antagonistic actuation models and control laws which are found in the CNS of vertebrates. The output of the bio-inspired controller is the net-

torque of all virtual antagonistic muscles pulling at the joint. This net-torque is used as an input for the technical drive, which, controlled using cascade feedback control, generates the desired torque and reproduces the biological behavior.

1.1 Classical stiff actuators versus compliant robotics joints

Classical industrial robotics requires predominantly stiff actuators and rigid support structures to achieve high position accuracy and repeatability. Known as an "the stiffer, the better" approach, it guarantees high control bandwidth, reduced instability, high precision and is appropriate for tasks in which well-defined work must be realized in a known environment (i.e., pick-and-place procedures). For these setups, considerable attention has to be payed to the mechanical construction, taking into account both torsional and bending stiffness in joints and segments. As the movements are fixed and the environment known, a simple position control is usually adequate to realize the desired movement. In actual industrial production, robots are still confined to operate in cages. However, there are already some applications like polishing, welding and general peg-in-hole problems (Mason, 1981) in which robots are subject to external forces such as disturbances, collisions and interactions. In these situations, the performance of the controller is critical. For example, for robots that have to interact with unknown environments in order to complete a desired task, it would be necessary to have an accurate model of the environment for the development of the controller, which is actually difficult to obtain. Therefore, much of current robotic research has shifted its focus to robots which can be employed as interaction partners for humans e.g., in assistance, rehabilitation, domestic or entertainment (Honda, 2008; Vallery et al., 2008; Virk and Nyoman, 2013). Robots that share an environment with humans must fulfill different requirements from those typically found in industry. Especially with the objective to increase safety in the interaction between robots and humans, in the last thirty years, new control approaches referred to as *interaction control* (Chiaverini et al., 1999) have been developed, in which the robot's dynamic behavior can be selected according to the situation or kind of interaction.

Traditionally, safety in human-robot interaction was guaranteed by increasing the sensorization on the basis of real-time obstacle avoidance or prevention of collisions. An example is proposed by Cheung and Lumelsky (1989) in which proximity-sensitive skin sensors were adopted. Other approaches are based on the implementation of stiffness control strategies to change the compliance at the joint, and are based on the concept of impedance as formulated by Hogan (1985). In impedance control, the desired interaction with the environment of the robot Tool Center Point (TCP) is modified according to a mass-spring-damper equation until the desired dynamic behavior between end-effector and the external force acting on the link is reached. Therefore, it is necessary to sense external forces in the environment in order to develop a control law that facilitates a

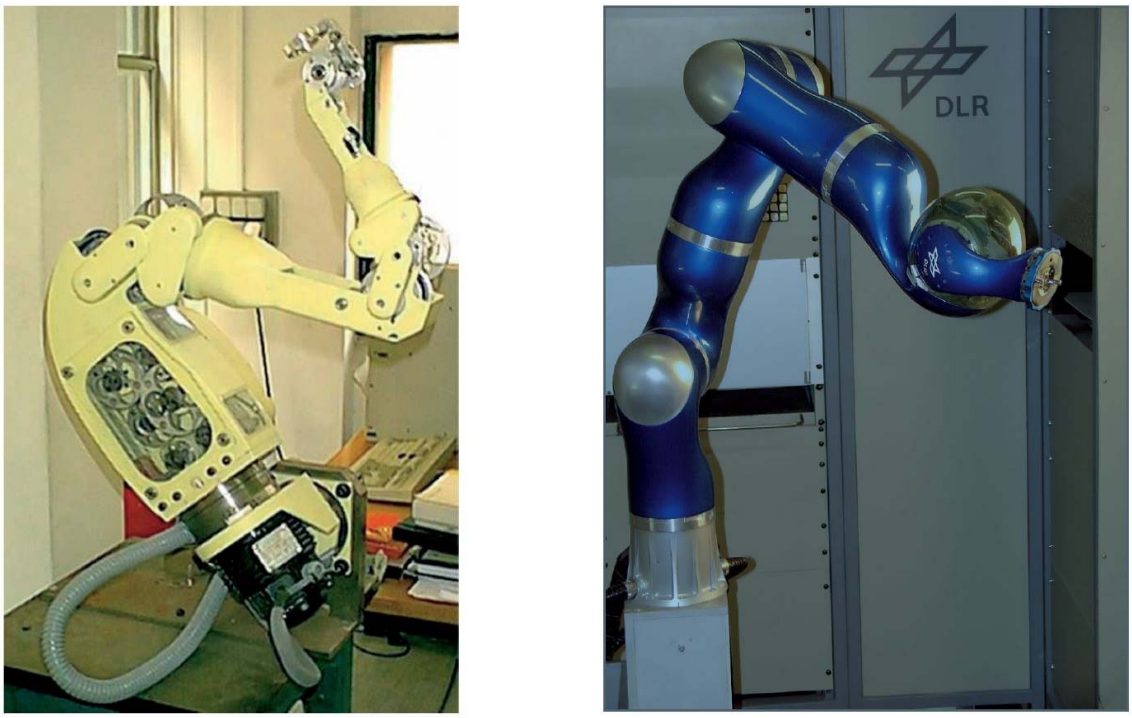

(a) (b)

Fig. 1.1: Examples of first attempts to obtain compliant robots [figures from (Siciliano and Khatib, 2008), p. 288-289; reproduced with permission of the publisher]. (a) The cable-driven anthropomorphic robot arm Dexter, manufactured by Scienza Machinale s.r.l. (Pisa, Italy) and designed for applications of assistance robotics. (b) The DLR LWR-III mounts torque sensors to close the torque control loop and to control the compliance at the joint.

desired interaction behavior. A simple approach to estimate the torque could be to measure the motor current, taking advantage of the torque-current proportional relationship of DC-motors. Figure 1.1(a) shows an example of a robot manipulator in which the compliance at the joints is controlled using the measurement of the motor current (Zollo et al., 2003). However, motor torque is not the same as joint torque as the first does not take into account the nonlinearity in the gearbox. A better way to control the joint torque is its direct measurement using a torque sensor (Readman, 1994). In the last fifteen years, many robots have been equipped with a torque sensor. Integrated between the gearbox output and the load, the torque sensor allows the implementation of joint torque–feedback control laws and feedback–linearization strategies in order to compensate for the nonlinearity and friction effects present in the drive and in the gearbox. Moreover, the feedback of the torque measured on the output side of the joint improves the rejection of disturbances. This method is used mostly in systems where an actuator is driving a joint using a large gear ratio. An example is the DLR lightweight robot LWR-III [shown in fig. 1.1(b)] (Albu-Schäffer et al., 2007) in which the controller

allows desired position and stiffness to be set while robot operation remains stable at all times. Aside from the additional weight of the sensor and its electronics, the drawback of such a strategy is that the compliance is mimicked by control. An exclusively feedback based controlled elasticity (called *active compliance*) could represent still a danger during interactions in cases of outage, control errors, etc. Furthermore, it provides the desired compliance characteristics only in a limited frequency range: the control bandwidth (i.e. the range of frequencies for which controllable compliance can be achieved with rigid joints), is limited due to control loop delay and time delay in the sensor data acquisition. These types of actuators are therefore intrinsically stiff and not suitable for human-robot interaction.

Ensuring safe interaction is extremely important in the construction and control of a robot. However, safe behavior is not a unit that is directly measurable. In the absence of such a quantity, several safety criteria have been defined in literature. An example is the Head-Injury-Criteria (HIC) index. Developed by the automotive industry to correlate head acceleration to injury severity, the HIC-index has been adopted since 2004 in the field of robotics and is used to provide an estimation of the resulting injury, should a human head come into contact with a robotic manipulator, and to asses safety properties (Zinn et al., 2004). Taking into account the robotics arm effective inertia and its covering material (interface stiffness), the HIC-index indicates that a lightweight construction and the introduction of real elasticity (or *passive compliance*) into the joint are good candidates for improving safety (see fig. 1.2). Passive compliant actuators with at least one physical elastic element integrated into the joint provide intrinsic compliance and reduce the risk for the user when an impact takes place, at a cost of lower high-speed positioning accuracy and lower control bandwidth. Different technical actuation systems and control approaches have been proposed and developed which realize joint compliance with the integration of elastic elements.

Pratt and Williamson (Pratt and Williamson, 1995), with their Serial Elastic Actuator (SEA), were among the first to introduce real serial elastic elements into a robotics joint drive for generating passive compliance. In SEAs, the elastic element limits the high-frequency impedance of the actuator to the stiffness of the elastic coupling. Furthermore, the spring stiffness is constant, and as a consequence, the mechanical output position of the joint drive cannot be independently controlled. Variable Stiffness Actuators (VSAs) were developed with the objective to control the position and stiffness separately. They use two actuators, typically mounted in an antagonistic configuration, in combination with an elastic element. Numerous VSAs have been proposed by the robotics community. For example, Tonietti and co-workers adopted two DC motors and a belt tensioned by springs (Tonietti et al., 2005). Hurst et al. (2004) proposed an actuator with adjustable serial compliance by using an additional actuator in the joint drive mounted in an antagonistic setup. Migliore et al. (2005) used a nonlinear spring mechanism to mimic muscle behavior and to realize independent control of joint angle and stiffness. In the area of technical, antagonistic actuation, also pneumatic actuators were used to implement variable compliance based on their inherent nonlinear elasticity (Daerden and Lefeber, 2001). An example of simultaneous torque and stiffness con-

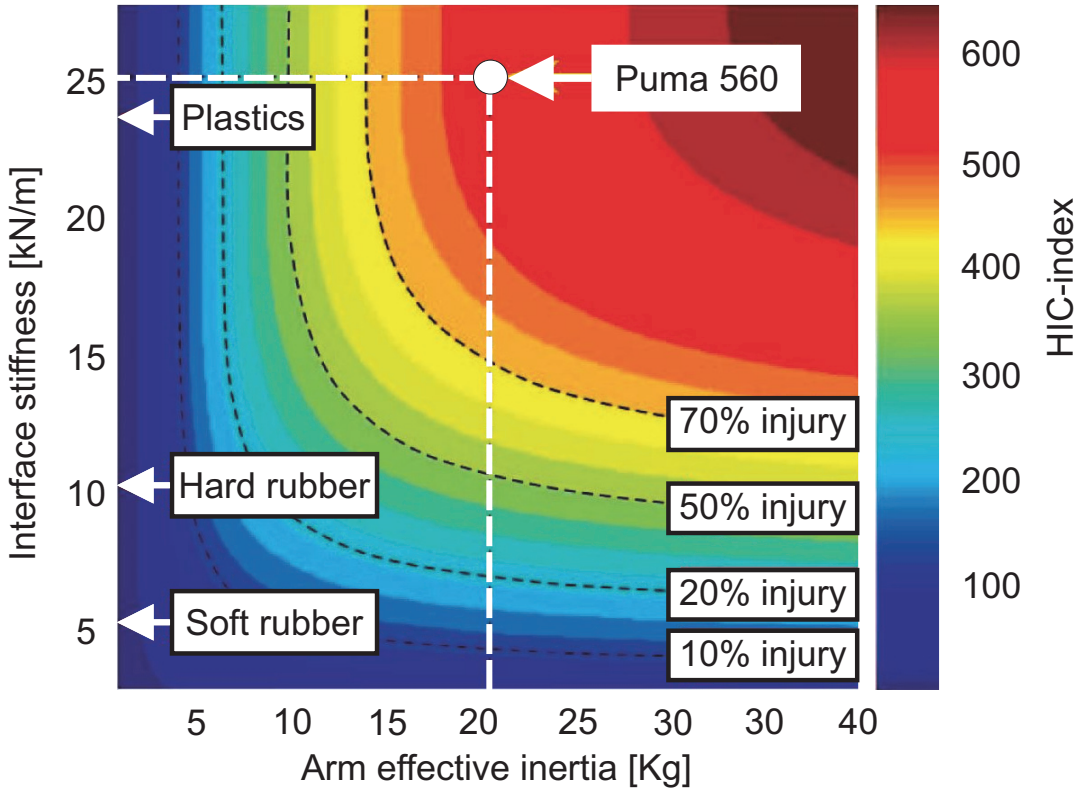

Fig. 1.2: Head-Injury-Criteria index as found by Zinn, 2004 [figure from (Zinn et al., 2004), used with author's permission]. As example an impact velocity of 1 m/s for the robot PUMA 560 produces a maximum HIC greater than 500 which corresponds to a serious injury.

trol for pneumatic actuators is provided by Sardellitti et al. (2010). Recently, further design solutions have been proposed to change the intrinsic stiffness of the elastic (or passive) element. Some designs are based on the adjustment of its fixation point into the drive, like in the Actuator With Adjustable Stiffness (AWAS) (Sardellitti et al., 2012). Groothuis et al. (2012), presented a novel mechanism based on mechanical springs, in which the spring-stiffness can be varied by setting its effective lever arm length. Nevertheless, these solutions are difficult to miniaturize as they require at least a second actuator and the construction of complex mechanisms. Furthermore, the introduction of passive compliance into the joint could induce oscillations of the output link. In order to actively modulate the impedance of the drive and reduce those oscillations, Laffranchi and co-workers introduced an actuation system (CompaAct™) which integrates passive compliance and a novel Variable Physical Damping Actuator (VPDA) unit (Laffranchi et al., 2011). A robotic arm (CompAct Arm) was recently developed based on this actuator (Laffranchi et al., 2012).

1.2 From biological systems to safe robots

Many biological systems present three important properties: (1) they are antagonistically actuated; (2) they integrate intrinsic elastic elements, the muscles; (3) and they are able to modulate joint impedance with respect to the task requirements, e.g., during interactions with unknown environments.
Integrated into the antagonistic setup, each muscle is connected to the skeletal apparatus via tendons and is embedded within soft tissue, thus acting both as actuator and as passive compliance. The muscles and the skeletal structure form the musculoskeletal setup, which results in a high order nonlinear elastic actuation system with many parameters and degrees of freedom even at the joint level for a potential controller. The combination of feedback signals such as interaction forces, joint position and velocity, together with the neural commands to the muscles play a fundamental role for the regulation of joint mechanical impedance. Antagonistic actuation by at least two muscles leads to an additional degree of freedom for the control of the joint i.e. the same joint torque can be achieved by different muscle activations. The CNS uses the additional degree of freedom to set the joint torque and the stiffness independently in a certain parameter range by co-activation of the antagonistic muscles (Hogan, 1984). To be able to change joint stiffness by means of co-activation, the antagonistic actuators must act as nonlinear springs, since the stretching of antagonistically operating linear springs in a rotatory joint does not change the joint stiffness (Migliore et al., 2007). Biological muscles represent such an actuator. Humans, for example, are able to shift their operational mode from stiff (e.g. when performing delicate brain surgery) to fully backdriveable (e.g. while throwing a ball or to prevent muscle damage due to overload). Furthermore, studies on humans interacting with the environment (e.g., when using tools) have shown that instabilities might arise. In these cases, the CNS is responsible both for controlling the movement and adequately stiffening the joint (thus reaching robust stability). Again, this performance is achieved through co-activation of antagonistic muscles (Gribble et al., 2003; Suzuki et al., 2001).

In the last fifteen years, an interdisciplinary science called *biomechatronics* has seen rapid growth. In biomechatronics, the objective is to improve the construction and control of mechatronics systems through the implementation of bio-inspired control approaches and the adoption of construction principles as found in biological examples. The fundamental idea in this thesis is that the observation of the biological example and the adoption of physiological control mechanisms based on muscle models can lead to successful solutions in the area of mechatronics. Chou and Hannaford (1997) were among the first to apply knowledge of human physiological motion control in robotics. Their antagonistic pneumatic actuators acted as elbow flexor and extensor and were controlled by artificial neural networks that were based on physiological laws. Over the last few years, many studies have focused on the implementation of impedance control strategies based on neuromuscular models with optimization algorithms and learning processes to improve safety in human-machine interaction. Burdet et al. (2006) and Hoult and Cole (2008) proposed an algorithm to estimate feed-forward signals due to

external forces adopting internal models of human motor control. Franklin et al. (2008) introduced a motor learning algorithm that made deductions based on observations in psychophysical experiments. Using feedback loops and feed-forward signals, the motor commands were iteratively adjusted based on a V-shaped learning function. Mitrovic et al. (2009) adopted an antagonistic setup where the control of the joint impedance during reaching tasks was achieved through optimization of a cost function based on the position error. The result was a formalization of internal models for minimization of energy consumption. In all these works, the muscles were modeled as linear spring-damper systems in which the stiffness and damping vary as a function of activation.
In this thesis we adopt a different approach to realize a bio-equivalent technical actuation system, by using nonlinear muscle models and models of physiological properties of biological systems.

1.3 Thesis organization

This thesis is divided into six chapters and is organized as follows.

Chapter 2 presents the musculoskeletal joint setup and its mathematical model. Furthermore, the relevant concepts related to muscle actuation such as co-activation, reciprocal activation, joint stiffness, torque generation and mechanical impedance properties are illustrated. With the objective to control torque (or position) and stiffness at the joint, a mathematical analysis of the stiffness provides the basis for the choice of relevant control schemes.

In **Chapter 3** several concurrent torque/stiffness control strategies are developed and their effectiveness is tested in numerical simulations in Matlab/Simulink. An optimization is performed to find the muscle configuration which results in the maximal stiffness variation across the angular working range of motion.

Chapter 4 is dedicated to the design of a novel position and stiffness control strategy that takes advantage of virtual antagonistic actuation using nonlinear muscle models and physiologically based control laws. This strategy features antagonistic muscle co-activation and adaptive regulation of joint compliance. Section 4.1 provides the analysis of the stability properties of the joint for increasing co-activation. The proposed control schema is able to adapt impedance to the interaction task with the objective to increase stability (Section 4.2).

In **Chapter 5** a lightweight rotatory robotics joint drive is presented. The integrated passive elasticity with inherent damping characteristic, in the form of an elastomer coupling, ensures intrinsic joint compliance. The measure of its torsion allows the estimation of the load torque, which in turn, is used for control purposes. A cascade feedback control strategy is designed by modeling the drive in Matlab/Simulink and is then tested on the robotics joint prototype. The bio-inspired control approach is applied

to the drive. Its effectiveness is tested first in simulation and then validated on the real drive.

This thesis is concluded in **Chapter 6** with a summary of the main results achieved in this thesis and by extending them with a discussion of their possible implications. Finally we discuss possible future avenues for research in this area.

Chapter 2

Mechanical impedance properties of muscle-joint systems

This thesis concentrates on the design of bio-inspired control concepts for the modulation of the impedance in robotic joints. The mechanical impedance is a measure of how much a system resists to movement when subjected to an external force. This chapter deals specifically with the analysis of the mechanical impedance properties related to musculoskeletal joint setups. A musculoskeletal setup is composed of a joint geometry and at least two antagonistic muscles pulling at the joint. The mechanical impedance at the joint is analyzed and concepts such as stiffness and viscosity are separately considered. Starting from studies which revealed that biological systems are able to change joint stiffness by co-activation of antagonistic muscles, we show that in dependence of certain muscle and joint parameters, positions in the angular joint space can be found for which different levels of co-activation do not generate any change in stiffness (*stiffness nodes*). Consequently, for joint positions in the vicinity of such nodes, any stiffness controller would be expected to fail. After a mathematical analysis of the conditions for which stiffness nodes occur, we show that it is possible to predict the node positions. The musculoskeletal model proposed here captures the key complexities of biological systems while preserving a framework that is sufficiently abstract to facilitate computational studies of the overall control problem. The implications of more detailed biological joint models, more realistic joint geometries and additional muscles characteristics (Gaussian force-length curve and compliant tendons) are also investigated.

2.1 Musculoskeletal joint setup

A musculoskeletal system is made up of pairs of muscles, a skeletal structure (or geometry), tendons, ligaments, joints and other tissues that support and bind the organs together. Muscles exist in pairs because each single muscle, by contracting, generates a pulling force on the structure at which is connected but can not exert a pushing force. Therefore, a second muscle which pulls in opposite direction is needed. This framework composed by muscles arranged in opposing groups around a joint is called antagonistic muscle-joint setup. With the objective to obtain a mathematical model of an antagonistic muscle-joint setup, first the Hill-type muscle model is revisited and

its mathematical description is provided, then different antagonistically actuated joint geometries are evaluated. In order to model a human elbow joint, a hinge geometry with a pulley, driven by two antagonistic muscles, is adopted.

2.1.1 Hill-type muscle model

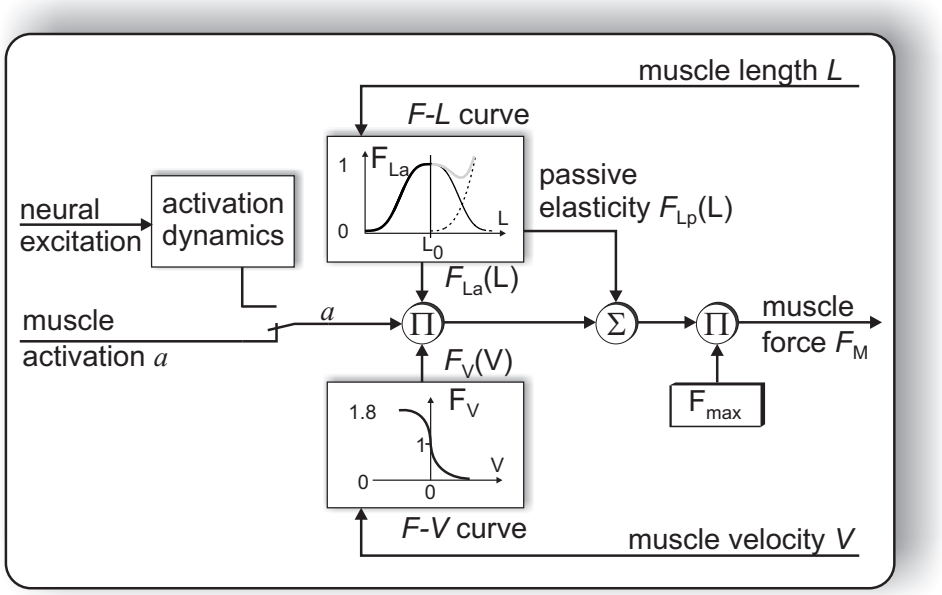

Fig. 2.1: Hill-type muscle model.

The force generated by a muscle can be estimated by using the Hill-type muscle model (Hill, 1938; Zajac, 1989), which is widely used in the context of experimental movement science [see e.g. Geyer et al. (2003)]. In this model, shown in fig. 2.1, the force produced by a muscle depends on the muscle activation a, and varies with muscle sarcomere length L and with the velocity V at which the muscle contracts or lengthens. Simpler linear muscle models such as those proposed by Hogan (1984) are not suited since they omit important details (like muscle nonlinear force-length relationship) that lead to the effects described in this study. Models such as the λ-model (Feldman, 2008) take a whole-system approach by observing the complete functionality of a limb with reflexes and control overhead included. This perspective again disguises the low-level effects discussed in this thesis.

In biological systems, muscle activation is a low-pass filtered neural input to the muscles (activation dynamics). However, in this work, this phenomenon is omitted. Instead, the activation is considered to be a normalized value in the range [0...1] corresponding to the output of a simultaneous torque (or position) and stiffness control process described in Chapter 3 and Chapter 4. The addition of a first-order excitation-activation dynamics would have the effect of delaying the muscle contraction slightly, thus prolonging the

Table 2.1: Overall muscle force and force functions as adopted in the Hill-type muscle model.

	Description	Unit
F_{M}	overall force output of the muscle model	N
$F_{\mathrm{La}}(L)$	norm. active force-length function	dimensionless
$F_{\mathrm{Lp}}(L)$	norm. passive force-length function	dimensionless
$F_{\mathrm{V}}(V)$	norm. force-velocity function	dimensionless
$\mathrm{F_{max}}$	maximum muscle force	N

time it takes to occur and lowering the muscle shortening velocity (Buchanan et al., 2004). For the tasks analyzed in this study, these effects can be neglected with little loss of accuracy. Furthermore, for simplification purposes, in this study, the nonlinear behavior of tendons is not considered. Instead, a serial elastic element of high stiffness is assumed as tendon (Gribble et al., 1998; Zajac, 1989). The consequences of this assumption are discussed in Section 2.3.5.

For the mathematical description of the muscle model, the muscle force-length dependency is divided into an active and a passive component.

Therefore, the overall time varying muscle force F_{M} can be mathematically described as

$$F_{\mathrm{M}} = \left[F_{\mathrm{La}}(L)\, F_{\mathrm{V}}(V)\, a(t) + F_{\mathrm{Lp}}(L)\right] \mathrm{F_{max}} \tag{2.1}$$

where $F_{\mathrm{La}}(L)$ is the active length-dependent force component, $F_{\mathrm{V}}(V)$ is the velocity-dependent force component and $F_{\mathrm{Lp}}(L)$ is the passive length-dependent force component. All functions are normalized to a maximum isometric muscle force $\mathrm{F_{max}}$ (see Table 2.1), optimal muscle length $\mathrm{L_0}$ (length at which the active muscle force reaches its maximum) and maximum shortening velocity $\mathrm{V_{max}}$.

The analytical expressions of the functions are approximations of the dimensionless curves adopted by Zajac (1989). The active length dependent force, F_{La}, generated by the contractile elements of muscle fibers can be approximated with several mathematical expressions[1]. In this thesis, a Gaussian (subscript G) and a quadratic (subscript q) version of the active force-length relationship are used. The Gaussian version guarantees a smooth transition to zero forces whereas the quadratic version shows an abrupt transition. Both versions are commonly used to represent the force-length relationship of a muscle and their expressions are

$$F_{\mathrm{LaG}}(L) = exp\left[\mathrm{c}\left|\frac{L-\mathrm{L_0}}{\mathrm{w\,L_0}}\right|^3\right], \text{ and} \tag{2.2}$$

$$F_{\mathrm{Laq}}(L) = \begin{cases} 1-\left(\frac{L-\mathrm{L_0}}{\mathrm{w\,L_0}}\right)^2 & |L-\mathrm{L_0}| < \mathrm{w\,L_0} \\ 0 & \text{otherwise} \end{cases}, \tag{2.3}$$

[1]This curve is often modeled as a second-order polynomial (Woittiez et al., 1984) or Gaussian (Geyer et al., 2003), although it is actually a bit more complex than those.

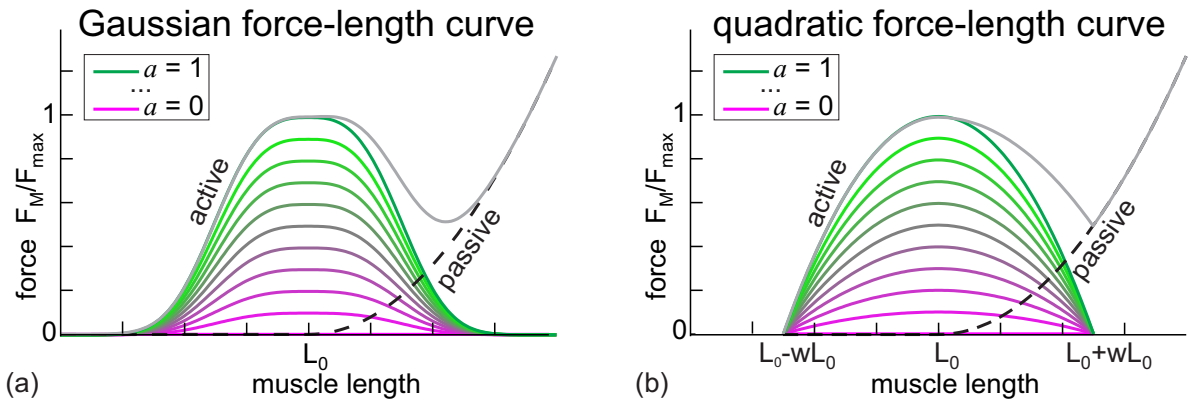

Fig. 2.2: (a) Active muscle force generated with a Gaussian force-length curve for different activations. The passive curve is depicted as a dashed line. For the maximum activation, the sum of passive and active forces (topmost curve) is shown. (b) Same as (a) but using a quadratic force-length curve.

where $c = \ln(0.05)$ [fulfilling $F_{\mathrm{LaG}}(\mathrm{L_0}(1 \pm \mathrm{w})) = 0.05$] and $2\,\mathrm{w}\,\mathrm{L_0}$ is the width of the active muscle curve (Geyer et al., 2003). The region in which active muscle force is generated is often assumed to range from $\sim 0.5\,\mathrm{L_0}$ to $\sim 1.5\,\mathrm{L_0}$ (corresponding to $\mathrm{w} \cong 0.5$) (Burkholder and Lieber, 2001).

The passive force component, related to titin molecules, generates a nonlinear, length-dependent restoring force independent of the muscle activation and is described by the following equation

$$F_{\mathrm{Lp}}(L) = \begin{cases} \mathrm{K_p}\,(L - \mathrm{L_0})^2 & L \geq \mathrm{L_0} \\ 0 & \text{otherwise} \end{cases}, \tag{2.4}$$

where the parameter $\mathrm{K_p}$ changes the curvature of the curve (Zajac, 1989).

Figure 2.2 depicts the active force-length curve modeled with the Gaussian (a) and quadratic (b) relations respectively, for different activations. In gray the active muscle force along with the passive component for maximum activation (a=1) is depicted. The active force follows the tension-length behavior of the sarcomere and scales with muscle activation. The passive force is negligible for lengths less that the normal resting length $\mathrm{L_0}$ and then starts to rise for growing muscle lengths.

The force-velocity dependency is approximated with the following function

$$F_{\mathrm{V}}(V) = \begin{cases} \frac{\mathrm{V_{max}} - V}{\mathrm{V_{max}} + \mathrm{K_v}\,V} & V > 0 \\ \mathrm{N_n} + (\mathrm{N_n} - 1)\,\frac{\mathrm{V_{max}} + V}{7.56\,\mathrm{K_v}\,V - \mathrm{V_{max}}} & V \leq 0 \end{cases} \tag{2.5}$$

where the constant $\mathrm{K_v}$ regulates the curvature and $\mathrm{N_n}$ corresponds to the normalized force value reached for $V = -\mathrm{V_{max}}$ (Geyer et al., 2003). For V=0 the force F_{V} is 1.

Figure 2.3 depicts the normalized muscle force as a function of normalized muscle length and shortening velocity for maximum activation. The passive force component is responsible for high restoring forces when the muscle is stretched. In the main operative

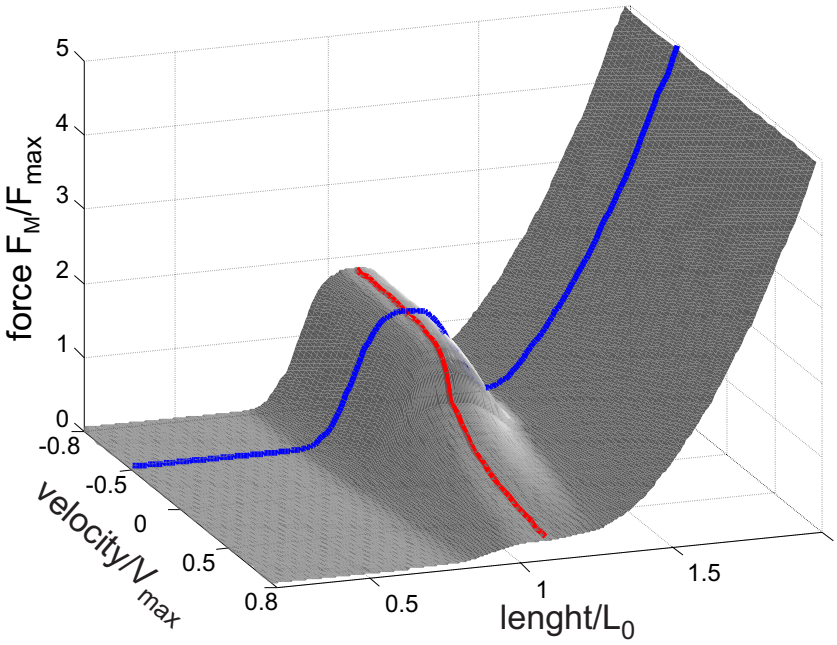

Fig. 2.3: Normalized muscle force F_{M} generated for maximum activation ($a = 1$) plotted over different normalized shortening velocity and normalized muscle length. As example, the normalized force-velocity curve plotted against the muscle resting length is depicted in red. The force-length curve for V/V_{max}=−0.5 is depicted in blue.

muscle range, the greatest force is produced when the lengthening is close to the resting length. In addition, force is greater during lengthening (increasing negative velocities) than shortening contractions (increasing positive velocities). Any movement in the figure corresponds to a "walk" on that surface. In red the force-velocity curve plotted against the muscle resting length (length/L_0=1) is depicted. The blue line represents the force-length curve for $V/\mathrm{V}_{\mathrm{max}} = -0.5$.

2.1.2 Antagonistic joint geometries with two muscles

The mechanical action of a muscle at joint level depends on its anatomical orientation with respect to the center of rotation of the joint. Each muscle produces a torque, product of the force F_{M} and its moment arm, i.e. the distance from the point of force application to the axis of rotation. For some joint setups this moment arm is constant, in others the moment arm varies as a function of the skeletal configuration or geometry. The simplest joint geometry is a one-degree-of-freedom (DoF) rotational hinge joint, like the elbow and interphalangeal joints. These joints allow movements back and forth in only one plane. Since the contraction of muscles develops unidirectional pulling forces, to move a lever around the joint in opposite directions, at least two antagonistic muscles are necessary. Figure 2.4(a) shows a simple hinge joint setup with a pulley. In this case,

the radius r of the pulley is the lever arm at which the muscles pull and it remains constant during joint rotation.
A closer approximation to biological musculoskeletal setups is depicted in fig. 2.4(b). The distances r_1 and r_2 between the attachment points of the muscles to the skeletal structure and the center of rotation are fixed but the moment arms at which the muscles pull are a function of the joint angle.

2.1.3 Simplified model of the human elbow joint with a pulley

In this work, a simplified version of the human elbow joint is used as a biological reference. We assume that the forearm is moved by only two antagonistic muscles which are pulling upon the elbow joint. Figure 2.5(a) shows the simplified human arm with the elbow joint that is moved by two antagonistic muscles (*muscle* 1 is the extensor and *muscle* 2 is the flexor). The joint range of motion is depicted with a dashed arc. In order to characterize stiffness and viscosity at the joint and later to test a concurrent control of position and stiffness, a model of the biological system has to be defined. A suitable model of the human elbow can be described by a hinge joint with a lever and two muscles. A simple hinge joint geometry with a pulley [as shown in fig. 2.4(a)] is used for the arm. Therefore, the moment arm for all the muscles acting on the joint corresponds to the radius r of the pulley. The use of constant moment arms is a simplification that allows a closed mathematical description of stiffness and is consistent with the assumptions made by, e.g., the models of Gribble et al. (1998). For parameter fitting of muscle data it can be assumed that this assumption degrades by 30% over a movement range of 1.66 rad (Murray et al., 1995). However, in this thesis the simple constant moment arm is used in the interest of simplicity. Figure 2.5(b) shows the antagonistic pulley wheel actuated by two muscles. The joint angle α is defined as $\alpha_0 = 0$ when the

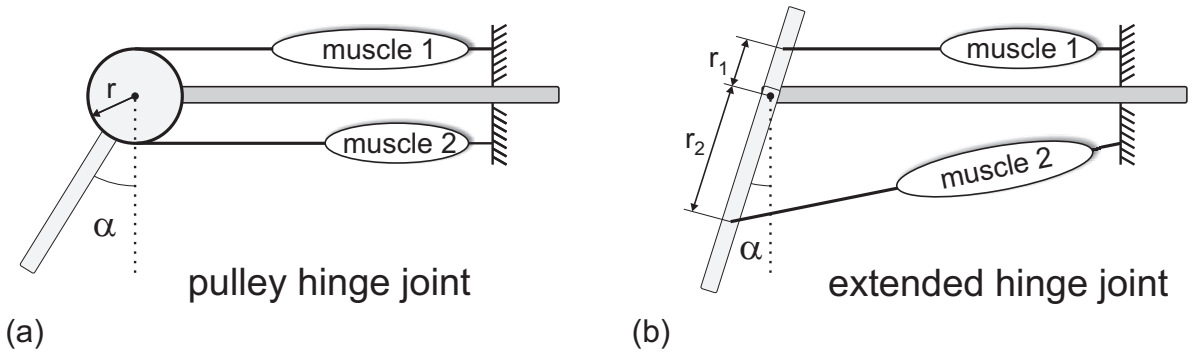

Fig. 2.4: (a) Simplified antagonistic hinge joint geometry with two muscles acting on a pulley. The moment arm is the same for both muscles and remains constant during the lever arm movement. (b) Extended antagonistic hinge joint geometry. The muscle attachment points to the structure are such that the two moment arms are different and vary as a function of the joint angle.

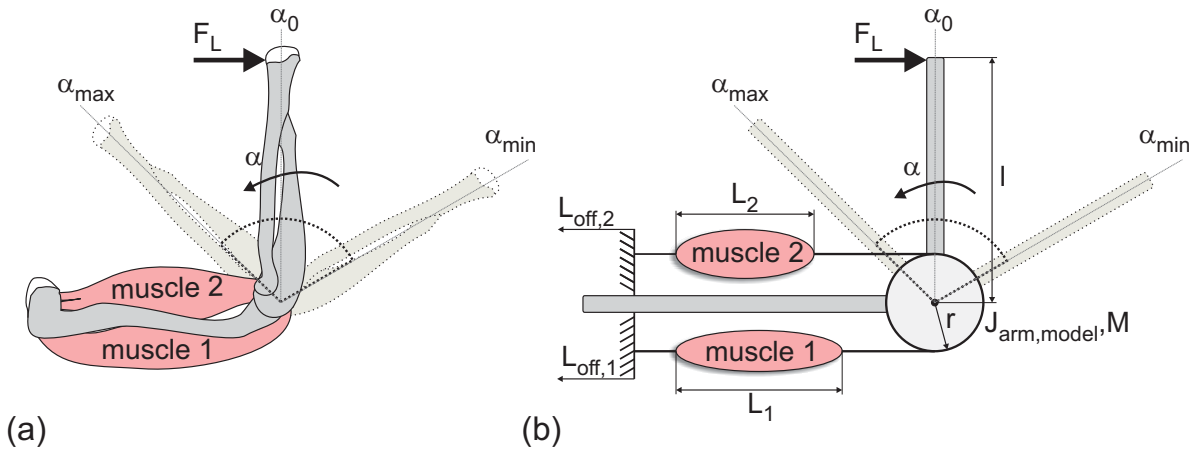

Fig. 2.5: (a) Simplified depiction of a human arm with the elbow joint moved by two muscles. (b) Two muscles in a simple hinge joint setup which uses a pulley. L_1 and L_2 are the muscle lengths. The values $\mathrm{L_{off,1}}$ and $\mathrm{L_{off,2}}$ indicate the possible pre-stretch that can be set for the muscles when integrated into the setup.

forearm is in the vertical position and the joint range of motion is limited to:

$$\alpha_{\min} \leq \alpha(t) \leq \alpha_{\max}$$

with $\alpha_{\min} = -\frac{\pi}{3}$ rad and $\alpha_{\max} = \frac{\pi}{4}$ rad. L_1 and L_2 are the muscle lengths. The region in which active muscle force is generated depends on the sarcomere length operating range, which varies according to the species. $\mathrm{L_{off,1}}$ and $\mathrm{L_{off,2}}$ represent offset lengths of the two muscles that allow the muscle insertion into the joint in a pre-stretched or loosened way. Therefore, these offset parameters can be used to adjust the operating range of the muscles with respect to the angular range of the joint.
The muscles are modeled based on the Hill-type model. When the lever arm moves, whether due to the action of the contracting muscle, the action of the other muscle, or to external forces, the muscles connected to that joint are subject to a change in length ΔL which depends on the joint angle α. In addition, each muscle is subjected to the pre-stretch value $\mathrm{L_{off}}$. Both length changes are deviations from the muscle resting length $\mathrm{L_0}$. Therefore, for each muscle, the effective deviation ΔL_{eff} of the muscle length from the resting length $\mathrm{L_0}$ can be written as (positive direction of movement is counterclockwise):

$$\begin{aligned} \Delta L_{\mathrm{eff},1} &= \Delta L_1 + \mathrm{L_{off,1}} \quad \text{with} \quad \Delta L_1 = \mathrm{r}\,\alpha \\ \Delta L_{\mathrm{eff},2} &= \Delta L_2 + \mathrm{L_{off,2}} \quad \text{with} \quad \Delta L_2 = -\mathrm{r}\,\alpha \quad . \end{aligned} \tag{2.6}$$

Furthermore, for the given setup, the following relations between shortening velocity of *muscle* 1 and *muscle* 2 and the joint angular velocity $\omega = \dot{\alpha}$ hold:

$$\begin{aligned} V_1 &= -\mathrm{r}\,\omega \\ V_2 &= \mathrm{r}\,\omega \quad . \end{aligned} \tag{2.7}$$

The hinge joint setup presented above, along with the muscle model introduced in Section 2.1.1, is used for the analysis of the joint stiffness and its dependence on different parameters of the joint-muscle setup.

The product $\mathrm{w\,L_0}$ in Equations (2.2) and (2.3) will always turn up as a pair. For the sake of simplicity, this product is therefore rewritten as one parameter $\mathrm{w_{L0}}$. The same holds true for the difference $L - \mathrm{L_0}$ in Equations (2.2), (2.3) and (2.4) which is replaced by ΔL_{eff}. As a consequence, the force-length relationship in *Gaussian* and *quadratic* form can be rewritten as:

$$F_{\mathrm{LaG}}(\Delta L_{\mathrm{eff}}) = exp\left[\mathrm{c}\left|\frac{\Delta L_{\mathrm{eff}}}{\mathrm{w_{L0}}}\right|^3\right] \tag{2.8}$$

$$F_{\mathrm{Laq}}(\Delta L_{\mathrm{eff}}) = \begin{cases} 1 - \left(\frac{\Delta L_{\mathrm{eff}}}{\mathrm{w_{L0}}}\right)^2 & |\Delta L_{\mathrm{eff}}| < \mathrm{w_{L0}} \\ 0 & \text{otherwise} \end{cases}, \tag{2.9}$$

and similarly the passive curve can be written as:

$$F_{\mathrm{Lp}}(\Delta L_{\mathrm{eff}}) = \begin{cases} \mathrm{K_p}\,(\Delta L_{\mathrm{eff}})^2 & \Delta L_{\mathrm{eff}} \geq 0 \\ 0 & \text{otherwise}. \end{cases} \tag{2.10}$$

For the simplified bio-inspired elbow joint model, several physiological parameters have to be selected. In this thesis, the parameters for both the arm model and the muscle model are obtained either directly from the literature or selected in order to match empirical data (as in the case of joint stiffness and viscosity). The physical parameters of the setup have been obtained from Katayama and Kawato (1993), Bennett et al. (1992) and Lacquaniti et al. (1982) and are reported in Table 2.2 (where the length of the moment arm r corresponds to the average value of anatomical data).
Referring to fig. 2.5(b), the lever is considered to be a uniform stick so that its center of mass is at the geometrical center. M is the mass of the lever arm concentrated in the center of gravity and l is the distance from the end of the lever to the axis of rotation

Table 2.2: Joint parameters for the antagonistic setup.

Variable	Description	Value	Unit
r	pulley radius	0.03	m
$\mathrm{J_{arm,model}}$	moment of inertia	0.06125	$\mathrm{kg\,m^2}$
M	mass lever arm	1.5	kg
l	length lever arm	0.35	m
$\mathrm{K_{max}}$	max joint stiffness	35[1]	Nm/rad
$\mathrm{B_{max}}$	max joint viscosity	4[2]	Nms/rad

[1] for max co-activation
[2] for low velocity

of the pulley. $J_{arm,model}$ is the moment of inertia of the lever and r is the radius of the pulley. The axis of rotation for the lever passes through the center of the pulley which corresponds to one end of the stick. The moment of inertia of the forearm about the axis is calculated by applying the *Parallel Axis Theorem*:

$$J_{arm,model} = J_{CM} + M\,d^2$$

where J_{CM} is the moment of inertia of the forearm if the rotation axis were to pass through its center of mass, and d is the displacement of the axis from the center of mass, which is $\frac{1}{2}\,l$. Therefore, this means that:

$$\begin{aligned} J_{arm,model} &= \frac{1}{12}\,M\,l^2 + M\,d^2 = \frac{1}{12}\,(1.5\,kg)(0.35\,m)^2 + \\ &\quad (1.5\,kg)(\frac{1}{2}\,0.35\,m)^2 = 0.06125\,kg\ m^2 \quad . \end{aligned}$$

The rotational inertia of the forearm about the axis is $0.06125\,kg\ m^2$.

The dynamics model equations of the setup shown in fig. 2.5(b) are:

$$\left\{ \begin{array}{lcl} \dot{\alpha} & = & \omega \\ J_{arm,model}\,\frac{\partial \omega}{\partial t} & = & \tau_{net} - \tau_G - \tau_L \quad , \end{array} \right. \tag{2.11}$$

where τ_{net} is the joint net-torque, which is the sum of the torques of all the muscles crossing the joint. The antagonistic muscles produce torques in opposite directions, resulting in the net-torque being the difference between the torques produced by each muscle:

$$\tau_{net} = \tau_2 - \tau_1 \quad . \tag{2.12}$$

τ_L is the load torque

$$\tau_L = F_L\,l$$

and τ_G is the gravitational torque about the joint

$$\tau_G = M\,g\,d\,\sin(\alpha) \quad ,$$

where g is the acceleration due to gravity. The muscle parameters adopted in this thesis are based on measurements of the elbow muscles performed by Murray et al. (2000). The values for maximum isometric force, maximum shortening velocity and the curvature constant in the force-velocity curve are selected based on the values of elbow joint stiffness and viscosity, experimentally measured by Lacquaniti et al. (1982) and Bennett et al. (1992) (and reported in Table 2.2). The parameters for *muscle* 1 (M_1, extensor muscle) and *muscle* 2 (M_2, flexor muscle) are given in Table 2.3.

The forces generated by the antagonistic muscles integrated into the model can be depicted over the joint range of motion (joint angle α). Due to the joint setup, the muscles are coupled by the skeletal framework and therefore their force-length curves are superimposed. Figure 2.6 depicts the force-angle relationship of *muscle* 1 and *muscle*

Table 2.3: Muscle parameters hinge joint.

Variable	Description	M_1	M_2	Unit
L_{off}	pre-stretch	0.0	-0.035	m
w_{L0}	half width F-L curve·optimal length	0.08	0.06	m
F_{max}	maximum isometric force	800	1200	N
K_p	passive curve constant	2	2	
V_{max}	max short. velocity	150	150	m/s
N_n	max F/F_{max} at $-V_{max}$	1.8	1.8	
K_v	curvature constant F-V curve	5	5	

2 for the pulley joint system, for the static case ($\omega = 0$, i.e. the force contribution of the force-velocity curve for both muscles is 1) and for maximum activations ($a_1 = a_2 = 1$) when the quadratic force-length muscle function is adopted. The red curve depicts the normalized force generated by *muscle* 1 and the blue curve shows the normalized force (mirrored due to antagonistic setup) for *muscle* 2.

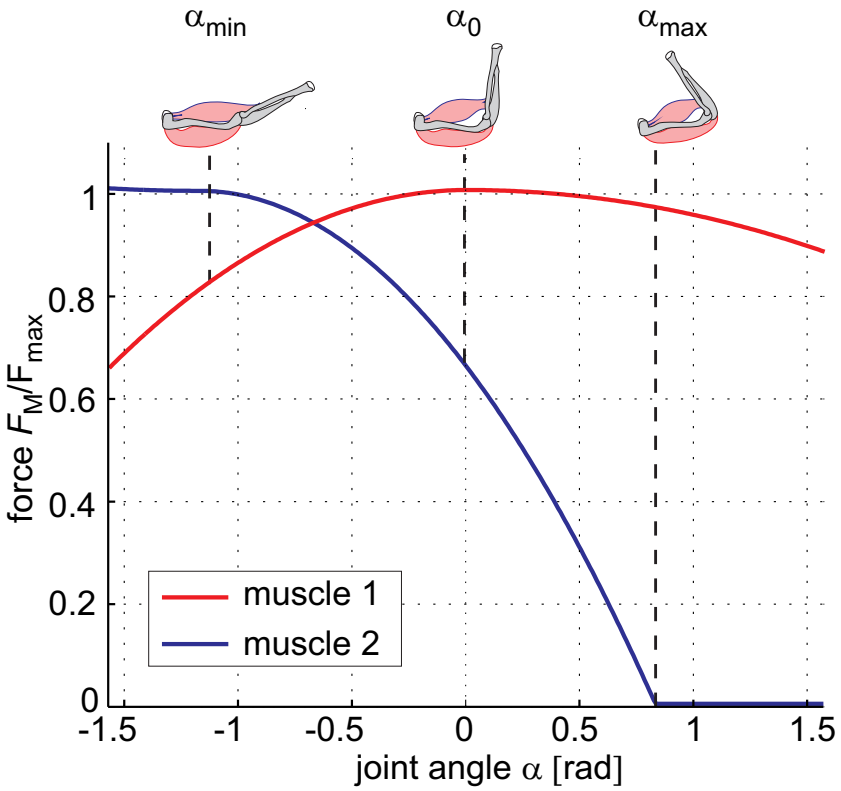

Fig. 2.6: Forces in a hinge joint generated by two antagonistic muscles plotted over joint angle for maximal activation and in the static case when the quadratic force-length muscle function is adopted. The dashed lines indicate force contributions corresponding to three different joint positions.

2.2 Mechanical impedance in a pulley hinge joint geometry

An important function of the activity of antagonistic muscle groups is the modulation of the mechanical impedance (Hogan, 1984). The mechanical impedance of biological systems is often described using spring-damper-inertia (KBI) models (Popescu et al., 2003). A KBI-model consists of a stiffness element (K), a damping element (B), and an inertia element (I), where stiffness and damping parameters are typically identified experimentally (through an optimization to obtain a best fit with experimental data). Recent results suggest that the use of such models to investigate the dynamical properties of the musculoskeletal system under the control of the CNS is problematic because a KBI-model neglects important properties of real musculoskeletal systems (Kistemaker and Rozendaal, 2011). In this thesis the mechanical impedance about a joint is analyzed by studying separately stiffness and viscosity properties. We illustrate those properties in a mathematical framework adopting the Hill-type muscle model and the pulley joint geometry introduced in Section 2.1.

2.2.1 Reciprocal activation and co-activation of muscles

Biological systems are elastic and are able to modulate the compliance at the joint according to the task. The CNS is responsible for the muscle activation. Over the last thirty years experimental observations of biological systems have shown that during movements a superposition of two central commands to antagonistic motorneurons takes place: *reciprocal activation* (i.e. a net activation difference) and *co-activation* (i.e. the activation is the same for all muscles) of antagonistic muscle groups (Feldman, 1980; Franklin et al., 2008; Humphrey and Reed, 1983; Yamazaki et al., 1994). Reciprocal activation controls the net joint torque while, due to the intrinsic muscle nonlinear elasticity, joint compliance modulation is achieved through antagonistic muscle co-activation (Hogan, 1984). Research in biomechanics has suggested that co-activation and movement of a limb can be controlled separately. For example subjects are able to keep the net joint torque at a zero level, while the stiffness can be varied over a wide range (Kearney and Hunter, 1990; Milner and Cloutier, 1998; Serres and Milner, 1991). Other studies, however, suggest that joint stiffness and movements are closely connected (Gribble et al., 1998; Suzuki et al., 2001) because the CNS adequately co-activates the muscles and thus stiffens the joint during movements or when a disturbance is acting on the limb to achieve robust stability (Gribble et al., 2003; Suzuki et al., 2001). The price of co-activation is an increased level of energy consumption as opposing muscles do not generate mechanical work (Carter et al., 1993; Hogan, 1984).

In this thesis, a novel bio-inspired control strategy is designed which adopts this biological control pattern based on the superposition of *reciprocal activation* and *co-activation*. With the objective of realizing a simultaneous control of position and stiffness for the

simplified model of the human elbow joint with a pulley, joint stiffness has to be characterized and analyzed.

2.2.2 Joint stiffness computation

The notion of stiffness as it is used in this thesis is related to the derivative of the force-length relation (the slope) of the muscle model with respect to the muscle displacement. This definition of stiffness (or its inverse, elasticity) complies with the notion of active compliance or active stiffness in robotics which defines an actively controlled displacement of a robot limb based on a force sensor signal without storing and releasing elastic energy [see e.g. (Siciliano and Khatib, 2008)]. In cases where the physical nature of a restoring force is neglected, it has been suggested that the term apparent stiffness should be used instead (Latash and Zatsiorsky, 1993). In this work, tendons as serial stiffness elements in the muscle model are omitted because in most cases the contractile element in the muscle appears more elastic and therefore dominates the overall stiffness [for tendon strain see Crisp (1972); for muscle strain see Burkholder and Lieber (2001)]. Also, Short Range Stiffness (SRS), which represents the ability of a muscle to compensate perturbations before active voluntary or reflex action sets in (Cui et al., 2008) is omitted in this study. SRS seems to acquire more importance in dynamic movements. However, its overall significance has not yet been broadly evaluated (Hu et al., 2011). For the analysis of the stiffness, the Gaussian expression causes numerical complications due to its exponential formulation. Therefore, in this thesis we will adopt the quadratic approximation (2.9). The expression of the stiffness generated by the antagonistically actuated system described above can be obtained by calculating the first derivative of the net joint torque τ_{net} with respect to the joint angle α where

$$\tau_{\text{net}} = [F_{\text{M},2}(\Delta L_{\text{eff},2}, V_2, a_2(t)) - F_{\text{M},1}(\Delta L_{\text{eff},1}, V_1, a_1(t))]\,\text{r} \quad . \tag{2.13}$$

Therefore the stiffness, K, about the joint is

$$K = -\frac{\partial \tau_{\text{net}}}{\partial \alpha} = -\frac{\partial\,(F_{\text{M},2}\,\text{r} - \text{F}_{\text{M},1}\,\text{r})}{\partial \alpha} = \\ -\frac{\partial[(F_{\text{Laq}}(\Delta L_{\text{eff},2})\,F_{\text{V}}(V_2)\,a_2 + F_{\text{Lp}}(\Delta L_{\text{eff},2}))\,\text{F}_{\text{max},2}\,\text{r}]}{\partial \alpha} \\ +\frac{\partial[(F_{\text{Laq}}(\Delta L_{\text{eff},1})\,F_{\text{V}}(V_1)\,a_1 + F_{\text{Lp}}(\Delta L_{\text{eff},1}))\,F_{\text{max},1}\,\text{r}]}{\partial \alpha}$$

and inserting (2.6), (2.9), (2.10), (2.5) and (2.7) this yields

$$
\begin{aligned}
K(\alpha,\omega,a_1,a_2) \;=\; & 2\,\mathrm{r}^2\cdot \\
\Bigg(& \begin{cases} -\frac{\mathrm{F_{max,1}}\,a_1\,(\mathrm{L_{off,1}}+\mathrm{r}\,\alpha)}{\mathrm{w_{L01}^2}} & \text{if } \mathrm{w_{L01}} > |\mathrm{L_{off,1}}+\mathrm{r}\,\alpha| \\ 0 & \text{otherwise} \end{cases} \\
& \cdot \begin{cases} \frac{\mathrm{r}\,\omega+\mathrm{V_{max}}}{-\mathrm{K_v}\,\mathrm{r}\,\omega+\mathrm{V_{max}}} & \text{if } \omega \le 0 \\ \mathrm{N_n}+\frac{(\mathrm{N_n}-1)\,(\mathrm{V_{max}}-\mathrm{r}\,\omega)}{-7.56\,\mathrm{K_v}\,\mathrm{r}\,\omega-\mathrm{V_{max}}} & \text{otherwise} \end{cases} \\
& + \begin{cases} \mathrm{F_{max,1}}\,\mathrm{K_{p,1}}\,(\mathrm{L_{off,1}}+\mathrm{r}\,\alpha) & \text{if } \alpha > -\frac{\mathrm{L_{off,1}}}{\mathrm{r}} \\ 0 & \text{otherwise} \end{cases} \\
& - \begin{cases} \frac{\mathrm{F_{max,2}}\,a_2\,(\mathrm{L_{off,2}}-\mathrm{r}\,\alpha)}{\mathrm{w_{L02}^2}} & \text{if } \mathrm{w_{L02}} > |\mathrm{L_{off,2}}-\mathrm{r}\,\alpha| \\ 0 & \text{otherwise} \end{cases} \\
& \cdot \begin{cases} \frac{-\mathrm{r}\,\omega+\mathrm{V_{max}}}{\mathrm{K_v}\,\mathrm{r}\,\omega+\mathrm{V_{max}}} & \text{if } \omega \ge 0 \\ \mathrm{N_n}+\frac{(\mathrm{N_n}-1)\,(\mathrm{V_{max}}+\mathrm{r}\,\omega)}{7.56\,\mathrm{K_v}\,\mathrm{r}\,\omega-\mathrm{V_{max}}} & \text{otherwise} \end{cases} \\
& + \begin{cases} \mathrm{F_{max,2}}\,\mathrm{K_{p,2}}\,(\mathrm{L_{off,2}}-\mathrm{r}\,\alpha) & \text{if } \alpha < \frac{\mathrm{L_{off,2}}}{\mathrm{r}} \\ 0 & \text{otherwise} \end{cases} \Bigg) \,.
\end{aligned}
\tag{2.14}
$$

It can be seen that once the geometrical and muscle parameters are fixed the stiffness is a function of the joint angle, its derivative and the two activations. The joint stiffness can be plotted against the joint angle, α, for the cases of co-activation and zero joint velocity ($\omega = 0$) (see fig. 2.7). As the joint velocity is assumed to be zero, only force-length curves are responsible for stiffness changes. The force-length curve is a quadratic approximation and as such causes a discontinuity at $\alpha \approx 0.8\,\mathrm{rad}$ corresponding to the shortest muscle length in $\mathrm{M_2}$ for which active force is generated [see fig. 2.6].

For two muscles, acting in opposition around a joint, there exist an equilibrium position at which the net-torque [equation (2.13)] is zero. This net-torque is function, among others, of the two muscle activations. For each combination of muscle activations, a certain equilibrium position is reached. Figure 2.8 shows the net-torque against the joint angle for the setup introduced in fig. 2.6 and for perfect co-activation. The joint stiffness plotted against the joint angle of fig. 2.7 is valid in general and not only at the equilibrium position (e.g. the lower arm can be forced to a certain joint position by an external force). At that joint position, a stiffness value, as reported in the figure, can be measured.

2.2.3 Joint viscosity computation

During movement, the joint is subject to the force-velocity dependency of muscles, which leads to the concepts of dynamic stiffness and viscosity. Milner and Cloutier (1998)

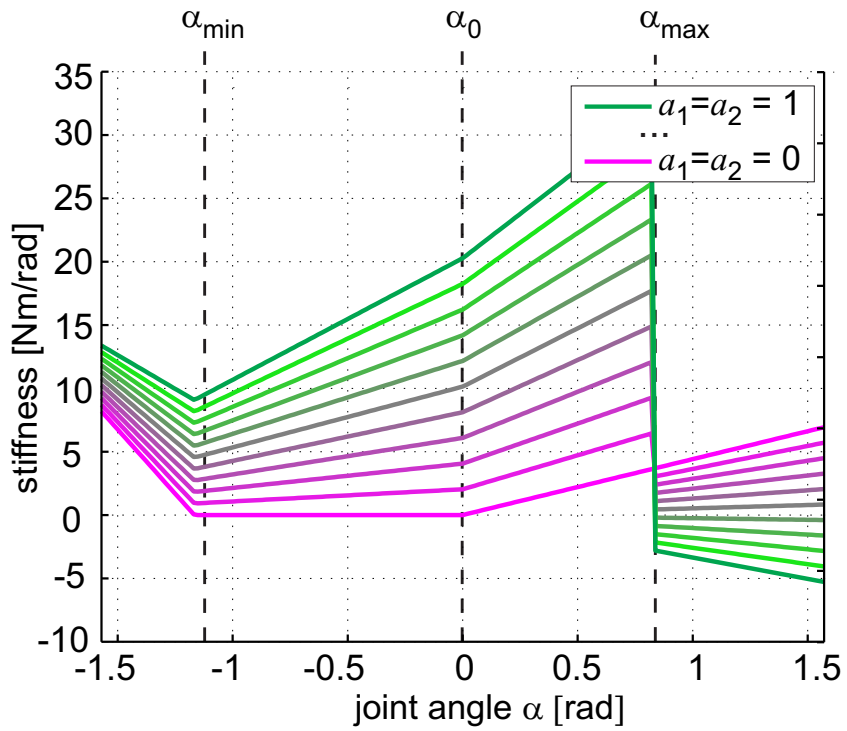

Fig. 2.7: Joint stiffness plotted against joint angle for the setup introduced in fig. 2.6 for perfect co-activation ($a_1 = a_2$).

investigated damping in a musculoskeletal system and found that the velocity-dependent properties at the joint may play an important role in reducing the destabilizing effect due to reflex delays. Furthermore, muscle viscosity depends on the steepness of the force-velocity relationship (Stroeve, 1999) and increases with increasing muscle activation. Therefore, in this thesis, the derivation of the dynamic joint stiffness during movement (or viscosity) is obtained by calculating the first derivative of the net joint torque, τ_{net}, with respect to the joint velocity, ω, (Katayama and Kawato, 1993). As a consequence, joint viscosity depends on the joint angle, its velocity and the muscle activations. The expression of the viscosity, B, for the antagonistic hinge joint in this work is

$$B = -\frac{\partial \tau}{\partial \omega} = -\frac{\partial \left(F_{\mathrm{M},2}\,\mathrm{r} - \mathrm{F}_{\mathrm{M},1}\,\mathrm{r}\right)}{\partial \omega} = \\ -\frac{\partial[(F_{\mathrm{La}}(\Delta L_{\mathrm{eff},2})\,F_{\mathrm{V}}(V_2)\,a_2 + F_{\mathrm{Lp}}(\Delta L_{\mathrm{eff},2}))\,\mathrm{F}_{\mathrm{max},2}\,\mathrm{r}]}{\partial \omega} \\ +\frac{\partial[(F_{\mathrm{La}}(\Delta L_{\mathrm{eff},1})\,F_{\mathrm{V}}(V_1)\,a_1 + F_{\mathrm{Lp}}(\Delta L_{\mathrm{eff},1}))\,\mathrm{F}_{\mathrm{max},1}\,\mathrm{r}]}{\partial \omega}\ ,$$

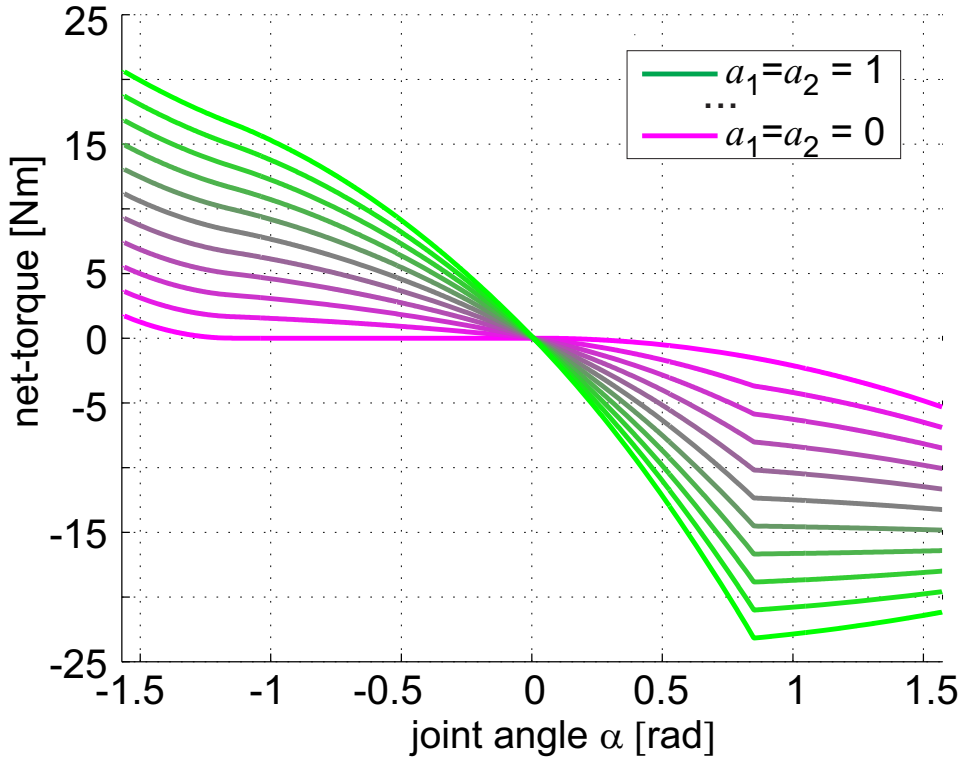

Fig. 2.8: Net-torque plotted against joint angle for the setup introduced in fig. 2.6 for perfect co-activation ($a_1 = a_2$).

and by incorporating (2.6), (2.9), (2.10), (2.5) and (2.7) this yields

$$
\begin{aligned}
&B(\alpha,\omega,a_1,a_2) \;=\\
&a_1\,\mathrm{F_{max,1}}\,\mathrm{r}\cdot\\
&\left(\begin{cases} 1-\frac{(\mathrm{L_{off,1}}+\mathrm{r}\,\alpha)^2}{\mathrm{w_{L01}^2}} & \text{if } \mathrm{w_{L01}} > |\mathrm{L_{off,1}}+\mathrm{r}\,\alpha| \\ 0 & \text{otherwise} \end{cases}\right.\\
&\cdot\left.\begin{cases} \frac{\mathrm{K_v}\,(\mathrm{r}\,\omega+\mathrm{V_{max}})}{(-\mathrm{K_v}\,\mathrm{r}\,\omega+\mathrm{V_{max}})^2}+\frac{1}{-\mathrm{K_v}\,\mathrm{r}\,\omega+\mathrm{V_{max}}} & \text{if } \omega<0 \\ \frac{1-\mathrm{N_n}-7.56\,\mathrm{K_v}\,\mathrm{N_n}}{-7.56\,\mathrm{K_v}\,\mathrm{r}\,\omega-\mathrm{V_{max}}}+\frac{7.56\,\mathrm{K_v}\,(\mathrm{r}\,\omega-\mathrm{N_n}\,\mathrm{r}\,\omega-7.56\,\mathrm{K_v}\,\mathrm{N_n}\,\mathrm{r}\,\omega-\mathrm{V_{max}})}{(-7.56\,\mathrm{K_v}\,\mathrm{r}\,\omega-\mathrm{V_{max}})^2} & \text{otherwise} \end{cases}\right)\\
&-a_2\,\mathrm{F_{max,2}}\,\mathrm{r}\cdot\\
&\left(\begin{cases} 1-\frac{(\mathrm{L_{off,2}}-\mathrm{r}\,\alpha)^2}{\mathrm{w_{L02}^2}} & \text{if } \mathrm{w_{L02}} > |\mathrm{L_{off,2}}-\mathrm{r}\,\alpha| \\ 0 & \text{otherwise} \end{cases}\right.\\
&\cdot\left.\begin{cases} \frac{-1+\mathrm{N_n}+7.56\,\mathrm{K_v}\,\mathrm{N_n}}{7.56\,\mathrm{K_v}\,\mathrm{r}\,\omega-\mathrm{V_{max}}}-\frac{7.56\,\mathrm{K_v}\,(-\mathrm{r}\,\omega+\mathrm{N_n}\,\mathrm{r}\,\omega+7.56\,\mathrm{K_v}\,\mathrm{N_n}\,\mathrm{r}\,\omega-\mathrm{V_{max}})}{(7.56\,\mathrm{K_v}\;\mathrm{r}\,\omega-\mathrm{V_{max}})^2} & \text{if } \omega<0 \\ -\frac{\mathrm{K_v}\,(-\mathrm{r}\,\omega+\mathrm{V_{max}})}{(\mathrm{K_v}\,\mathrm{r}\,\omega+\mathrm{V_{max}})^2}-\frac{1}{\mathrm{K_v}\,\mathrm{r}\,\omega+\mathrm{V_{max}}} & \text{otherwise} \end{cases}\right).
\end{aligned}
\tag{2.15}
$$

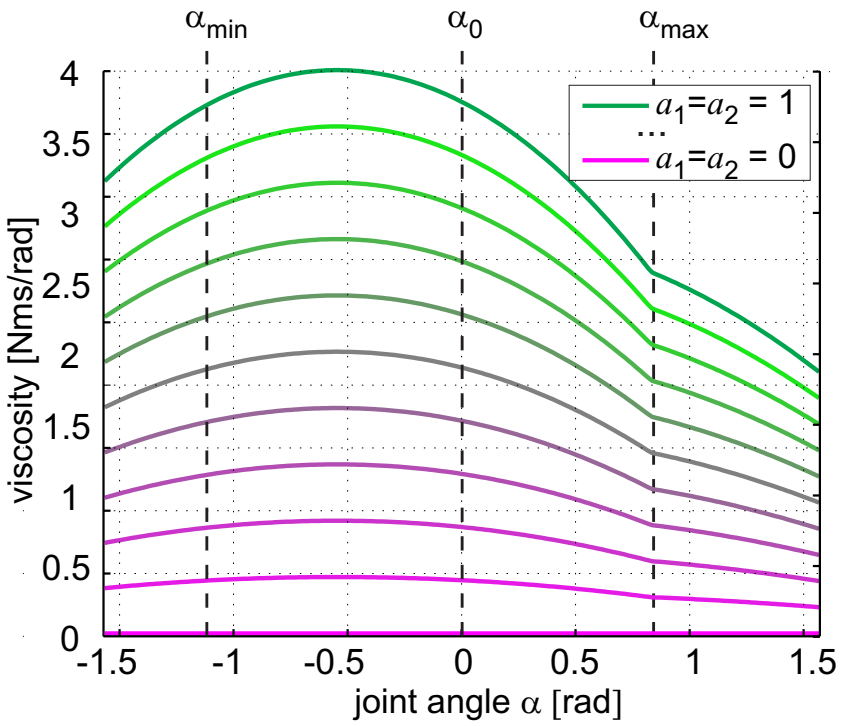

Fig. 2.9: Joint viscosity plotted against joint angle for the setup introduced in fig. 2.6 for perfect co-activation ($a_1 = a_2$) and slow movements.

Figure 2.9 shows the joint viscosity plotted against the joint angle, α, for slow movements given equal levels of activation in both muscles (co-activation).

2.3 Stiffness nodes in the joint range of motion

Generally, co-contraction of antagonistic muscles allows the joint stiffness to be varied independently of the torque (Hogan, 1984). However, in this section it will be shown that situations can occur for which the ability to control joint stiffness through co-contraction is limited.

While bio-inspiration is drawn from the antagonistic muscle setup and from the nonlinear muscle characteristics, it has to be emphasized that in this section no experimental data from a specific biological reference system has been used for the models. Parameters are either chosen exemplarily to underline particular system behaviors or they are normalized (arbitrary units, cmp. Table 2.4 and Table 2.7) and could be adapted to specific biological data later. Nevertheless, the problem statements and the drawn conclusions in this study remain valid when adjusted to realistic parameters. In Section 6.3 an example will be shown that adopts a locust geometry and real biological data in which the effects discussed here actually occur.

2.3.1 Regions in the joint range of motion resulting from overlap of the force-length curves

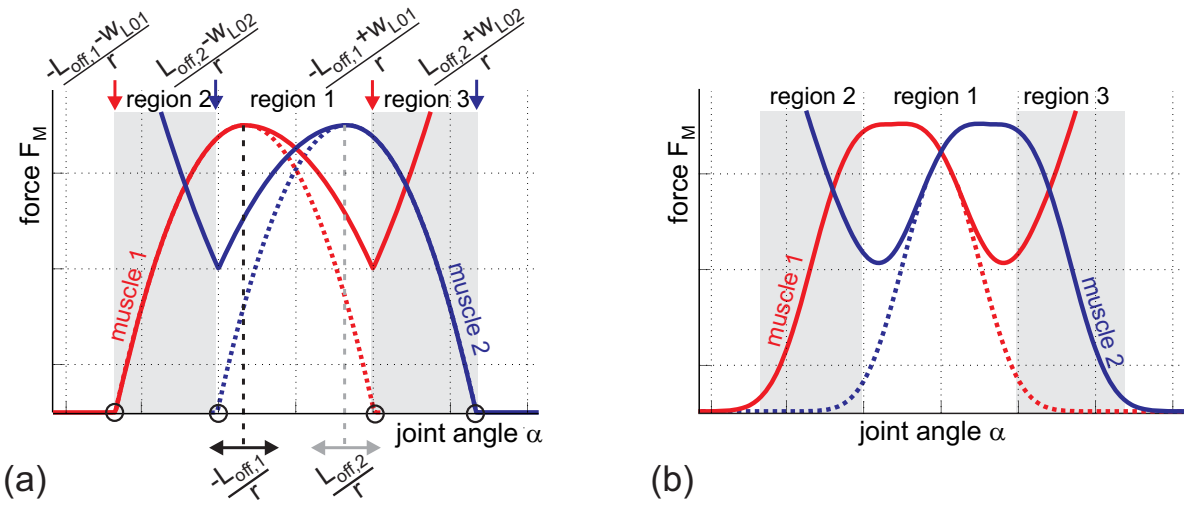

Fig. 2.10: (a) Force curves generated by two antagonistic muscles in a pulley joint plotted over the joint angle for maximum activation of both muscles. The curve for muscle 1 is depicted in red and for muscle 2 in blue (mirrored due to antagonistic setup). Dotted lines indicate the course of the active force curves. The overlaps of the active curves define three regions. The mathematical expressions for region borders are given at the top. The dashed vertical lines indicate the maximum of the force-length curves (the mathematical expressions are given at the bottom). (b) same as (a) but with the Gaussian force-length relation for the active muscle forces. Region borders are adopted from the quadratic case.

In this section, the pulley joint setup is used together with the Hill-type muscle implementation and the biological control pattern strategy, to evaluate how muscle parameters influence the stiffness properties.
The forces generated by two antagonistic muscles used in a pulley joint setup can be depicted with respect to the angle of joint rotation α (see fig. 2.10). Figure 2.10(a) depicts the force-angle relationship using the *quadratic* force-length expression and for ω=0 (i.e. the force-velocity function contribution for both muscles is 1). The red curve depicts the overall muscle force of *muscle 1* and the blue curve shows the same for *muscle 2*. The dotted lines indicate the course of the active muscle forces. The origins of the two active force-angle functions are highlighted with circles. For zero forces, the active muscle force curves indicate the natural borders of three regions. These three regions occur when the muscle workspaces of the two antagonistic muscles overlap (which is normally the case). Each region is bounded by two joint angles defined by the origins of the active force-angle curves of a muscle. For two muscles, a maximum number of three

regions may occur[2]. The middle region (region 1) represents the main working range of the joint since both antagonistic muscles can actively influence the joint behavior. It has to be emphasized that these regions are not a special case due to the piecewise definition of the quadratic force length dependency but rather natural regions[3]. Hence, also in the Gaussian case, which is depicted in fig. 2.10(b), three regions are depicted over the joint angular range[4]. We therefore use the same region descriptions that were derived from the quadratic case in both contexts. In order to evaluate stiffness properties in the static case, the stiffness equation (2.14) is considered. For the special case $\omega = 0$, it reduces to:

$$
\begin{aligned}
K(\alpha, a_1, a_2) \;=\; & 2\,\mathrm{r}^2 \cdot \\
\Bigg(& \begin{cases} -\frac{\mathrm{F_{max,1}}\; a_1\; (\mathrm{L_{off,1}} + \mathrm{r}\,\alpha)}{\mathrm{w_{L01}^2}} & \text{if } \mathrm{w_{L01}} > |\mathrm{L_{off,1}} + \mathrm{r}\,\alpha| \\ 0 & \text{otherwise} \end{cases} \\
- & \begin{cases} \frac{\mathrm{F_{max,2}}\; a_2\; (\mathrm{L_{off,2}} - \mathrm{r}\,\alpha)}{\mathrm{w_{L02}^2}} & \text{if } \mathrm{w_{L02}} > |\mathrm{L_{off,2}} - \mathrm{r}\,\alpha| \\ 0 & \text{otherwise} \end{cases} \\
+ & \begin{cases} \mathrm{F_{max,1}}\, \mathrm{K_{p,1}}\, (\mathrm{L_{off,1}} + \mathrm{r}\,\alpha) & \text{if } \alpha > -\frac{\mathrm{L_{off,1}}}{\mathrm{r}} \\ 0 & \text{otherwise} \end{cases} \\
+ & \begin{cases} \mathrm{F_{max,2}}\, \mathrm{K_{p,2}}\, (\mathrm{L_{off,2}} - \mathrm{r}\,\alpha) & \text{if } \alpha < \frac{\mathrm{L_{off,2}}}{\mathrm{r}} \\ 0 & \text{otherwise} \end{cases} \Bigg) \; .
\end{aligned}
\tag{2.16}
$$

The first two lines of equation (2.16) represent the stiffness contribution due to the active force-length relationship. The superposition of these active regions defines region 1. On either side of this superimposed region, two regions may exist in which only one muscle is able to produce an active force (region 2 and region 3). Figure 2.11(a) shows the joint stiffness for a quadratic force-length relation plotted against the joint angle α in the case of co-activation. As expected, the stiffness in region 1 can be varied from a minimum to a maximum value while increasing co-activation levels.
Using a numerical simulation, the stiffness-angle plot for the Gaussian force-length expression can be generated [see fig. 2.11(b)]. The principal ability to change the stiffness by means of co-activation is the same as in fig. 2.11(a). The muscle parameters adopted for the plots in fig. 2.10 are listed in Table 2.4 (column: *No node occurrence*). The radius r of the pulley is assumed to be 1.

[2]Three regions occur when the two active curves partially overlap. Two regions occur when the curves do not overlap. Only one region occurs when the two curves are completely overlapped.

[3]Active muscle force-length curves are actually limited.

[4]Although the Gaussian formulation presents unlimited borders, which would lead to ∞ wide regions, in this thesis, the regions formulation as obtained for the quadratic force-length curves, is adopted.

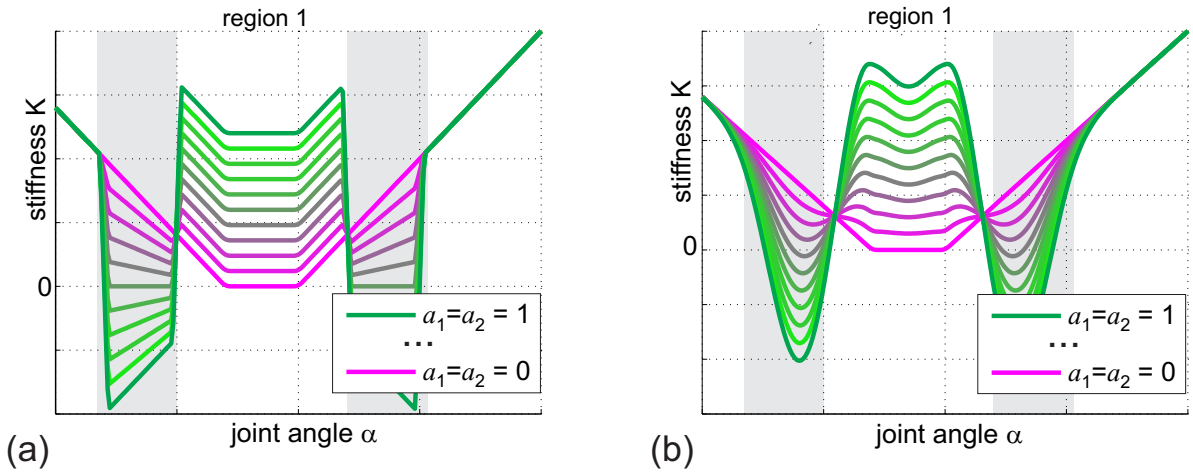

Fig. 2.11: (a) Joint stiffness plotted against the joint angle for the setup in fig. 2.10 for perfect co-activation. The highest activation ($a_1 = a_2 = 1$) is depicted in green. (b) same as (a) but with the Gaussian force-length relation for the active muscle forces.

Table 2.4: Muscle parameters of the antagonistic pulley joint setup.

		No node occurrence		Node occurrence	
Parameter	Description	M_1	M_2	M_1	M_2
L_{off}	pre-stretch	0.0	−0.3	0.0	−0.025
w_{L0}	half width F-L curve	0.5	0.5	0.5	0.5
F_{max}	max. isometric force	1	1	1	1
K_p	passive curve const.	2	2	2	2

2.3.2 Stiffness nodes evaluation for a pulley hinge joint geometry

In a concurrent torque-stiffness control system, along with joint stiffness, joint torque can be varied and therefore the activation levels to the antagonistic muscles cannot remain the same. A certain offset and proportionality between the two activations should be expected. In this context, dependent on the geometrical joint parameters, one can find angular joint positions for which the joint stiffness does not change when varying the activation levels of the muscles. Such points will be called "stiffness nodes". Figure 2.12(a) shows the occurrence of a stiffness node in the region 1 for an activation ratio of $a_1/a_2 = 1.5$ and for a muscle pre-stretch, $L_{off,2}$, slightly changed[5] with respect to the situation in fig. 2.11 (to view the muscle parameters see Table 2.4, column: *Node occurrence*). At this joint angle, the system loses its ability to choose a certain stiffness as long as the activation ratio remains the same. Figure 2.12(b) shows a similar

[5]The pre-stretch $L_{off,2}$ was changed such that the stiffness node occurred in the middle.

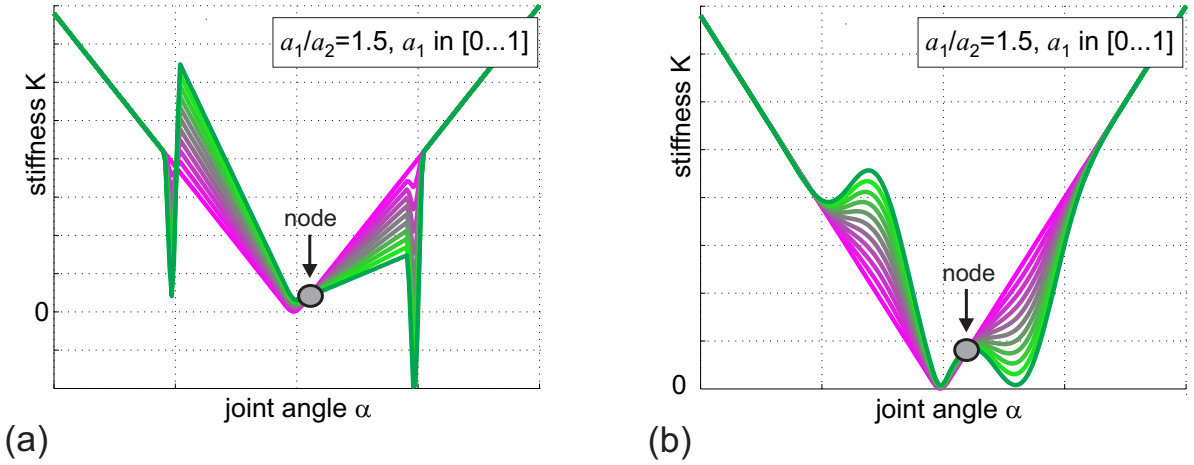

Fig. 2.12: (a) Joint stiffness plotted over the joint angle using the activation scheme a_1/a_2=1.5) and, in order to have a better visualization of the node position, the muscle pre-stretch $L_{off,2}$ is slightly changed with respect to the situation in fig. 2.11. The highest activation ($a_1 = 1$) is depicted in green. For a certain joint angle, a stiffness node occurs. (b) same as (a) but with the Gaussian force-length relation for the active muscle forces.

behavior when using a Gaussian force-length expression. Besides a small deviation of the stiffness node position due to the different force-length function approximation, the main characteristics are maintained (a comparison of the stiffness node positions in the Gaussian and quadratic case is provided in Section 2.3.4).

In order to derive an analytical expression for the positions of stiffness nodes, the stiffness expression has to be inspected more closely in terms of activations. For combinations of α, a_1 and a_2 for which a change of a_1 and a_2 results in a minimal stiffness change (stiffness node), the total differential of the function K with respect to a_1 and a_2 is zero.

$$\mathrm{d}K(\alpha, a_1, a_2) = \frac{\partial[K(\alpha, a_1, a_2)]}{\partial a_1}\mathrm{d}a_1 + \frac{\partial[K(\alpha, a_1, a_2)]}{\partial a_2}\mathrm{d}a_2 \stackrel{def}{=} 0 \ , \tag{2.17}$$

where $\mathrm{d}a_1$ and $\mathrm{d}a_2$ are the differential changes in a_1 and a_2.
For the combination of the pulley geometry (2.6) and the quadratic force length expression (2.9), this results in

$$\mathrm{d}a_1\ \mathrm{r}\cdot\left(\begin{cases} -2\,\mathrm{r}\,\frac{\mathrm{F_{max,1}}\,(\mathrm{L_{off,1}}+\mathrm{r}\,\alpha)}{\mathrm{w}_{\mathrm{L01}}^2} & \text{if} \quad \mathrm{w_{L01}} > |\mathrm{L_{off,1}}+\mathrm{r}\,\alpha| \\ 0 & \text{otherwise} \end{cases}\right) -$$
$$\mathrm{d}a_2\ \mathrm{r}\cdot\left(\begin{cases} 2\,\mathrm{r}\,\frac{\mathrm{F_{max,2}}\,(\mathrm{L_{off,2}}-\mathrm{r}\,\alpha)}{\mathrm{w}_{\mathrm{L02}}^2} & \text{if} \quad \mathrm{w_{L02}} > |\mathrm{L_{off,2}}-\mathrm{r}\,\alpha| \\ 0 & \text{otherwise} \end{cases}\right) \stackrel{def}{=} 0 \ ,$$

that, in piecewise notation, corresponds to

$$\begin{cases} -\frac{2\,F_{max,1}\,da_1\,r^2\,(L_{off,1}+r\,\alpha)}{{w_{L01}}^2}+ \\ -\frac{2\,F_{max,2}\,da_2\,r^2\,(L_{off,2}-r\,\alpha)}{{w_{L02}}^2} = 0 \text{ if } \quad w_{L01} > |L_{off,1}+r\,\alpha| \ \wedge \quad w_{L02} > |L_{off,2}-r\,\alpha| \\ -\frac{2\,F_{max,1}\,da_1\,r^2\,(L_{off,1}+r\,\alpha)}{{w_{L01}}^2} = 0 \text{ if } \quad w_{L01} > |L_{off,1}+r\,\alpha| \ \wedge \quad w_{L02} \leq |L_{off,2}-r\,\alpha| \\ -\frac{2\,F_{max,2}\,da_2\,r^2\,(L_{off,2}-r\,\alpha)}{{w_{L02}}^2} = 0 \text{ if } \quad w_{L01} \leq |L_{off,1}+r\,\alpha| \ \wedge \quad w_{L02} > |L_{off,2}-r\,\alpha| \,. \end{cases}$$

By solving these equations for α and assuming $da_1 \neq 0$ and $da_2 \neq 0$, the positions of the stiffness nodes are defined:

$$\alpha = \frac{L_{off,2}+L_{off,1}\,\frac{da_1\,F_{max,1}\,{w_{L02}}^2}{da_2\,F_{max,2}\,{w_{L01}}^2}}{r\,(1-\frac{da_1\,F_{max,1}\,{w_{L02}}^2}{da_2\,F_{max,2}\,{w_{L01}}^2})} \quad \text{if } w_{L01} > |L_{off,1}+r\,\alpha| \wedge w_{L02} > |L_{off,2}-r\,\alpha| \tag{2.18}$$

$$\alpha = -\frac{L_{off,1}}{r} \quad \text{if } w_{L01} > |L_{off,1}+r\,\alpha| \wedge w_{L02} \leq |L_{off,2}-r\,\alpha| \tag{2.19}$$

$$\alpha = \frac{L_{off,2}}{r} \quad \text{if } w_{L01} \leq |L_{off,1}+r\,\alpha| \wedge w_{L02} > |L_{off,2}-r\,\alpha| \,. \tag{2.20}$$

Equation (2.18) is only dependent on the ratio of da_1 and da_2 and since in this study the assumption $\frac{a_1}{a_2} = const.$ is made (i.e. the activations are in a linear relation), the ratio $\frac{da_1}{da_2}$ can be replaced by $\frac{a_1}{a_2}$:

$$\alpha = \frac{L_{off,2}+L_{off,1}\,\frac{a_1\,F_{max,1}\,{w_{L02}}^2}{a_2\,F_{max,2}\,{w_{L01}}^2}}{r\,(1-\frac{a_1\,F_{max,1}\,{w_{L02}}^2}{a_2\,F_{max,2}\,{w_{L01}}^2})} \quad \text{if } w_{L01} > |L_{off,1}+r\,\alpha| \wedge w_{L02} > |L_{off,2}-r\,\alpha| \,. \tag{2.21}$$

Inserting the solutions for α into the respective region results in the conditions for the existence of a node in each region. For the region 1, a node therefore exists if

$$\left[\frac{a_1\,F_{max,1}}{a_2\,F_{max,2}} < \frac{{w_{L01}}^2}{{w_{L02}}^2} \wedge \left(|L_{off,1}+L_{off,2}| < \left|\frac{\frac{a_2\,F_{max,2}}{a_1\,F_{max,1}}\,{w_{L01}}^2-{w_{L02}}^2}{w_{L02}}\right|\right)\right] \wedge$$
$$\left[\frac{a_1\,F_{max,1}}{a_2\,F_{max,2}} > \frac{{w_{L01}}^2}{{w_{L02}}^2} \wedge \left(|L_{off,1}+L_{off,2}| < \left|\frac{\frac{a_1\,F_{max,1}}{a_2\,F_{max,2}}\,{w_{L02}}^2-{w_{L01}}^2}{w_{L01}}\right|\right)\right]. \tag{2.22}$$

The nodes in the side regions (region 2 and region 3) will exist if they satisfy the following conditions, respectively:

$$w_{L01} > 0 \ \wedge \ w_{L02} \leq |L_{off,1}+L_{off,2}| \tag{2.23}$$
$$w_{L02} > 0 \ \wedge \ w_{L01} \leq |L_{off,1}+L_{off,2}| \,. \tag{2.24}$$

A closer inspection of the node position in the region 1, as expressed in equation (2.21), shows that the node is absent if one of the two factors in the denominator is zero

(given that the numerator is positive and not equal to zero). The first factor r is the radius of the pulley which cannot be smaller than zero to allow torque generation. The second factor $(1 - \frac{a_1 \, \mathrm{F_{max,1}} \, {\mathrm{w_{L02}}}^2}{a_2 \, \mathrm{F_{max,2}} \, {\mathrm{w_{L01}}}^2})$ is zero in the special case of equal muscles and activations ($\mathrm{w_{L01}} = \mathrm{w_{L02}}$, $\mathrm{F_{max,1}} = \mathrm{F_{max,2}}$, a_1=a_2). In the general case this factor has to be inspected more closely.

2.3.3 Active force-length function approximation: cubic spline interpolation

In the previous section it was shown that in a hinge joint setup with two muscles pulling upon a pulley, the superposition of the two force-length curves generate up to three regions in the joint angle space and up to three stiffness nodes could occur in the stiffness function. The active length-dependent force function, F_{La}, plays the most important role in the stiffness evaluation. It was shown that this function can be approximated with a quadratic or Gaussian expression. However, while for the quadratic approximation it was possible to get a closed expression for the regions, the node positions and the conditions of existence, the same mathematical formulation gives numerical complications when performed with the Gaussian expression. On the other hand, despite the fact that the quadratic approximation has the quality that it is easy to manipulate, it leads to problems in the differential operations as can be seen by the sharp discontinuities and abrupt transition to a zero force [see fig. 2.6 and fig. 2.11(a)]. Therefore, a function with a smoother shape than the quadratic function but simpler than the Gaussian is desired. A good candidate would be a third order polynomial. Moreover since in the stiffness analysis differential operations are required, there is the need to have at least C^2 functions[6]. Cubic splines satisfy the above requirements. Therefore, in this section, a cubic spline interpolation for the Gaussian force-length function (2.8) is performed.

For interpolation purposes, the function domain has to be selected and divided into a discrete set of known data points. Since the active region of the force-length function is assumed to range from $\sim 0.5\,\mathrm{L_0}$ to $\sim 1.5\,\mathrm{L_0}$, the domain extremes of the interpolation function are set to $0.25\,\mathrm{L_0}$ and $1.75\,\mathrm{L_0}$. Since interpolation over uniform spaced intervals does not guarantee the best approximation, an optimization scheme is introduced in order to find the subset of intervals that delivers the best fit. $\mathrm{L_0}$ is kept in the middle of the domain on purpose, thus dividing it in two halves. For symmetrical reasons, only even numbers of subintervals are evaluated.
Given $x_0 = 0.25\,\mathrm{L_0}$ and $x_m = 1.75\,\mathrm{L_0}$, (where m is the number of subintervals) the optimization algorithm has to find the vector β of parameters x_j with j=1:m-1 such that the spline interpolation model function $f(\overline{x}, \beta)$ best fits the data set (x_i, y_i) with i=1:n and $y_i = F_{\mathrm{LaG}}(x_i)$ (n is the number of points for which the error is evaluated and in our case corresponds to 1000). A residual r_i is defined as the difference between the

[6]First and second derivatives are continuous.

Table 2.5: Least Mean Square interpolation error and sub-intervals.

m	LMS error	$x_j\,\mathrm{L_0}$, (j = 1 : m − 1)
4	0.040926	0.446, 1, 1.56
6	0.0056325	0.624, 0.777, 1, 1.195, 1.404
8	0.00371426	0.607, 0.833, 1, 1.17, 1.237, 1.416, 1.584
10	0.00198698	0.396, 0.583, 0.807, 1, 1.188, 1.345, 1.4, 1.545, 1.729

actual value of the dependent variable y_i and the value predicted by the model function:

$$r_i = y_i - f(x_i, \beta) \quad . \tag{2.25}$$

The least squares method finds its optimum when the sum S of squared residuals is at a minimum:

$$\min_{x\in(0.25\,\mathrm{L_0},1.75\,\mathrm{L_0})} S \;=\; \min_{x\in(0.25\,\mathrm{L_0},1.75\,\mathrm{L_0})} \sum_{i=1}^{\mathrm{n}} {r_i}^2 \tag{2.26}$$

The results of the optimization process are shown in Table 2.5 for different numbers of subintervals m. As could be expected, the bigger m, the smaller the Least Mean Square (LMS) error. Each subinterval corresponds to a piecewise cubic polynomial interpolation of the Gaussian function. For simplification purposes, the number of polynomials that are needed to interpolate the function should be kept small. The best compromise between LMS error and number of intervals corresponds to the selection $m = 6$[7]. Given six subintervals along the *length* axis of the force-length function, the corresponding spline interpolation composed by six polynomials has the form:

$$f(x) = \begin{cases} a_0 + a_1\,x + a_2\,x^2 + a_3\,x^3, & 0.25\,\mathrm{L_0} \le \mathrm{x} \le \mathrm{x_1\,L_0} \\ b_0 + b_1\,x + b_2\,x^2 + b_3\,x^3, & x_1\,\mathrm{L_0} \le \mathrm{x} \le \mathrm{x_2\,L_0} \\ c_0 + c_1\,x + c_2\,x^2 + c_3\,x^3, & x_2\,\mathrm{L_0} \le \mathrm{x} \le \mathrm{x_3\,L_0} \\ d_0 + d_1\,x + d_2\,x^2 + d_3\,x^3, & x_3\,\mathrm{L_0} \le \mathrm{x} \le \mathrm{x_4\,L_0} \\ e_0 + e_1\,x + e_2\,x^2 + e_3\,x^3, & x_4\,\mathrm{L_0} \le \mathrm{x} \le \mathrm{x_5\,L_0} \\ f_0 + f_1\,x + f_2\,x^2 + f_3\,x^3, & x_5\,\mathrm{L_0} \le \mathrm{x} \le 1.75\,\mathrm{L_0}\ . \end{cases} \tag{2.27}$$

By using the length L instead of x and by recalling the positions made in Section 2.1.3 ($\mathrm{w\,L_0} = \mathrm{w_{L0}}$ and $L - \mathrm{L_0} = \Delta\mathrm{L_{eff}}$), the general form for each of the six polynomials (2.27) is:

$$P_i(L) = p_0 + p_1\,\frac{\Delta L_{\mathrm{eff}} + 2\,\mathrm{w_{L0}}}{2\,\mathrm{w_{L0}}} + p_2\,\frac{(\Delta L_{\mathrm{eff}} + 2\,\mathrm{w_{L0}})^2}{(2\,\mathrm{w_{L0}})^2} + p_3\,\frac{(\Delta L_{\mathrm{eff}} + 2\,\mathrm{w_{L0}})^3}{(2\,\mathrm{w_{L0}})^3},$$
$$\text{for} \quad 2\,\mathrm{w_{L0}}\,(x_{\mathrm{i}} - 1) \le \Delta\mathrm{L_{eff}} \le 2\,\mathrm{w_{L0}}\,(x_{\mathrm{i+1}} - 1) \text{ and } i{=}1{:}6\ . \tag{2.28}$$

[7]Criterion of selection: the combination that delivers the minimum LMS error weighted for the square of m is selected.

The six polynomials in (2.28) present 24 unknowns and for achieving the spline interpolation, an equal number of conditions have to be set. Beyond the requirements of interpolation (6 conditions) and continuity (6 conditions), for each internal point, first derivative continuity (5 conditions) and second derivative continuity (5 conditions) are required. In order to have a system with the same number of equations and unknowns, as last two conditions the *clamped* convention has been selected for which end slopes are prescribed. In our case this means the following conditions,

$$\begin{aligned} \frac{dP_1(x)}{dx} &= 0 \text{ at } x = x_0 \\ \frac{dP_6(x)}{dx} &= 0 \text{ at } x = x_6 \end{aligned} \quad ,$$

are imposed.

Table 2.6 reports the numerical values of the 24 unknowns $(a_0, ..., f_3)$ obtained as a result of the spline interpolation. Figure 2.13 depicts the force-length function approximation obtained adopting the spline interpolation. For comparison purposes, the Gaussian and quadratic curves are also plotted.

Similar to the quadratic approximation (Section 2.1.3), the spline interpolation case allows an expression of the stiffness as well as the stiffness node positions and the conditions of existence to be derived.

2.3.4 Stiffness nodes prediction for different force-length curve approximations

As it was pointed out in Section 2.3.2, the stiffness node positions predicted adopting the quadratic approximation of the force-length function might differ from the positions obtained when the Gaussian approximation is used. With the objective to evaluate the ability to provide a good estimation for the node positions in the angular range of motion when using quadratic and spline interpolation, in this section a comparison with the stiffness node positions obtained numerically adopting the Gaussian force-length curve

Table 2.6: Spline interpolation–polynomials parameters.

parameter	p_0	p_1	p_2	p_3
a	−0.23	2.43	−8.29	9.15
b	11.89	−55.81	85.01	−40.67
c	−12.79	39.45	−37.59	11.93
d	13.15	−38.35	40.2	−14
e	−62.57	151.72	−118.83	30.35
f	50.95	−90.76	53.82	−10.62

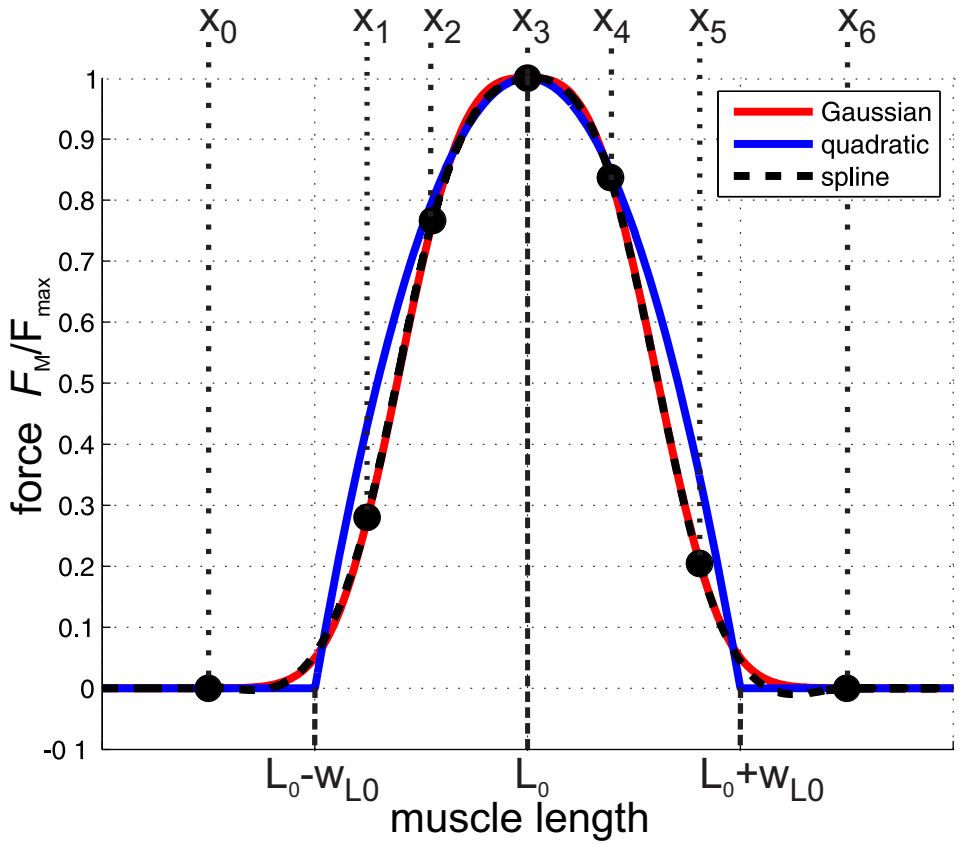

Fig. 2.13: Force-length approximation for Gaussian, quadratic and spline interpolation.

will be evaluated. The stiffness node estimation is pursued for all the possible combinations of the parameters [$w_{L0,1}$, $w_{L0,2}$, $L_{off,1}$, $L_{off,2}$] varied in a certain range and for different activation ratios $c_1 = a_1/a_2$. Table 2.7 reports the parameters and their range of variation. 4356 combinations have been evaluated and for each of them a maximum of three stiffness nodes have been obtained. A prediction error for each stiffness node, ϵ_{node}, can be calculated comparing the positions in the quadratic and spline interpolation with respect to the Gaussian case. Figure 2.14(a) depicts the prediction error for each of the three possible nodes when the quadratic curve is used (Gaussian-quadratic error $\epsilon_{Gq,node}$). Figure 2.14(b) shows the prediction error when the cubic spline interpolation is adopted (Gaussian-spline error $\epsilon_{Gs,node}$). The average prediction error adopting the spline interpolation is four times smaller than that obtained by using the quadratic approximation.
In most of the cases, out of the three conditions of node existence [equations (2.22), (2.23) and (2.24)] only two were satisfied (i.e., out of the three possible nodes, only two turned up). Therefore, for most of the parameter combinations the prediction error for node 3 ($\epsilon_{node,3}$) does not exist (missing bars in fig. 2.14).
In the Gaussian-quadratic error evaluation, the biggest prediction error for node 1 and 2 is obtained when the pre-stretches parameters $L_{off,1}$ and $L_{off,2}$ are at the range limit

and increases for increasing activation ratio c_1. This is not the case when the spline interpolation is adopted. Furthermore, parameters $w_{L0,1}$ and $w_{L0,2}$ slightly influence the prediction error for both cases.
Finally, the adoption of the cubic spline interpolation generates a prediction error which, in most of the cases, is lower than 0.1 rad. This result confirms that such an approximation might be adopted instead of the Gaussian representation delivering a negligible prediction error.

2.3.5 Integration of a compliant tendon in the muscle model

In biological systems muscles are a source of force. It is well known that muscles practically do not store a significant amount of elastic energy. Some energy is stored in the titin molecules, which are represented by the passive force-length curve in the Hill-model. Tendons, however, are able to store and return almost all of the deformation energy with little energy dissipation (Alexander, 1988). In current models of the muscle-tendon complex, the tendons are connected in series with the contractile element (muscle model). The physiological range of tendon strain lies below 4% (Crisp, 1972) whereas many muscles show elongation and shortening of more than ±50% (Burkholder and Lieber, 2001). Because of the serial connection, tendon and contractile element experience the same force which results in a domination of the contractile element over the tendon with respect to the general compliant behavior in these cases (assuming that the tendon length is approximately the same as the muscle length or shorter). For this reason and because tendon stiffness does not depend on the activation of the respective muscle, in Section 2.1.1 a simplification assumption was adopted and the tendon was considered to be very stiff. In this section we want to show that the stiffness properties obtained so far are valid even when more compliant tendons are included into the muscle model.

The tendon can be modeled as an elastic element where its compliance is proportional to the tendon slack length (L_{ts}). In the model proposed by Zajac the tendon is modeled

Table 2.7: Parameters used in the stiffness nodes prediction error evaluation process. Each parameter is defined with a starting value and a range in which it can vary during the process.

			Range of variability	
Parameter	Description	starting value	$X_{i,\text{low}}$	$X_{i,\text{upp}}$
c_1	activation ratio	0.1	0.1	1.5
$w_{L0,1}$	half width F-L curve M_1	0.3	0.3	1
$w_{L0,2}$	half width F-L curve M_2	0.3	0.3	1
$L_{off,1}$	pre-stretch M_1	−1.5	−1.5	1.5
$L_{off,2}$	pre-stretch M_2	−1.5	−1.5	1.5

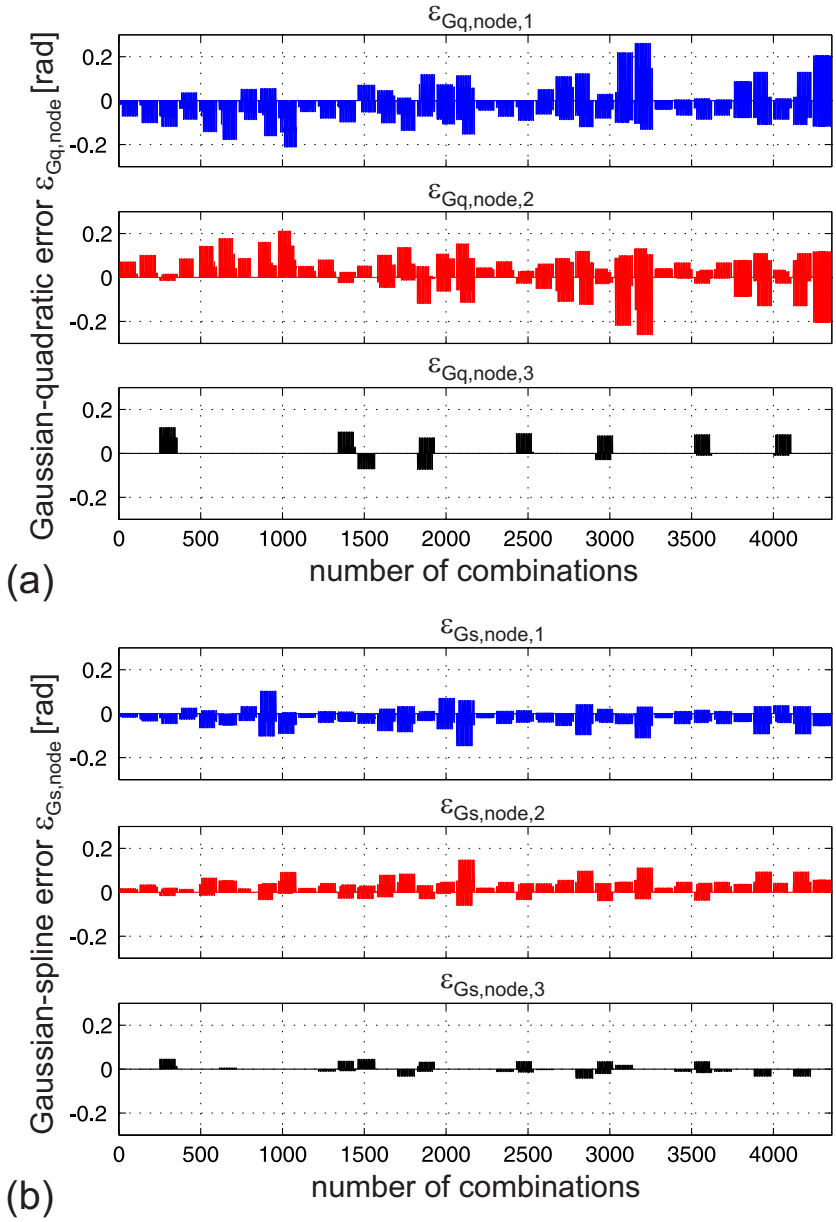

Fig. 2.14: (a) Prediction error of the node positions when adopting the quadratic force-length function with respect to the Gaussian case. Missing bars: node does not exist. (b) Same as (a) but when the cubic spline interpolation is used.

as a nonlinear function, normalized to slack length and maximum muscle force F_{max} (Zajac, 1989). This model has been integrated in series to the muscle model and simulations were performed adopting the Gaussian approximation and muscle parameters as in Section 2.3.2. Three different values of the tendon slack length were evaluated. Figure 2.15 shows the simulation results in terms of stiffness over the joint angle when a very stiff tendon is introduced into the model [compare with fig. 2.12(b)].

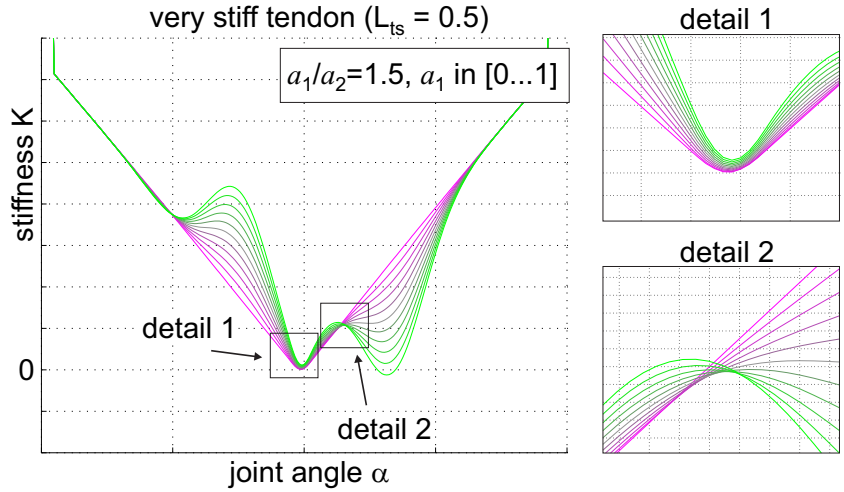

Fig. 2.15: Stiffness against the joint angle for different activations when a very stiff tendon is inserted in series with the muscle. Higher activation is shown in green. In the insets, two details, "detail 1" and "detail 2", of the stiffness plot are shown which illustrate that no nodes turn up.

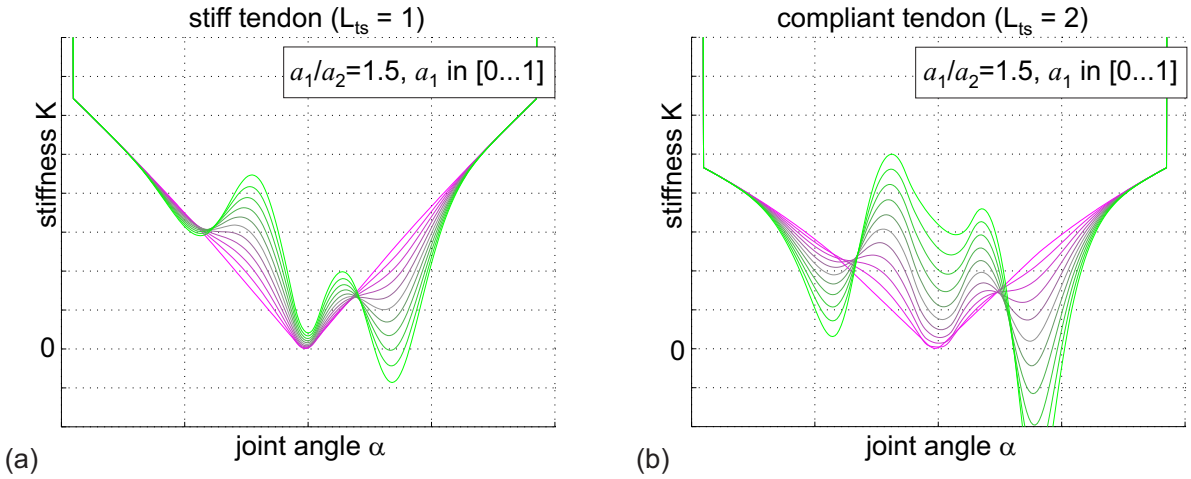

Fig. 2.16: Stiffness over the joint angle for two different tendon slack lengths and for different activations. Higher activation is in green. (a) Joint stiffness obtained when a stiff tendon ($L_{ts} = 1$) is integrated in series with the muscle model. (b) Same as (a) but for a compliant tendon ($L_{ts} = 2$).

In fig. 2.16(a) the situation is depicted in which the tendon is less stiff while fig. 2.16(b) shows the stiffness over the joint angle for a compliant tendon. The more compliant the tendon is, the more the stiffness node turns to a region of low stiffness variation.
An important effect due to the introduction of a compliant tendon into the muscle model is that the stiffness range becomes larger for increasing co-activation. This effect can be expected as the muscle generates higher force, which pulls at the serial nonlinear spring thus increasing the overall stiffness magnitude.

2.4 Summary

This chapter has presented the different implications of muscle actuation such as joint stiffness control, torque generation and mechanical impedance properties. Muscles are modeled using a Hill-type model and a simple joint geometry – a hinge joint with a pulley – is assumed to model a simplified version of the human elbow. Two muscles are integrated in an antagonistic setup and the mechanical impedance of the muscle-driven hinge joint was analyzed (Section 2.1). In Section 2.2, joint stiffness and damping generated by a pair of antagonistic muscles driving a hinge joint with a pulley were examined for different activations. It was shown that, in principle, in an antagonistic co-activated muscle pair it is possible to achieve simultaneous control of joint torque and stiffness. A careful analysis of the stiffness shows that dependent on some parameters of the musculoskeletal setup (length of muscles, width of the force-length curves, pre-stretched arrangement of the muscles, lever arm), positions in the angular joint range of motion can be found for which co-contraction does not lead to a change of the joint stiffness. For this property, the notion of "stiffness nodes" was introduced and its mathematical formulation was provided (Section 2.3). The force-length muscle curve was approximated with a quadratic and a Gaussian expression. The stiffness node position evaluation results in differential operation difficulties for the quadratic representation and numerical complications for the Gaussian expression. To overcome these issues, a cubic spline interpolation was sought (Section 2.3.3). A comparison of stiffness nodes position prediction adopting the quadratic approximation and the spline interpolation with respect to the Gaussian case shows that the spline interpolation is four times more precise than the quadratic case. The chapter ended with an evaluation of the joint stiffness with a tendon integrated into the muscle model (Section 2.3.5).

Chapter 3

Control approaches to increase the stiffness variability in multi-muscle driven joints

The scientific results of this chapter were published in the journal *Bioinspiration & Biomimetics* (Annunziata et al., 2011). This manuscript includes Jan Paskarbeit and Axel Schneider as co-authors. The author carried out the simulations for the concurrent torque/stiffness control with two and four muscles and the design/implementation of the stiffness node controller of Section 3.2. The optimization process of Section 3.3 and the design and simulation of different control approaches as proposed in Section 3.4 were carried out in collaboration with the co-authors.

3.1 Introduction

In Chapter 2 it was shown that depending on the muscle and joint parameters, domains might occur in the joint angular range for which stiffness variability is limited (low stiffness variation) or even impossible (stiffness nodes). In order to design novel control strategies for simultaneous control of torque and stiffness in a hinge joint actuated by antagonistic muscles, a pure concurrent torque/stiffness control implementing co-activation is tested (Section 3.2). Since it is expected that such an approach will fail when a stiffness node is nearby, an additional pair of muscles is added to the joint which results in additional DoFs that can be used for the control problem. One control strategy that takes advantage of the additional muscle pair, handles stiffness nodes by shifting them away from the current joint position and thus regaining stiffness controllability. To prevent domains of low stiffness variation, an optimal muscle configuration is sought and finally defined which allows for a maximal stiffness variation across a wide joint angular range (Section 3.3). Based on this optimal configuration, four additional control strategies are proposed and tested which deliver stiffnesses and torques comparable to those obtained in the optimal case. The strategies combine torque control and stiffness control by co-activation with novel ideas such as activation overflow and an inverse model approach. All strategies are tested in simulation and the results are compared with those of the optimal setup (Section 3.4). In this study, no specific biological example is

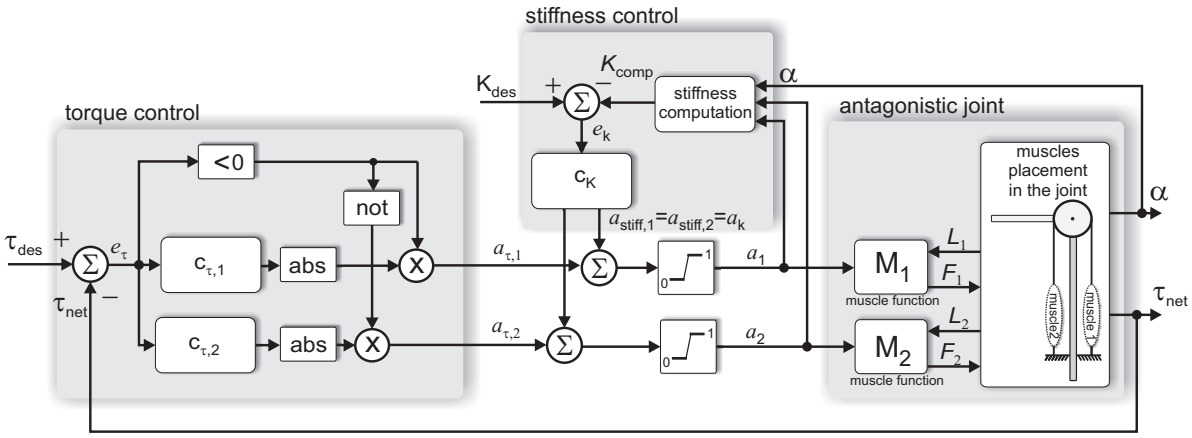

Fig. 3.1: Concurrent torque and stiffness control for an antagonistic joint setup with a pulley. On the right side, two muscles (M_1 and M_2) are integrated in the antagonistic hinge joint setup. Forces F_1 and F_2 are generated by muscle functions based on the activation levels a_1 and a_2. The torque control on the left side activates either the agonistic ($a_{\tau,1}$) or antagonistic ($a_{\tau,2}$) muscle in dependence of the desired joint torque. The stiffness control on the top generates the same activation (a_k) for both muscles. Both controllers are of the proportional type. The muscle activations are limited to 1.

simulated. Therefore, the values of variables used in all models are expressed as relative and thus dimensionless numbers (arbitrary units, cmp. Tables 3.1, 3.2, 3.3, 3.4, 3.5). Dimensionless force-length relationship and values for the parameters have been selected such that the maximum muscle force and torque at the pulley wheel is one for maximum activation (e.g. also the pulley radius is one) to simplify the analysis. Nevertheless, the problem statements and conclusions remain valid when adjusted to realistic parameters. It must be emphasized that also time responses are dimensionless. Real time responses scale e.g. in dependence of maximum muscle force F_{max}, etc.

3.2 Concurrent torque/stiffness control in the presence of stiffness nodes

Based on the stiffness node examination carried out in Chapter 2, in this section the design of a concurrent torque and stiffness control will be introduced for the special case in which the lever arm is fixed. It will be shown that in the absence of a stiffness node, torque and stiffness can be set independently. However, if the stiffness node is present, the controller cannot set the desired stiffness around the node position. The concurrent torque and stiffness control is shown in fig. 3.1. The torque controller (on the left side) is of the proportional type and activates either muscle 1 (M_1) or muscle 2 (M_2) depending

Table 3.1: Simulation parameters.

Parameter	Description	Value
r	pulley radius	1
$J_{arm,model}$	pulley moment of inertia	1000
$c_{\tau,1}$	prop. gain torque cont.1	30
$c_{\tau,2}$	prop. gain torque cont.2	30
c_k	prop. gain stiffness cont.	5

on the desired joint torque (reciprocal activation). The activation output is converted into a torque by an antagonistic joint setup (right side). This torque is used to close the feedback loop. In order to change the stiffness of the joint setup, the co-activation strategy is adopted. Therefore, another controller is needed that activates both muscles at the same time. For this purpose, a stiffness control is added to the system (top box). Using the activation levels of the two muscles and the actual angular position of the joint, the stiffness of the system can be computed through equation (2.16). This computed stiffness value is compared with the desired stiffness and the error is then converted into equal activation levels for both muscles by a proportional controller.
Two simulations are performed. The first in absence of a stiffness node and the second when a stiffness node is close to the joint position. Joint and control parameters adopted in the simulations are listed in Table 3.1. The muscle parameters for the first simulation are listed in Table 2.4 (column: *No node occurrence*), which corresponds to the joint stiffness configuration plotted in fig. 2.11(a). The controllers and the antagonistic joint are modeled using Matlab/Simulink 7.5 (The MathWorks Inc., Natick, MA, USA). To held the angular position constant at $\alpha = 0.05$, in an experimental setup, the lever arm would be clamped. In simulation, a high inertia of the lever arm is assumed[1] (see Table 3.1). This strategy was chosen to set the values of the system parameters and to study quasi-static situations. The results are also valid for other quasi-static situations in which the inertia of the lever is lower. Figure 3.2 depicts the simulation results of the concurrent torque/stiffness control for a fixed position and for the *No node occurrence*. The torque and the stiffness are changed in the absence of a stiffness node. The torque controller is activated at $t = 1$, the stiffness controller at $t = 3$. Beside a small error due to the usage of proportional controllers, both desired stiffness and desired torque are reached. The torque output is only insignificantly influenced by the change of the stiffness.
In the second simulation, all parameters are the same as those adopted for the first one except the pre-stretch $L_{off,2}$ which is changed in such a way that a stiffness node occurs close to the joint angular position [the muscle parameters are listed in Table 2.4 (column: *Node occurrence*)] and correspond to the joint stiffness configuration plotted in 2.12(a). In this case a stiffness node at α=0.05 occurs. Figure 3.3 shows the torque/stiffness

[1]Assuming a high inertia of the lever arm, a deviation of the angular position of 0.001 rad at t=6 is obtained in simulation.

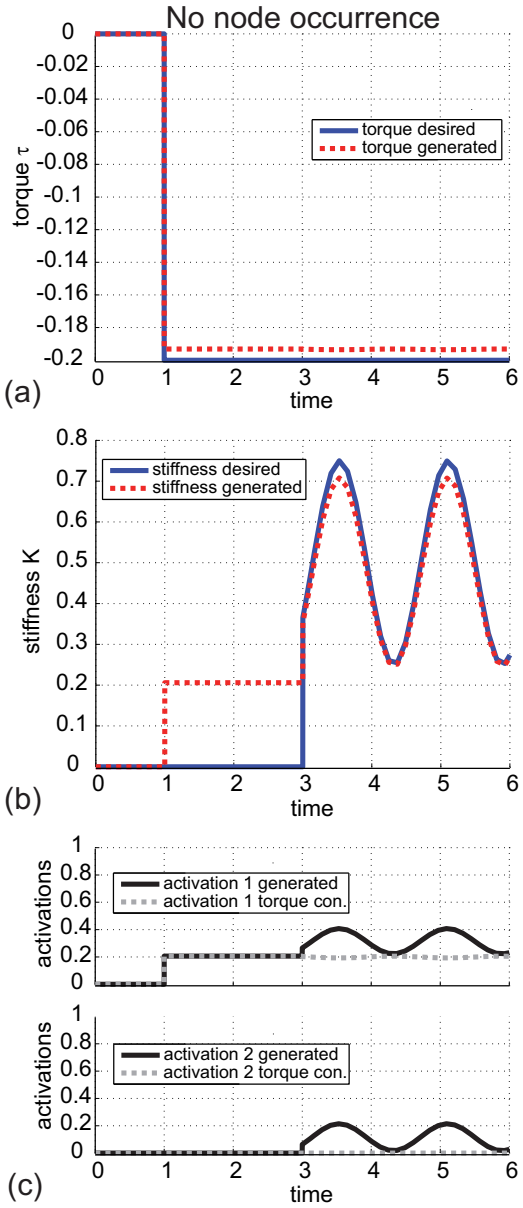

Fig. 3.2: Simulation results of the concurrent torque/stiffness control for an antagonistic muscle pair in a hinge joint setup for the case in which no node is present around the angular joint position. At t=1 the torque controller is switched on; torques are shown in (a). At t=3 the stiffness controller is switched on. Stiffnesses are shown in (b). Beside a small error due to the usage of proportional controllers, the desired values for torque and stiffness are reached. Total activation 1 and activation 2 are shown as black curves in (c). The only torque controller activation contributions are shown as dashed gray curves.

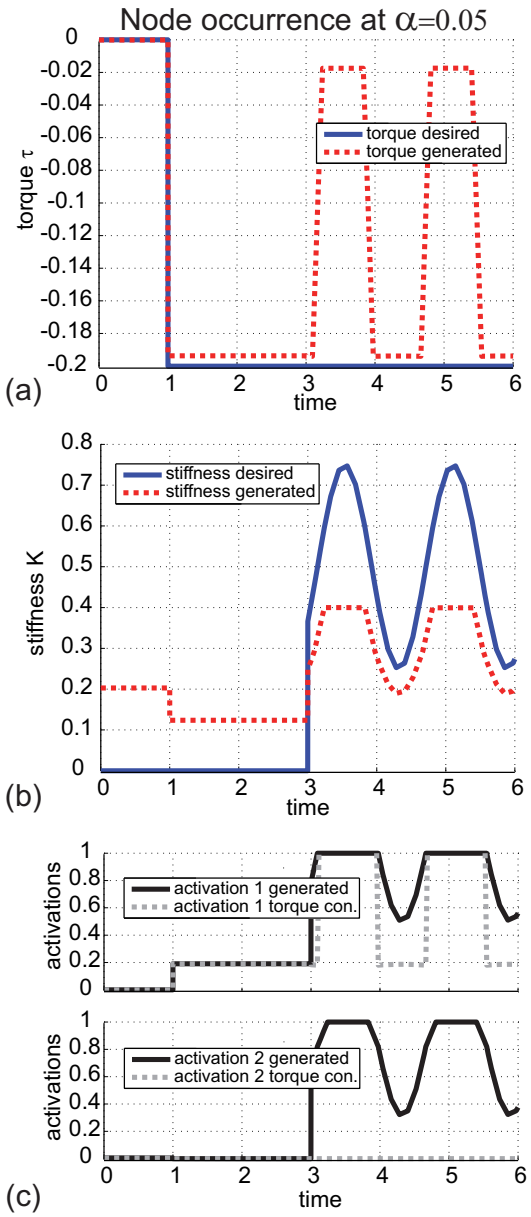

Fig. 3.3: Simulation results of the concurrent torque/stiffness control for an antagonistic muscle pair in a hinge joint setup for the case in which a node is present around the angular joint position. The lever arm is kept at a joint angle $\alpha = 0.05$ assuming high inertia. At t=1 the torque controller is switched on; torques are shown in (a). At t=3 the stiffness controller is switched on [stiffnesses are shown in (b)] but this time the desired stiffness cannot be reached although both activations are driven to their limits (c).

control simulation results. Due to the change of the pre-stretch, the stiffness of the system is non-zero during the first second of the simulation although both activations are set to zero. This is caused by the passive force-length function. At $t = 1$ the torque

controller is turned on and the desired torque, beside a small error due to the usage of a proportional controller, is reached. At $t = 3$, the stiffness controller is also switched on but in contrast to the *No node occurrence* the ability to reach higher stiffnesses is reduced significantly although both activation signals are at their maximum value [fig. 3.3(c)]. Moreover, since the activation level is maximal for both muscles, the actual torque deviates considerably from the desired value [fig. 3.3(a)]. This result shows that for the simultaneous control of torque and stiffness the setup with two muscles is coupled and therefore not fully controllable. The conclusion is that, given a fixed set of joint and muscle parameters, the number of DoFs available to control the system is not enough for designing a control strategy able to overcome the presence of a stiffness node. Therefore, any concurrent torque/stiffness controller is bound to fail.

3.2.1 Stiffness generated by two muscle pairs in a pulley joint

With the objective of decoupling the control of torque and stiffness, at least one further DoF has to be added to the joint system. The introduction of a third muscle in the setup adds an additional DoF that can be used to decouple the control of torque and stiffness in cases in which controllability is reduced and to cope with the potential occurrence of a stiffness node. In this study, two instead of one additional muscles are introduced to allow symmetric joint operation. Figure 3.4(a) shows the antagonistic setup with four muscles pulling at the hinge joint. Similar to the two-muscles setup, also for this configuration the joint stiffness can be obtained in a closed formula. The region borders can be explicitly found, too. The borderlines of these regions occur at those positions in the angular space of the joint where the active force-angle curves have their root. Figure 3.4(b) depicts regions and force-angle relations adopting the values reported in Table 3.2 (column: *No node occurrence*). The configuration with four muscles allows the design of a suitable control strategy to get rid of the influence of stiffness nodes. For example, the stiffness controller can adopt co-contraction of two antagonistic muscles while the torque control could be realized by differential actuation of the remaining two muscles. In this way, the control problem could be decoupled. Despite the decoupling, it can still be expected that the interplay of control strategies generates combinations of the

Table 3.2: Muscle parameters for the analysis of the stiffness for a four-muscles hinge joint setup with a pulley wheel.

		No node occurrence				Node occurrence			
Par.	Description	M_1	M_2	M_3	M_4	M_1	M_2	M_3	M_4
L_{off}	pre-stretch	0.0	−0.025	0.0	0.0	0.0	0.0	−0.025	0.0
w_{L0}	half width F-L curve	0.5	0.5	0.8	1	0.5	0.8	0.5	1
F_{max}	max. isometric force	1	1	1	1	1	1	1	1
K_p	passive curve const.	2	2	2	2	2	2	2	2

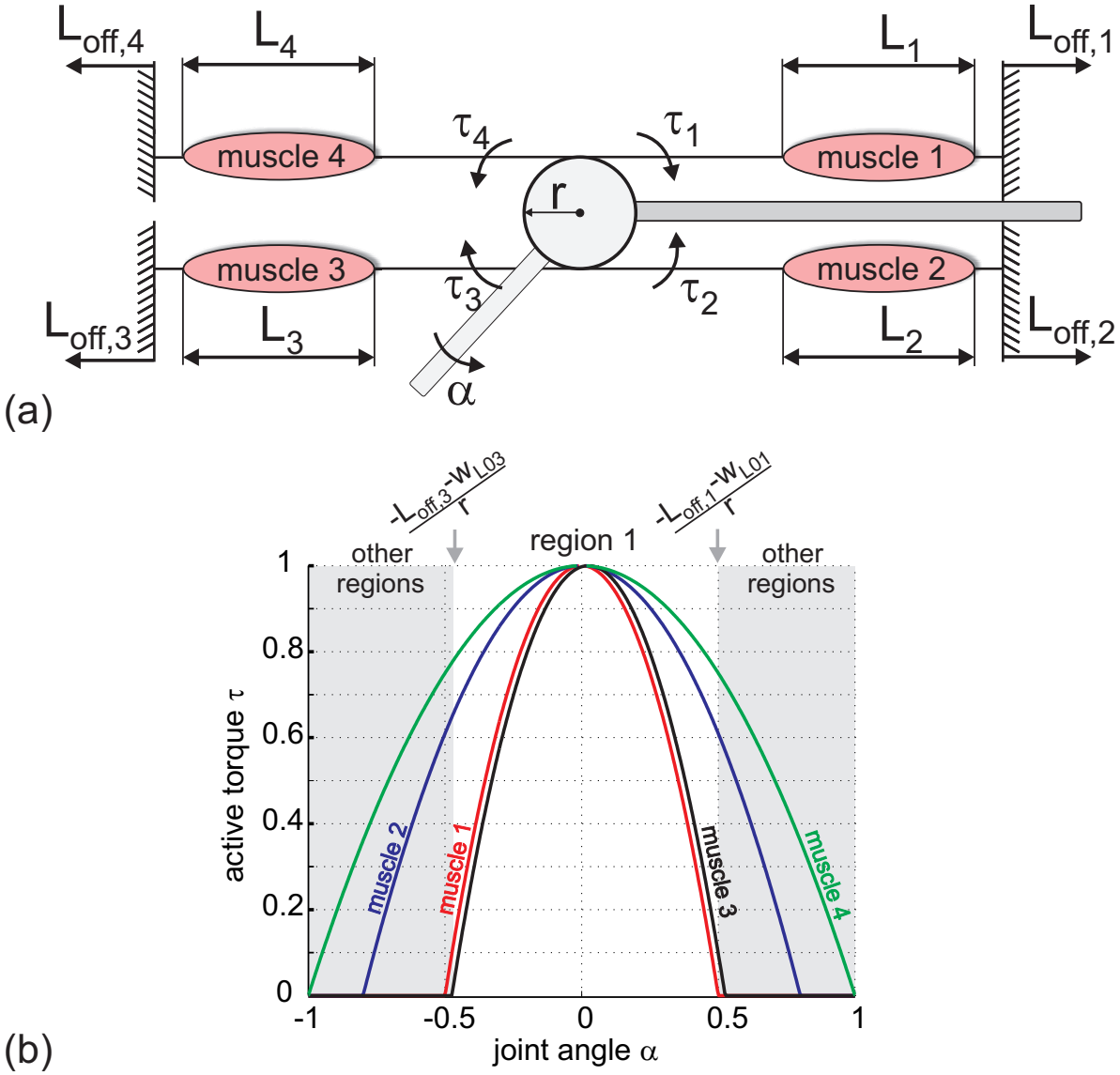

Fig. 3.4: (a) Four muscles integrated in a hinge joint setup using a pulley wheel. L_1, L_2, L_3 and L_4 are the muscle lengths. The values $L_{off,1}$, $L_{off,2}$, $L_{off,3}$ and $L_{off,4}$ represent the muscle pre-stretch. α indicates the joint angle. (b) Active force-length curves in a hinge joint generated by two antagonistic muscle pairs plotted over the joint angle. The force contribution for each muscle is depicted in red (muscle 1), blue (muscle 2), black (muscle 3) and green (muscle 4), respectively. Their overlap in the joint angle space defines different regions. The region in the middle is called *region 1* in the figure. The mathematical expressions for the angular positions of the region borders are given at the top.

four activations a_1, a_2, a_3 and a_4 for which stiffness nodes can occur. For 4 muscles, all possible combinations of the active force-length curves overlap, deliver up to 15 regions

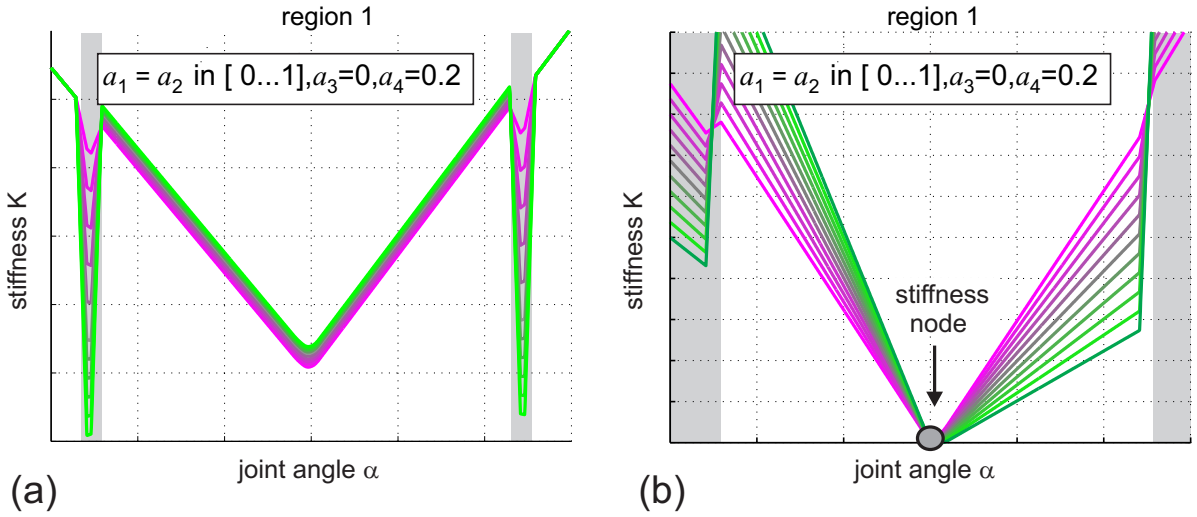

Fig. 3.5: (a) Stiffness generated by the setup of fig. 3.4(b) when using a co-activation strategy for M_1 and M_2. In this case no stiffness nodes occur but the range of stiffness change is limited. (b) Same as (a) but exchanging the muscle parameters among M_2 and M_3 leads to the appearance of a stiffness node.

at which correspond a maximum of 15 possible stiffness nodes. Figure 3.5(a) shows the joint stiffness generated at the hinge joint for increasing co-activation of muscle 1 and 2 and a constant differential activation among muscle 3 and 4. The plot shows that even though no stiffness nodes occur, the possible stiffness variation might still be limited. Therefore, later in this study the question is posed what an optimal muscle setup might look like (Section 3.3). Optimal in this case refers to the ability to generate a maximal stiffness variation across a given angular joint range of motion. Figure 3.5(b) shows the stiffnesses for the same configuration as in (a) but with exchanged parameters between M_2 and M_3 [see Table 3.2 (column: *Node occurrence*)]. In this case a stiffness node in *region 1* occurs. The position of the stiffness node $\alpha_{node,1}$ occurring in *region 1* is given by the following expression obtained with the quadratic force-length approximation:

$$\alpha_{\text{node},1}(a_1,a_2,a_3,a_4) = \frac{\frac{a_1\,\mathrm{F_{max,1}}\,\mathrm{L_{off,1}}\,\mathrm{r}^2}{\mathrm{w}^2_{\mathrm{L0,1}}} + \frac{a_2\,\mathrm{F_{max,2}}\,\mathrm{L_{off,2}}\,\mathrm{r}^2}{\mathrm{w}^2_{\mathrm{L0,2}}}}{-\frac{a_1\,\mathrm{F_{max,1}}\,\mathrm{r}^3}{\mathrm{w}^2_{\mathrm{L0,1}}} + \frac{a_2\,\mathrm{F_{max,2}}\,\mathrm{r}^3}{\mathrm{w}^2_{\mathrm{L0,2}}} - \frac{a_3\,\mathrm{F_{max,3}}\,\mathrm{r}^3}{\mathrm{w}^2_{\mathrm{L0,3}}} + \frac{a_4\,\mathrm{F_{max,4}}\,\mathrm{r}^3}{\mathrm{w}^2_{\mathrm{L0,4}}}} + \frac{\frac{a_3\,\mathrm{F_{max,3}}\,\mathrm{L_{off,3}}\,\mathrm{r}^2}{\mathrm{w}^2_{\mathrm{L0,3}}} + \frac{a_4\,\mathrm{F_{max,4}}\,\mathrm{L_{off,4}}\,\mathrm{r}^2}{\mathrm{w}^2_{\mathrm{L0,4}}}}{-\frac{a_1\,\mathrm{F_{max,1}}\,\mathrm{r}^3}{\mathrm{w}^2_{\mathrm{L0,1}}} + \frac{a_2\,\mathrm{F_{max,2}}\,\mathrm{r}^3}{\mathrm{w}^2_{\mathrm{L0,2}}} - \frac{a_3\,\mathrm{F_{max,3}}\,\mathrm{r}^3}{\mathrm{w}^2_{\mathrm{L0,3}}} + \frac{a_4\,\mathrm{F_{max,4}}\,\mathrm{r}^3}{\mathrm{w}^2_{\mathrm{L0,4}}}} \tag{3.1}$$

and the region of existence is:

$$w_{L01} > |L_{\text{off},1} + r\cdot\alpha| \;\wedge\; w_{L02} > |L_{\text{off},2} - r\cdot\alpha| \;\wedge$$
$$w_{L03} > |L_{\text{off},3} + r\cdot\alpha| \;\wedge\; w_{L04} > |L_{\text{off},4} - r\cdot\alpha| \;. \tag{3.2}$$

In the following, the attention will be focused on the design of a control approach for the joint setup with four muscles which is able to shift the node $\alpha_{node,1}$ away when it occurs.

3.2.2 Control approach adopting reciprocal activation and co-activation (dedicated muscles)

The use of two pairs of antagonistic muscles for driving the hinge joint adds additional DoFs that can be used in the control strategy for shifting the node and therefore enabling the torque and stiffness controllers to reach the desired values. In the following, a separate torque and stiffness control scheme for the joint setup with four muscles is combined with an additional controller that shifts the node away when the angular position of the joint approaches the node position. According to the function principle, the control strategy is called *stiffness node control*. Equation (3.1) gives the position of the stiffness node in *region 1*. A change in any activation influences the node position. With the objective to find out the activation that influences the node position the most, the partial derivatives of equation (3.1) with respect to all four activations have to be analyzed:

$$\left\{ \frac{\partial \alpha_{\mathrm{node,1}}}{\partial a_1}, \frac{\partial \alpha_{\mathrm{node,1}}}{\partial a_2}, \frac{\partial \alpha_{\mathrm{node,1}}}{\partial a_3}, \frac{\partial \alpha_{\mathrm{node,1}}}{\partial a_4} \right\} \quad . \tag{3.3}$$

The activation with the strongest influence on the stiffness node position corresponds to the biggest absolute partial derivative in (3.3). This idea will be used for the development of a node control strategy. Figure 3.6 shows the simultaneous torque/stiffness control with the additional stiffness node control. A dedicated muscle pair is adopted by the stiffness control which acts on M_1 and M_2 implementing co-activation. The torque control acts on one of the remaining two muscles M_3 or M_4 in dependence of the desired torque direction (reciprocal activation). As it is explained below, the stiffness node control chooses one out of the four activations to shift away the node position.
The torque controller is of PI type and provides the activations for the muscles to set the joint torque. With the torque error e_τ, the control strategy can be written as

$$a_{\tau,3} = \left(\mathrm{c_{p,\tau}} \cdot |e_\tau| + \mathrm{c_{i,\tau}} \cdot \int |e_\tau| \ \mathrm{dt} \right) \cdot \phi$$
$$a_{\tau,4} = \left(\mathrm{c_{p,\tau}} \cdot |e_\tau| + \mathrm{c_{i,\tau}} \cdot \int |e_\tau| \ \mathrm{dt} \right) \cdot \overline{\phi}$$

with $\mathrm{c_{p,\tau}}$ and $\mathrm{c_{i,\tau}}$ being the proportional and integral controller gains, respectively. The activations can only be positive, therefore the absolute value of the torque error is considered. The variable ϕ is used to generate the torque in the desired angular direction and here is adopted to activate either M_3 or M_4 in this way:

$$\phi = \begin{cases} 1 & e_\tau < 0 \\ 0 & e_\tau \geq 0 \end{cases} .$$

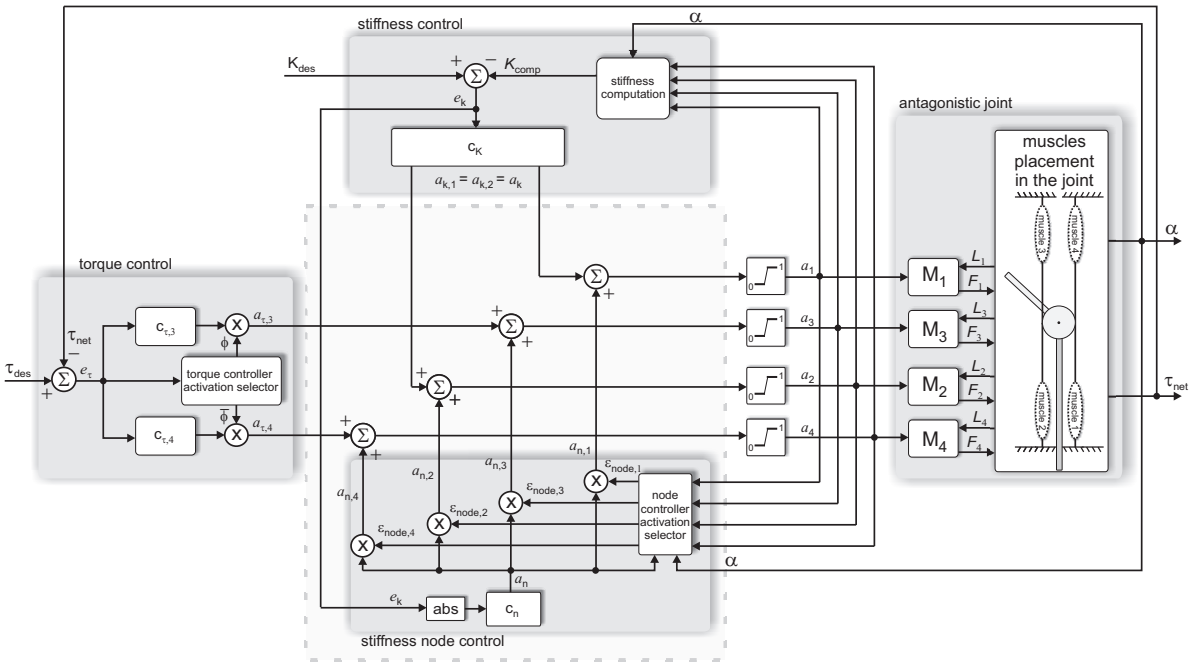

Fig. 3.6: Simultaneous torque/stiffness control for the antagonistic setup composed by two muscle pairs in a pulley joint. On the right side, four muscles (M_1–M_4) are integrated in the antagonistic setup. Based on the activation a_1–a_4, the muscle forces F_1–F_4 are generated. The torque control (on the left side) acts on M_3 and M_4 activating either the agonistic ($a_{\tau,3}$) or the antagonistic ($a_{\tau,4}$) muscle in dependence of the joint torque error (e_τ). The stiffness control (at the top) activates M_1 and M_2 with the same value (a_k) (co-activation). If a node is close to the angular joint position, the stiffness node control (at the bottom, enclosed in a rectangular dashed line) adds an offset to the activation which influences the node position the most with the objective to shift the stiffness node away. All activations are limited to 1.

The stiffness controller is also of PI type and provides the activations to the muscles to reach the desired stiffness $\mathrm{K_{des}}$. The computed stiffness K_{comp} is calculated in the *stiffness computation* box (on the top of fig. 3.6).

Therefore, starting from the stiffness error

$$e_{\mathrm{k}} = \mathrm{K_{des}} - K_{\mathrm{comp}},$$

the stiffness controller generates the control value

$$a_{\mathrm{k}} = \mathrm{c_{p,k}} \cdot e_{\mathrm{k}} + \mathrm{c_{i,k}} \cdot \int e_{\mathrm{k}}\ \mathrm{dt}$$

with the proportional and integral controller gains $\mathrm{c_{p,k}}$ and $\mathrm{c_{i,k}}$. The stiffness activation can also be negative; therefore here the signed error is considered.

3.2.3 Stiffness node control strategy

A node in the vicinity of the actual joint position decreases the ability to control the stiffness. In this section, a stiffness node control is introduced which is able to shift a potential node away. The stiffness node control is designed such that one among the four available activations is modified to accomplish the goal. The main idea is based on the addition or subtraction of a certain offset activation a_{n} to/from a selected activation. The activation is selected based on the stiffness error e_{k}. The offset sign (addition/subtraction) depends on the direction of the desired node shifting movement (with respect to the actual joint position). The procedure for selecting the activation and the sign is realized according to the following strategy. First, the muscle with the strongest influence on the node position is selected [biggest absolute value of (3.3)]. Second, the sign variable $\epsilon_{\mathrm{node},j}$ (see below) is set according to the partial derivative of the node function and the relative position of node and joint i.e. it determines whether the activation has to be increased or decreased. If the activation $a_{\mathrm{n},j}$ (with j indicating the muscle, j in [1,2,3,4]) of the selected muscle is already saturated at 1 and an increase is desired or if the activation is 0 and a decrease is desired, the second best muscle is selected. In this case, both torque and stiffness will present jumps which lead to a longer transient in the control response. The direction of the node controller activation depends on the slope of the gradient: If it is negative, an increase of the activation $a_{\mathrm{n},j}$ pushes the node to the left, while if it is positive, an increase of the activation $a_{\mathrm{n},j}$ pushes the node to the right. The sign $\epsilon_{\mathrm{node},j}$ of the activation contribution $a_{\mathrm{n},j}$, is mathematical defined as follows:

$$\epsilon_{\mathrm{node,j}} = \begin{cases} 1 & \text{slope} > 0 \ \wedge \ (\alpha - \alpha_{\mathrm{node},1}) < 0 \\ -1 & \text{slope} < 0 \ \wedge \ (\alpha - \alpha_{\mathrm{node},1}) < 0 \\ 1 & \text{slope} < 0 \ \wedge \ (\alpha - \alpha_{\mathrm{node},1}) \geq 0 \\ -1 & \text{slope} > 0 \ \wedge \ (\alpha - \alpha_{\mathrm{node},1}) \geq 0 \end{cases} .$$

As example, if the node $\alpha_{\mathrm{node},1}$ is on the left side of the actual joint position α, it has to be pushed more to the left to avoid an occurrence in the joint working range. According to the slope of the gradient, the activation $a_{\mathrm{n},j}$ has to increase ($\epsilon_{\mathrm{node},j} = 1$) if the slope is negative and decrease ($\epsilon_{\mathrm{node},j} = -1$) if the slope is positive (cmp. fig. 3.7). The node controller contribution $a_{\mathrm{n},j}$ for the selected activation can be expressed as:

$$a_{\mathrm{n},j} = \left(\mathrm{c_{p,n}} \cdot |e_{\mathrm{k}}| + \mathrm{c_{i,n}} \cdot \int |e_{\mathrm{k}}| \ \mathrm{dt} \right) \cdot \epsilon_{\mathrm{node,j}} \quad .$$

3.2.4 Simulation results for a fixed joint position

The effect of the stiffness node control on the performance of a simultaneously working torque/stiffness control when the joint angle is close to a stiffness node is shown in fig. 3.8. Subplots (a)-(b) show the torque and the stiffness with the stiffness node control switched off. The torque controller is turned on at $t = 1$, the stiffness controller at $t = 2$.

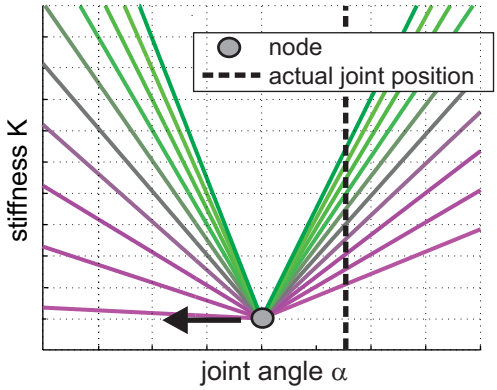

Fig. 3.7: A node is close to the actual joint angle and lies on its left hand side. In order to push it away, the node controller has to push it further to the left. Therefore, the activation contribution $a_{n,j}$ has to be positive if the gradient has a negative slope or negative if the gradient has a positive slope.

The desired torque is reached while the desired stiffness cannot be reached although activations a_1 and a_2 are saturated [subplot (c)] indicating highest possible co-contraction. The controllers and the four muscles joint setup were modeled in Matlab/Simulink 7.11 (The MathWorks Inc., Natick, MA, USA). To held the angular position constant at $\alpha = 0$, in an experimental setup, the limb segment would be clamped. In simulation, a high inertia of the limb segment is assumed[2]. Table 3.3 reports the joint and control parameters used in the simulation. Also in this case the results presented are valid for other quasi-static situations in which the inertia of the limb is lower.

Figure 3.9(a)-(d) depicts the simulation results for the case in which the stiffness node

Table 3.3: Simulation parameters for the torque/stiffness/node controller for a setup with four muscles driving a pulley wheel hinge joint [muscle parameters are given in Table 3.2 (column: *Node occurrence*)].

Parameter	Description	Value
r	pulley radius	1
$J_{arm,model}$	pulley moment of inertia	1000
$c_{p,\tau}$	prop. gain torque contr.	0.8
$c_{i,\tau}$	integ. gain torque contr.	20
$c_{p,k}$	prop. gain stiffness contr.	1
$c_{i,k}$	integ. gain stiffness contr.	5
$c_{p,n}$	prop. gain node contr.	0.2
$c_{i,n}$	integ. gain node contr.	5

[2]The angular position shows a deviation of 0.002 rad at t=6 in simulation.

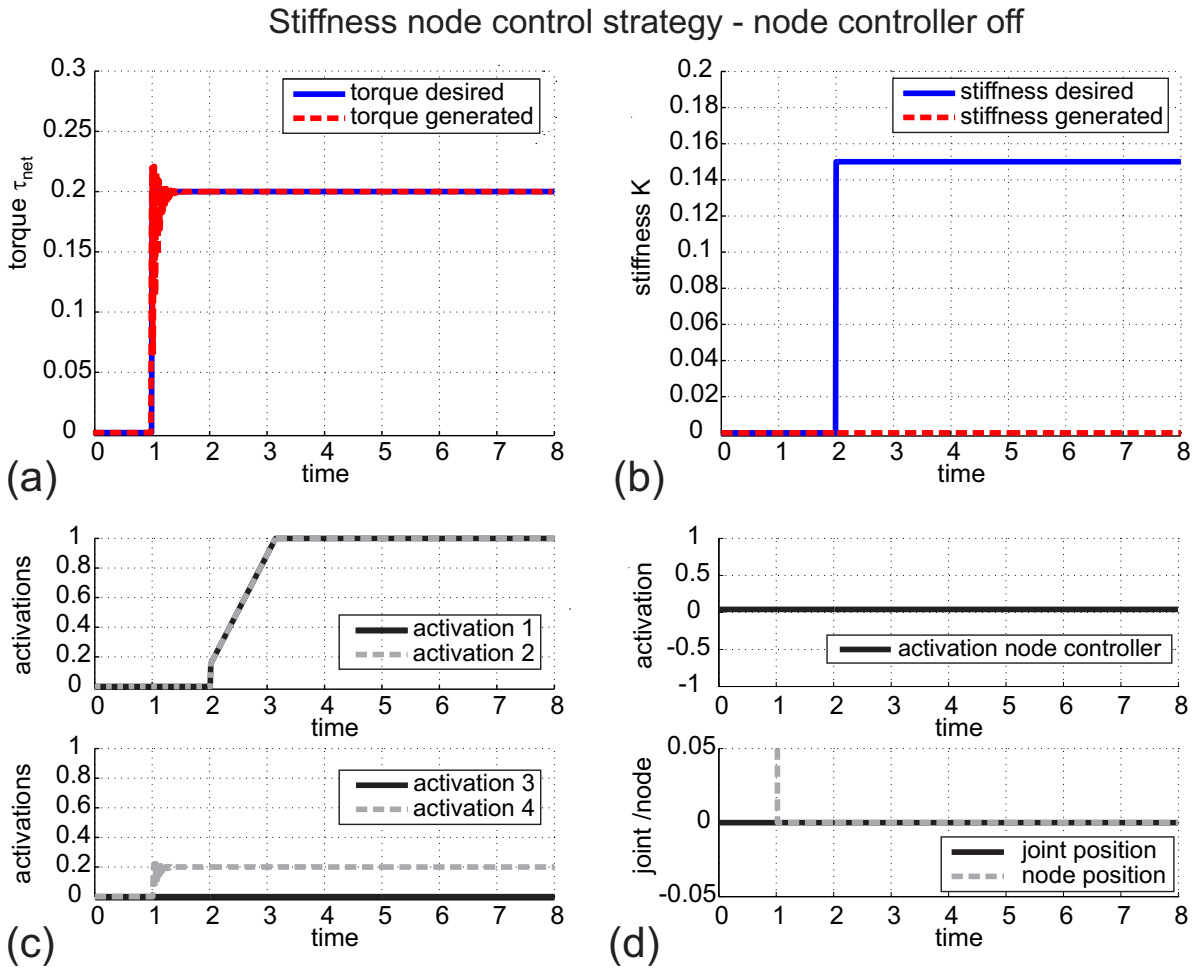

Fig. 3.8: Simulation results of the concurrent torque/stiffness control for two antagonistic muscle pairs in a hinge joint setup when the stiffness node controller is not operating. The joint is fixed at a joint angle $\alpha = 0$. At $t = 1$ the torque controller is turned on (a). At $t = 2$ the stiffness controller is also turned on (b). The desired torque is reached (a), while the desired stiffness is not (b), although both activations a_1 and a_2 responsible for the control of the stiffness are driven to the maximum values (c, top). The node controller activation is zero over the complete test as it was left switched off (d, top). The joint position corresponds to the node position (d, bottom).

controller is switched on. Both desired stiffness and desired torque are reached [cmp. fig. 3.9(a) and (b)] because the stiffness node control has shifted the node away [cmp. joint and node position in fig. 3.9(d)]. At $t = 2$ the net-torque is disturbed by the node controller action (an activation offset is added to activation a_3) but the torque controller compensates this disturbance by increasing a_4 [cmp. fig. 3.9(c)].

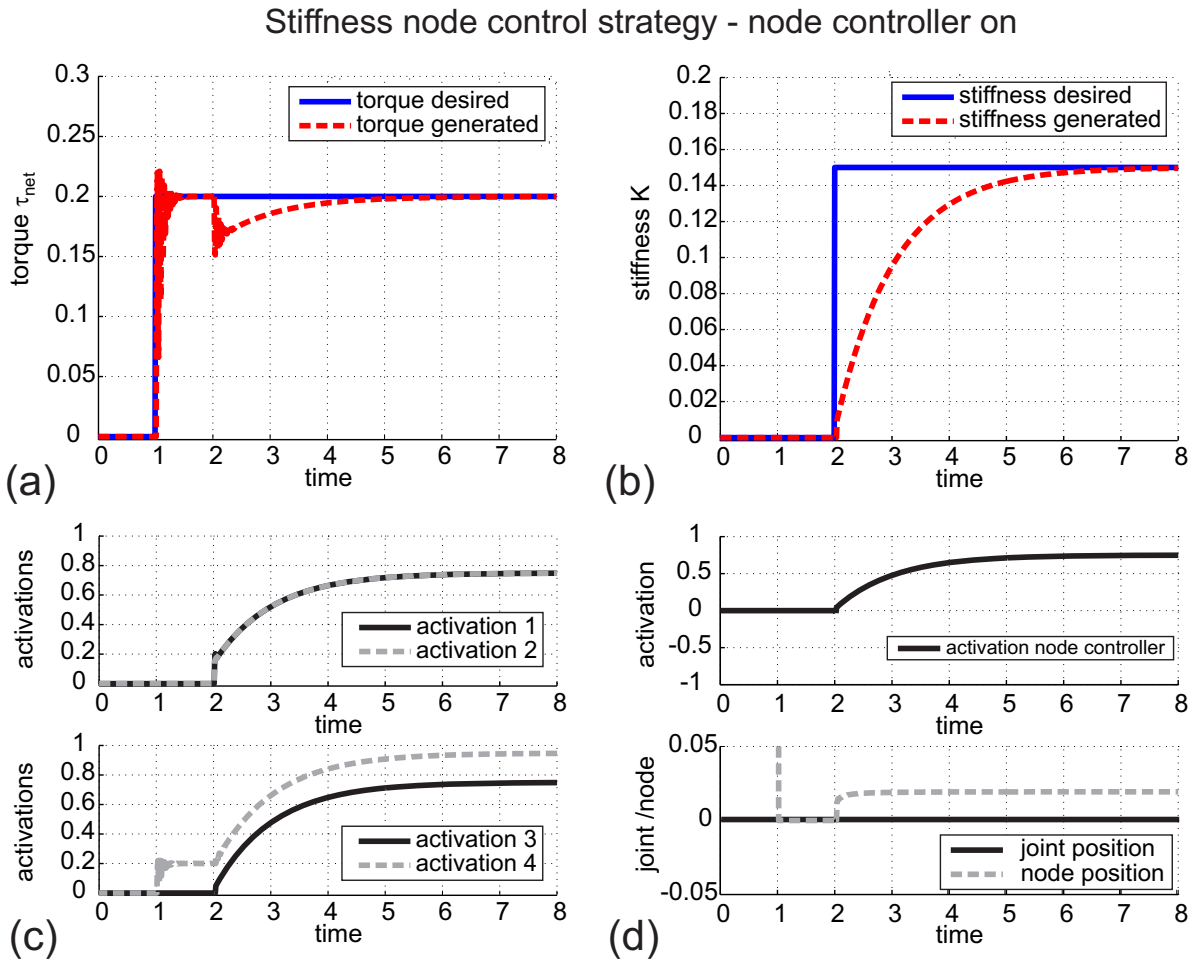

Fig. 3.9: Simulation results of the concurrent torque/stiffness control for two antagonistic muscle pairs in a hinge joint setup with a stiffness node controller. The joint is fixed at a joint angle $\alpha = 0$ which corresponds to the node position. At $t = 1$ the torque controller is turned on (a). At $t = 2$ the stiffness controller (b) and the stiffness node controller (d, top) are also turned on. Both desired torque and stiffness values are reached (a-b) because the node is shifted away from the joint position (d, bottom).

3.3 Optimal stiffness variation across a wide joint range of motion

It has been mentioned before that even without the occurrence of a stiffness node the range of possible joint stiffness variation can be small [cmp. fig. 3.5(a)]. In the following, the question is answered what is the maximal and minimal joint stiffness at a given joint angle and torque that can be reached when any combination of all four activations is allowed? Furthermore, how does an optimal hinge joint setup with two antagonistic muscle pairs look like? Optimal in this case means maximal stiffness variation over a

given interval of joint angles. In the following, the hinge joint with a pulley and two antagonistic muscle pairs will be used to answer these questions. The results of this optimization are used in subsequent sections to derive control strategies which generate activation patterns with a stiffness variability that comes close to this optimum.

3.3.1 Muscle parameters optimization process

In this section a set of optimal muscle parameters is sought. The optimization algorithm follows a brute-force approach[3] since the number of parameters is quite small and simulation time for one trial is short. The optimization goal is to find a set of muscle parameters for which *region 1* has a symmetric domain of $[-\frac{\pi}{2}, \frac{\pi}{2}]$ rad in the angular range of motion. For each set of muscle parameters under analysis, the process collects all the torques and stiffnesses generated at each angular position when varying the four activations in the interval $[0, 1]$ with steps of 0.1. Then, the generated torques are sorted into bins of width 0.1 within the interval $[-2, 2]$. After that, for each torque group, the maximum and minimum stiffness are selected. In this way, two stiffness surfaces over the angular and torque ranges can be created corresponding to the maximal and minimal possible stiffness that can be reached.

The process started with a set of muscle parameters x_i $(i = 1...m)$ the range of which was constrained by the lower boundary $X_{i,\text{low}}$ and the upper boundary $X_{i,\text{upp}}$ as reported in Table 3.4. m corresponds to the number of parameters (in our case is 3) times the number of muscles (in our case is 4), which gives $m = 12$. The optimization algorithm finds the set of parameters such that the stiffness variability in the angular working range $[-\frac{\pi}{2}, \frac{\pi}{2}]$ rad is maximized given that the activations span the interval $[0, 1]$ with steps of 0.1. For each set of muscle parameters, n activation patterns are analyzed corresponding to all possible combinations of the four activations[4].

Table 3.4: Muscle parameters used in the optimization process. For each muscle, the muscle parameters are defined with a starting value and a range in which they can vary during the optimization.

			Range of parameter variability	
x_i	Description	starting value	$X_{i,\text{low}}$	$X_{i,\text{upp}}$
L_{off}	pre-stretch	0	$-\pi$	π
w_{L0}	half width F-L curve	1	0.5	2π
K_p	passive curve const.	1	0	2

[3]The algorithm goes through all possible combinations of parameters.

[4]Each activation starts at 0 and increases stepwise of 0.1 till the maximum activation, a=1, is reached.

The objective function $E(x_i)$ to be minimized is defined as the sum of two terms

$$E(x_i) \;=\; \sum_{k=1}^{n} \left[|S_{\max,k} - 1| + (S_{\min,k} - 0) \right] \quad \text{with } S_{\max,k}\,,\, S_{\min,k} \in [0,1]$$

where the first is the absolute difference between the maximum stiffness generated in bin k (denoted as $S_{\max,k}$) and a reference value which was 1. The second is the difference between the minimum stiffness generated in bin k (denoted as $S_{\min,k}$) and a reference value which was 0. $S_{\max,k}$ and $S_{\min,k}$ were limited to the interval $[0,1]$ to favor equally distributed stiffnesses as opposed to high stiffness peaks. The optimization process finds a minimum for $E(x_i)$ solving the following problem:

$$\min_{x_i} E(x_i) \quad \text{such that} \quad X_{i,\text{low}} \leq x_i \leq X_{i,\text{upp}} \;\; .$$

The Matlab function *fmincon* was used for the constrained nonlinear optimization (Coleman and Li, 1992).

3.3.2 Analysis of the optimal muscle setup

Table 3.5 lists the muscle parameters that resulted from the above described optimization process (for completeness, F_{max} is also listed even if it was not part of the optimization). Figure 3.10(a) shows the torque curves generated by the four muscles in the case of maximum activation (a_1=a_2=a_3=a_4=1), when the muscle parameters of the optimization process are used. As desired, the main working range covers the angular joint range of motion from $-\frac{\pi}{2}$ to $\frac{\pi}{2}$ rad and is denoted as *region 1*. As a result of the optimization, the passive muscle forces do not play a role in *region 1* (cmp. K_p in Table 3.5). As a consequence, the passive curves are left out for the following considerations. A closer inspection of the resulting muscle setup shows that the optimization algorithm introduced two different types of muscles. One type can be denoted as *short muscles* (corresponding to M_1 and M_2), the other type as *long muscles* (corresponding to M_3 and M_4). Short muscles have an increased slope of the torque curves which results in a big change of stiffness for activation changes. Long muscles have a decreased slope. Therefore, an activation change has a stronger influence on the torque generation than on the joint stiffness. Figure 3.10(b) depicts the joint stiffness generated by the optimal

Table 3.5: Set of muscle parameters as a result of the optimization process.

x_j	Description	M_1	M_2	M_3	M_4
L_{off}	pre-stretch	$-\frac{\pi}{2}$	$-\frac{\pi}{2}$	$-\frac{\pi}{2}$	$-\frac{\pi}{2}$
w_{L0}	half width F-L curve	π	π	$2\,\pi$	$2\,\pi$
K_p	passive curve const.	0	0	0	0
F_{max}	max. isometric force	1	1	1	1

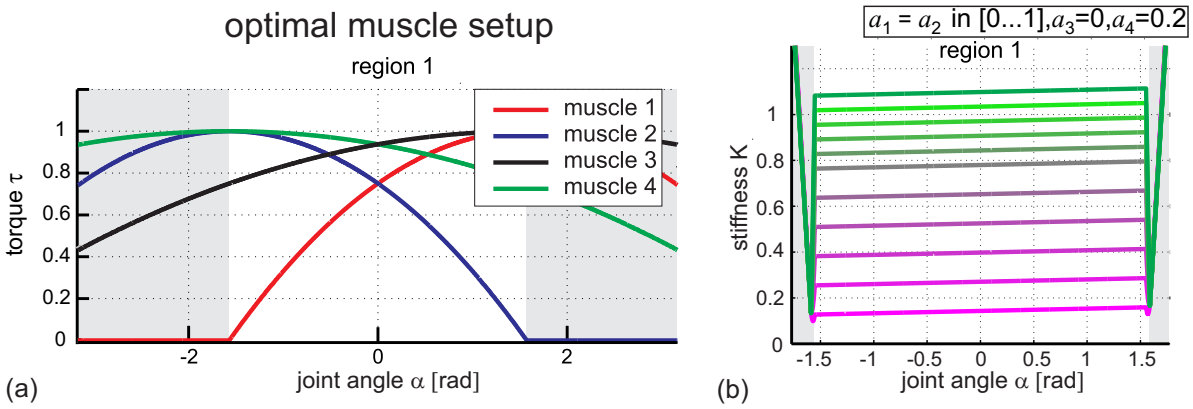

Fig. 3.10: (a) Result of the optimization process. Torque curves in a hinge joint generated by two antagonistic muscle pairs in the optimal configuration plotted against the joint angle. The curves are drawn in red (muscle 1), blue (muscle 2), black (muscle 3) and green (muscle 4). The width of the active parts of the force-length curves and their overlap in the joint angle space define different regions. The middle region – which is seen as the main working range of the joint – is denoted as *region 1*. (b) Joint stiffness plotted against the joint angle for the setup in (a) for co-activation of M_1 and M_2 ($a_1 = a_2$) and constant differential activation among M_3 and M_4. Maximum co-activation is depicted in dark green.

muscle setup when co-activation for M_1 and M_2 is applied and a constant activation offset is present among a_3 and a_4. In fig. 3.11, the maximum (a-b) and minimum (d-e) stiffness surfaces are plotted over joint angle and torque. Figures 3.11(c) and (f) show section views of the maximum and minimum surfaces for three selected net-torque values in *region 1*. For zero net-torque, the maximum stiffness reaches a value of almost 0.8 over the complete angular range. Figure 3.12 shows the optimal muscle activations resulting from the optimization process. These activations are responsible for generating the maximum and minimum stiffness surfaces shown in fig. 3.11 [subplots (a)-(d) for the maximum and subplots (e)-(h) for the minimum]. As expected, a_1 and a_2 are related to the generation of joint stiffness. Along the angular range of the joint they reach high values whenever high stiffness is generated and low values for low stiffness [cmp.(a,b) with (e,f)]. This seems to imply already some kind of co-activation. The activations a_3 and a_4 have a different behavior: When a low stiffness is generated [see (g,h)], these values can be high to generate high desired torques without strongly impairing the joint stiffness. This analysis shows that short muscles (M_1 and M_2) can be seen as *stiffness muscles* and long muscles (M_3 and M_4) as *torque muscles*.
The analysis of the condition (3.2) for the occurrence of the stiffness node in the *region 1* when adopting the optimal muscle setup, shows that in general a solution exists (i.e. a stiffness node occurs). However, an important result is that co-activation for M_1 and M_2, i.e. the constraint $a_1 = a_2$, leads to a node free *region 1* (i.e. the condition for the

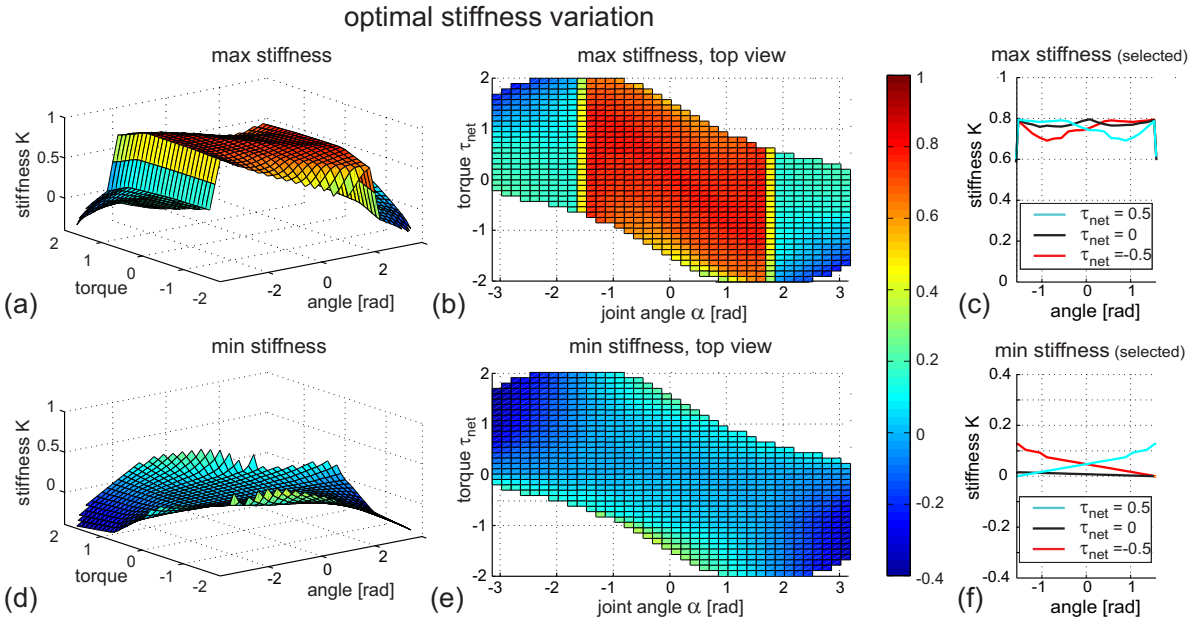

Fig. 3.11: Stiffness surfaces generated adopting the optimal muscle setup when the optimal activations resulting from the optimization process are applied. (a) Max stiffness plotted against joint angle and torque. (b) same as (a) in top view. (c) Section view of the maximum stiffness surface (a) for three selected torques (0.5, 0, −0.5) plotted against *region 1*. (d)-(f) same as (a)-(c) but for minimum stiffness.

occurrence of the stiffness node is never satisfied).

3.4 Torque/stiffness control approaches adopting the optimal muscle setup

As described in Section 3.3, for the optimal muscle setup, an algorithm tested all combinations of the four activations to get maximal stiffness variations across a desired angular range of motion and desired torque range. This approach delivered the activations able to provide the required maximal variation. However, the question remains, how a suitable control strategy might look like that delivers a torque and stiffness variability similar to the optimal one. In the following, the optimal muscle setup introduced in Section 3.3 is adopted and four different control strategies for the concurrent torque/stiffness control are described. In order to test and compare these control strategies, pairs of torque/stiffness values taken from the optimal stiffness surfaces shown in fig. 3.11(a,d) served as desired values. Figures 3.13(a1-d1) depict again the optimal stiffness surfaces and the corresponding section views. A dash-dotted rectangle indicates the main working range ($[-\frac{\pi}{2}, \frac{\pi}{2}]$ rad on the joint axis and +/-1 on the torque axis). For comparison with the optimal stiffness surfaces (min and max), for each of the four

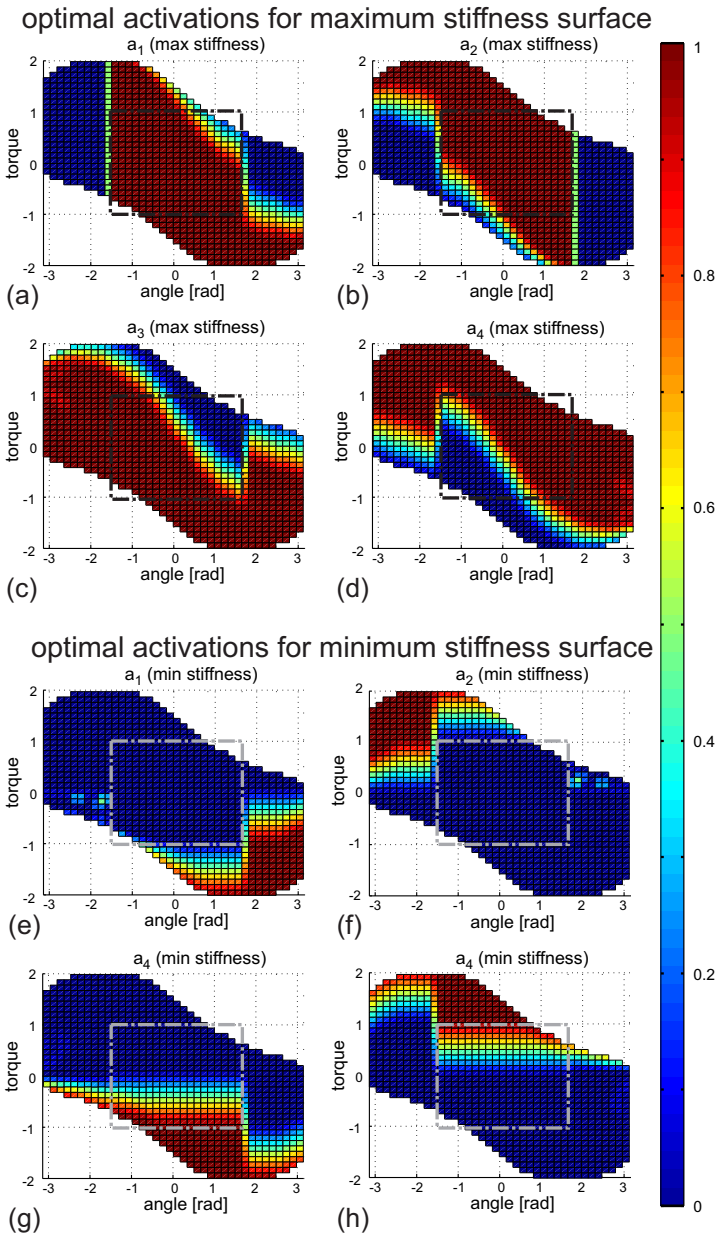

Fig. 3.12: Optimal activation values for the four muscles in the optimal setup for the maximum and minimum stiffness depicted in fig. 3.11. A dash-dotted rectangle indicates the main working range ($[-\frac{\pi}{2}, \frac{\pi}{2}]$ rad on the joint axis and +/-1 on the torque axis). Max activation ($a = 1$) is represented in dark red while min activation ($a = 0$) is shown in dark blue. (a) Activation of M_1 for max stiffness plotted against joint angle and torque.(b)-(d) same as (a) but for M_2, M_3 and M_4, respectively. (e) Activation of M_1 for min stiffness plotted against joint angle and torque. (f)-(h) same as (e) but for M_2, M_3 and M_4, respectively.

control strategies, a stiffness surface is also produced. As in the simulations before, a high inertia of the lever arm is assumed so that the joint angle is held constant.

3.4.1 Activation overflow strategy

The first control approach that is used for the optimal joint setup is based on a basic torque/stiffness control. The setup is the same as depicted in fig. 3.6 but without the stiffness node control. The controllers act on dedicated muscles. The torque controller generates the activations for the torque muscles (M_3 and M_4) and the stiffness controller the activations for the stiffness muscles (M_1 and M_2). All four activations are saturated at 0 and 1. One drawback of this basic torque/stiffness control is its missing ability to recruit the second muscle on one side if, for example, a higher torque and a lower stiffness is needed. This led to the second control approach which adds an *activation overflow strategy* to the first control strategy. In this case the activation overflow of one muscle is distributed to the other with the same torque direction when the activation reaches saturation level. The torque/stiffness control strategy including the activation overflow block (enclosed in a rectangular dashed line) is shown in fig. 3.14. The overflow mechanism is active if activation is above 1 and additional activation is required by a controller and also if activation is below 0 and a reduction is commanded. Both torque and stiffness controller in the simulations are of PI type. The parameters of both controllers were tuned in an iterative simulation process[5]. In a first sweep for all joint angles $[-\frac{\pi}{2}, \frac{\pi}{2}]$, torque $[-2, 2]$ and stiffness (taken from max and min surface of the optimal case) step inputs were used as desired values for the controllers. The iteration intervals for one sweep were partitioned in 40 steps for both angles and torques. The P-part was increased from a small initial value as long as no oscillations occurred within the test intervals. If oscillations occurred the P-part was decreased and the sweep was repeated until all simulations in the sweep were valid, i.e. no oscillations occurred for the complete sweep. In addition, the P-part was also decreased if the activation commands at the input of the saturation blocks were bigger than 1 which is the upper limit of valid muscle activations in this study. In a second phase, also the I-part was increased stepwise and torque and stiffness tests were carried out for valid joint angles unless the control signals saturated at 1. The controller parameters obtained as a result of the iterative process are listed in Table 3.6 (columns: *Torque/stiffness* and *Torque/stiffness plus act. overflow*).
Both cases, without and with overflow strategy were tested. Figures 3.13(a2-d2) show the stiffness surfaces obtained for the basic torque/stiffness control. Comparison of these surfaces with the optimal stiffness surfaces depicted in fig. 3.13(a1-d1) shows that this control strategy does not generate net-torques comparable to the optimal case. The maximum stiffness surface reaches maximum values of 0.68 as opposed to 0.8 in the

[5]The tuning approach is similar to the Ziegler-Nichols tuning method. An important difference is that, in this case, the parameters are selected in order to avoid any torque and stiffness oscillations at t=6.

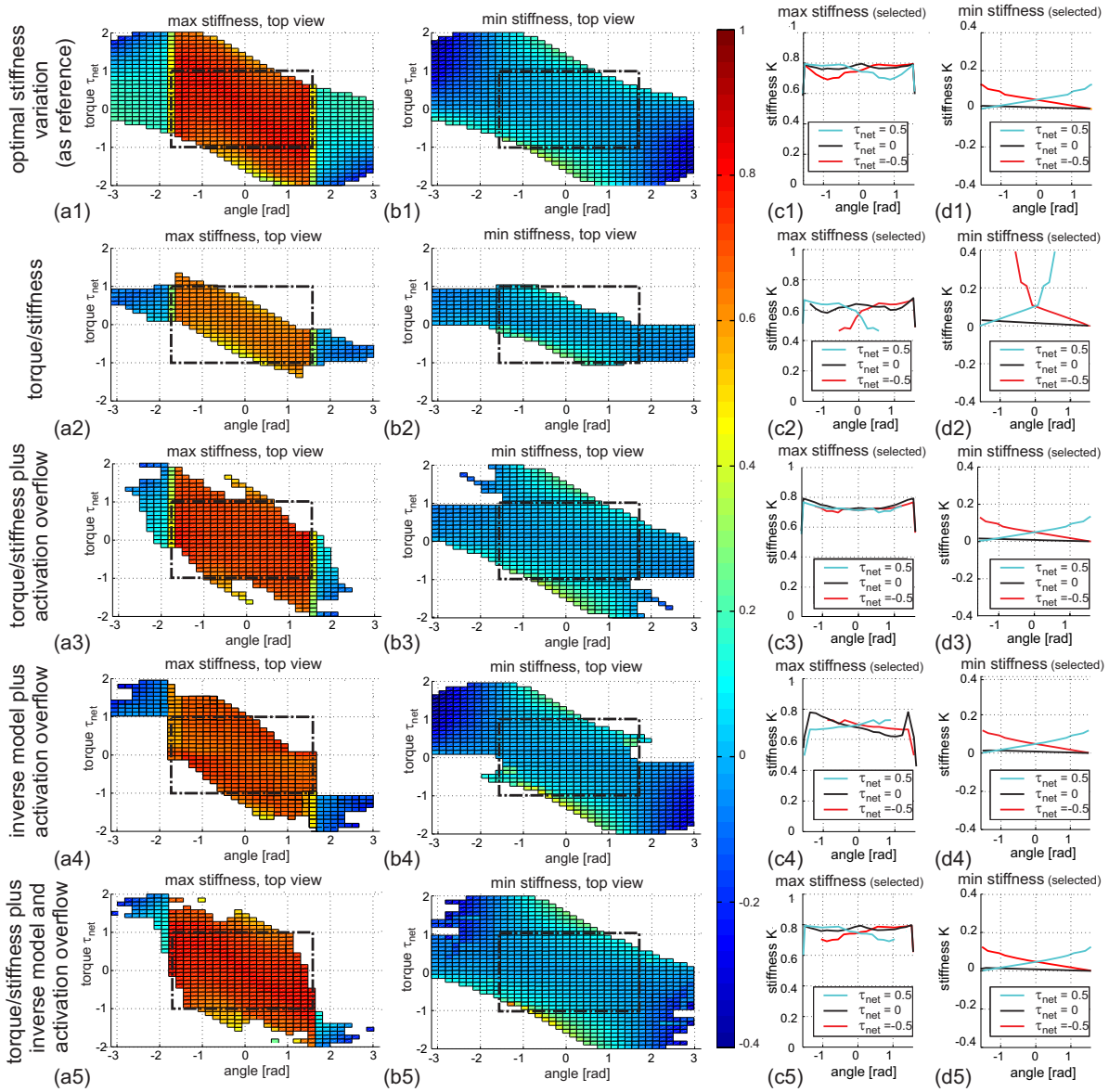

Fig. 3.13: (a1),(b1) Maximum and minimum stiffness surfaces generated for the optimal setup. (c1),(d1) Section views of the maximum and minimum stiffness surfaces for three selected torques ($\tau = 0.5$, 0.0 and -0.5) plotted against the angular range of the joint. (a2-a5) and (b2-b5) Maximum and minimum stiffnesses for four different control approaches. (c2-c5) and (d2-d5) Section views of maximum and minimum stiffnesses at torque values of 0.5, 0.0 and -0.5. Simulation parameters are given in Table 3.6.

optimal case. For easier comparison, dash-dotted rectangles in fig. 3.13(a1-a5) and (b1-b5) indicate the intended, basic workspace of the joint spanning *region 1* on the joint axis and values of ± 1 on the torque axis. Figures 3.13(a3-d3) depict the maximum and minimum stiffness surfaces obtained with the additional activation overflow strategy.

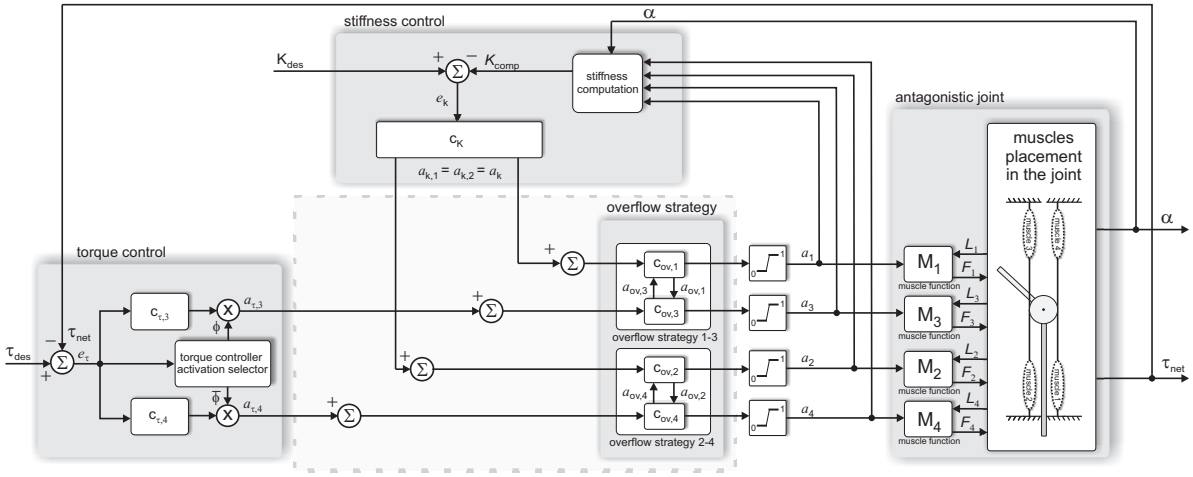

Fig. 3.14: Concurrent torque/stiffness control with activation overflow strategy for the optimal antagonistic muscle setup. The torque control activates either the agonistic or the antagonistic muscle in dependence of the desired torque. The stiffness control adopts a co-activation strategy. In the dashed line block the activation overflow strategy is depicted. When the conditions for the overflow strategy are verified the activations are re-distributed, saturated to 0 or 1 and then sent to the muscles.

This control strategy leads to a larger coverage of the basic workspace for the minimal and maximal stiffness surface. Figure 3.13(c3) shows high stiffness values for the whole *region 1*. Also the minimum stiffness which is reached [see fig. 3.13(d3)] is comparable to the optimal case.

3.4.2 Open-loop strategy with inverse model and activation overflow

On the way to find control strategies which deliver stiffnesses and torques comparable to those shown in fig. 3.13(a1-d1), it seems plausible to look for a system which compensates the effects of the nonlinear muscles. Feeding in open-loop a pair composed by the torque and stiffness values found for the optimal setup into the inverse formulation of the musculoskeletal setup would ideally deliver the optimal activations. In the following, the steps to get the inverse model of the musculoskeletal system are described[6].
The net-torque τ_{net} which is generated by the four muscles in the hinge joint is:

$$\tau_{\text{net}} \quad = \quad \mathrm{r}\,\mathrm{F}_{\max}\left(-a_1\,F_{\text{Laq},1} + a_2\,F_{\text{Laq},2} - a_3\,F_{\text{Laq},3} + a_4\,F_{\text{Laq},4}\right) \tag{3.4}$$

[6]The proposed inverse model strategy for torque and stiffness is an extension of the classical inverse dynamics approach (Bayo, 1987).

Table 3.6: Control parameters adopted in the simulation for the torque/stiffness control strategies of the antagonistic pulley joint setup.

		Control strategies		
Par.	Description	Torque/ stiffness	Torque/ stiffness plus act. overflow	Torque/stiffness plus inverse model and act. overflow
$c_{\mathrm{p},\tau}$	prop. gain torque contr.	0.5	0.5	0.5
$c_{\mathrm{i},\tau}$	integ. gain torque contr.	0.2	2	2
$c_{\mathrm{p,k}}$	prop. gain stiffness contr.	0.9	1	1
$c_{\mathrm{i,k}}$	integ. gain stiffness contr.	1	3	3

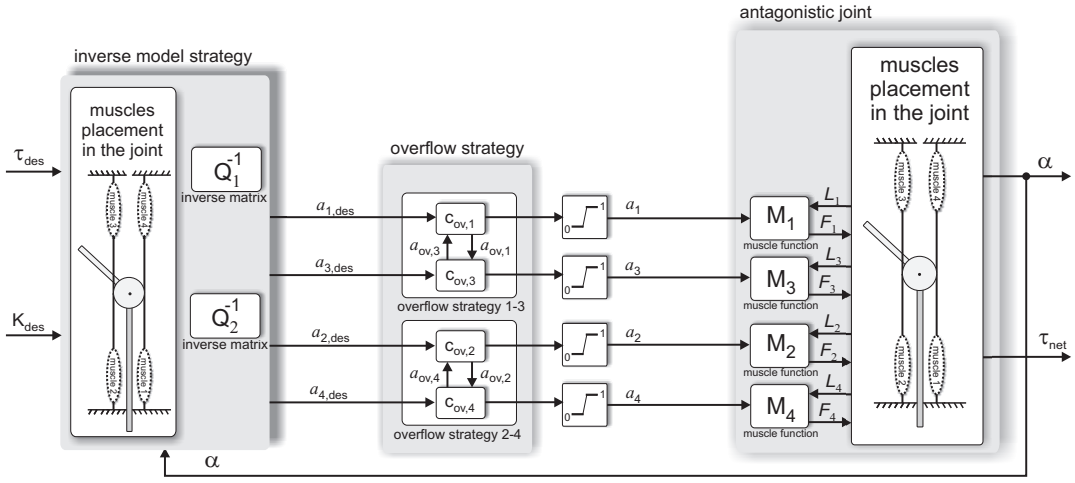

Fig. 3.15: Open-loop approach using the inverse model and activation overflow. The desired torque and stiffness are transformed in desired activations through an inverse matrix containing the system. The overflow strategy is then used to adjust the desired activations that are finally saturated.

with F_{Laq} corresponding to the quadratic version of the active force-length muscle function (2.3). The joint stiffness is:

$$
\begin{aligned}
K = \quad & -2\,\mathrm{r}^2\,\mathrm{F}_{\max}\cdot\left(\mathrm{a}_1\cdot\begin{cases}\frac{(\mathrm{L}_{\mathrm{off},1}+\mathrm{r}\,\alpha)}{\mathrm{w}^2_{\mathrm{L0},1}} & \text{if } \mathrm{w}_{\mathrm{L0},1}-|\mathrm{L}_{\mathrm{off},1}+\mathrm{r}\,\alpha|>0\\ 0 & \text{otherwise}\end{cases}\right.\\
& +a_2\cdot\begin{cases}\frac{(\mathrm{L}_{\mathrm{off},2}-\mathrm{r}\,\alpha)}{\mathrm{w}^2_{\mathrm{L0},2}} & \text{if } \mathrm{w}_{\mathrm{L0},2}-|\mathrm{L}_{\mathrm{off},2}-\mathrm{r}\,\alpha|>0\\ 0 & \text{otherwise}\end{cases}\\
& +a_3\cdot\begin{cases}\frac{(\mathrm{L}_{\mathrm{off},3}+\mathrm{r}\,\alpha)}{\mathrm{w}^2_{\mathrm{L0},3}} & \text{if } \mathrm{w}_{\mathrm{L0},3}-|\mathrm{L}_{\mathrm{off},3}+\mathrm{r}\,\alpha|>0\\ 0 & \text{otherwise}\end{cases}\\
& \left.+a_4\cdot\begin{cases}\frac{(\mathrm{L}_{\mathrm{off},4}-\mathrm{r}\,\alpha)}{\mathrm{w}^2_{\mathrm{L0},4}} & \text{if } \mathrm{w}_{\mathrm{L0},4}-|\mathrm{L}_{\mathrm{off},4}-\mathrm{r}\,\alpha|>0\\ 0 & \text{otherwise}\end{cases}\right) =\\
= \quad & -2\,\mathrm{r}^2\,\mathrm{F}_{\max}\left(a_1\,k_{\mathrm{a},1}+a_2\,k_{\mathrm{a},2}+a_3\;\;k_{\mathrm{a},3}+a_4\,k_{\mathrm{a},4}\right)\;. \qquad (3.5)
\end{aligned}
$$

Equations (3.4) and (3.5) represent the system that has to be inverted. By setting $\tau = \tau_{\mathrm{des}}$ and $K = \mathrm{K_{des}}$ it is not yet possible to obtain an explicit formulation of the four activations since this problem is not invertible. However, two constraints can be used to reduce the number of variables from four to two thus making the problem invertible. The first constraint introduces the co-activation idea for the two stiffness muscles[7]. The second constraint makes sure that only one of the two torque muscles is activated at a time depending on the desired torque. For the case:

$$\tau_{\mathrm{des}} \geq 0 \Rightarrow \begin{cases} a_{1,\mathrm{des}} = a_{2,\mathrm{des}} = \mathrm{a_{k,des}} \\ a_{3,\mathrm{des}} = 0 \\ a_{4,\mathrm{des}} = \mathrm{a}_{\tau,\mathrm{des}} \quad . \end{cases} \tag{3.6}$$

From (3.4) and (3.5) follows:

$$\mathrm{K_{des}} = -2\,\mathrm{r}^2\,\mathrm{F_{max}}\left[\mathrm{a_{k,des}}\,(k_{\mathrm{a},1} + k_{\mathrm{a},2}) + a_{\tau,\mathrm{des}}\,k_{\mathrm{a},4}\right] \tag{3.7}$$

$$\tau_{\mathrm{des}} = \mathrm{r\,F_{max}}\left[\mathrm{a_{k,des}}\,(\mathrm{F_{Laq,2}} - \mathrm{F_{Laq,1}}) + \mathrm{a}_{\tau,\mathrm{des}}\,\mathrm{F_{Laq,4}}\right] \tag{3.8}$$

That can be rearranged as:

$$Q_1 \cdot \begin{bmatrix} \mathrm{a_{k,des}} \\ \\ \mathrm{a}_{\tau,\mathrm{des}} \end{bmatrix} = \begin{bmatrix} \frac{\mathrm{K_{des}}}{-2\,\mathrm{r}^2\,\mathrm{F_{max}}} \\ \\ \frac{\tau_{\mathrm{des}}}{\mathrm{r\,F_{max}}} \end{bmatrix} \tag{3.9}$$

with the 2×2 matrix Q_1:

$$Q_1 = \begin{bmatrix} k_{\mathrm{a},1} + k_{\mathrm{a},2} & k_{\mathrm{a},4} \\ \\ F_{\mathrm{Laq},2} - F_{\mathrm{Laq},1} & F_{\mathrm{Laq},4} \quad . \end{bmatrix} \tag{3.10}$$

The desired activations can be derived by inverting the matrix Q_1

$$\begin{bmatrix} \mathrm{a_{k,des}} \\ \\ \mathrm{a}_{\tau,\mathrm{des}} \end{bmatrix} = Q_1^{-1} \cdot \begin{bmatrix} \frac{\mathrm{K_{des}}}{-2\,\mathrm{r}^2\,\mathrm{F_{max}}} \\ \\ \frac{\tau_{\mathrm{des}}}{\mathrm{r\,F_{max}}} \quad . \end{bmatrix} \tag{3.11}$$

It can be shown that Q_1 has full rank in the joint angle range $(-\frac{3}{2}\pi, \frac{3}{2}\pi)$ rad.
When $\tau_{\mathrm{des}} < 0$, a_3 is used by the controller and a_4 is set to 0. By using the same approach as before, the following result is obtained:

$$\begin{bmatrix} \mathrm{a_{k,des}} \\ \\ \mathrm{a}_{\tau,\mathrm{des}} \end{bmatrix} = Q_2^{-1} \cdot \begin{bmatrix} \frac{\mathrm{K_{des}}}{-2\,\mathrm{r}^2\,\mathrm{F_{max}}} \\ \\ \frac{\tau_{\mathrm{des}}}{\mathrm{r\,F_{max}}} \end{bmatrix} \tag{3.12}$$

with

$$Q_2 = \begin{bmatrix} k_{\mathrm{a},1} + k_{\mathrm{a}2} & k_{\mathrm{a},3} \\ \\ F_{\mathrm{Laq},2} - F_{\mathrm{Laq},1} & -F_{\mathrm{Laq},3} \quad . \end{bmatrix} \tag{3.13}$$

[7] Considering the way the CNS activates antagonistic muscles to vary the stiffness at the joint.

It can be shown that Q_2 has full rank in the joint angle range $(-\frac{3}{2}\pi, \frac{3}{2}\pi)$ rad.
It cannot be guaranteed that the activations that are generated by the inverse model approach lie in the interval $[0, 1]$. To handle those activations above 1 and below 0, the activation overflow strategy is also employed. The complete control strategy is shown in fig. 3.15. Figures 3.13(a4-d4) depict the maximum and minimum stiffness surfaces with the inverse model control strategy. It can be seen that this strategy delivers results which do not completely reach the level of the optimal approach.

3.4.3 Closed-loop control with inverse model and activation overflow

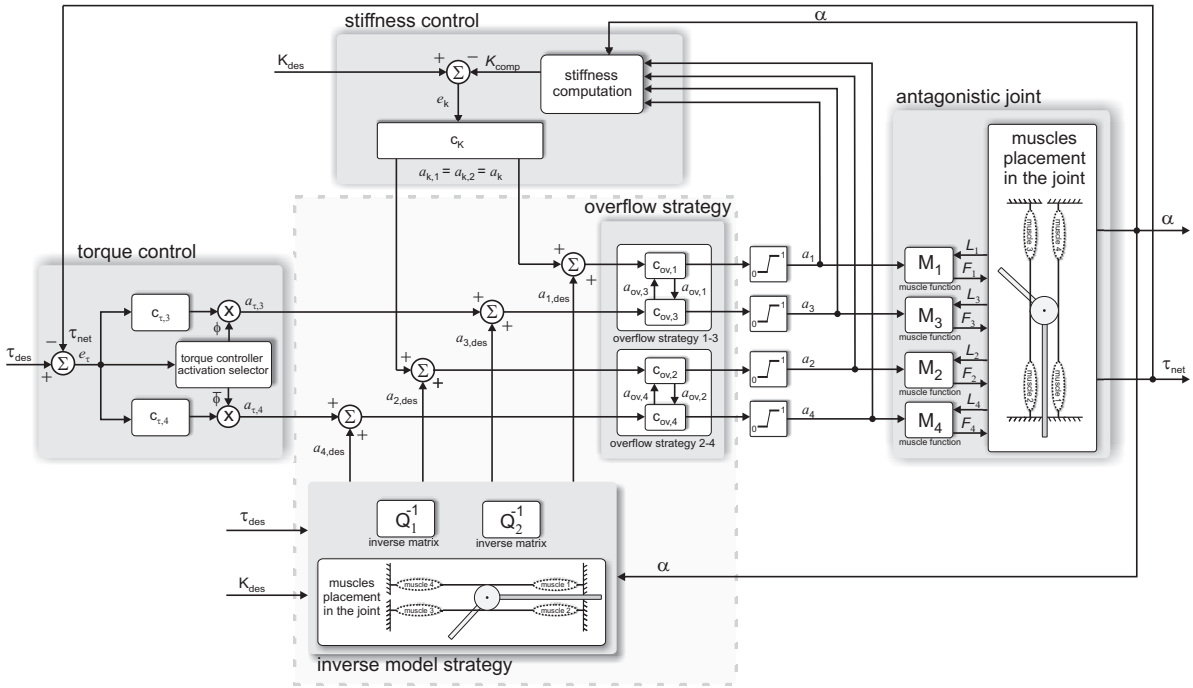

Fig. 3.16: Torque/stiffness closed-loop control combined with the inverse model strategy and the activation overflow. Apart from the desired activations coming from the inverse model strategy, the generated torque and stiffness are fed back to close the control loop. The control signals from the controllers are summed up to the values coming from the inverse model strategy and then re-distributed through the overflow strategy.

The inverse model strategy delivers feed-forward values based on the model and the desired signals. To improve its performance, closed loops for torque and stiffness would be desirable. For this purpose, the torque and stiffness controllers as introduced earlier in this study are combined with the inverse model strategy. The overall setup is shown in fig. 3.16. Figures 3.13(a5-d5) depict the maximum and minimum stiffness surfaces

achieved with this control strategy. The results obtained with this last scheme are close to those of the optimal case.

3.4.4 Response time comparison

Among the different control schemes proposed in this section, the torque/stiffness plus activation overflow and the torque/stiffness plus inverse model and activation overflow are the ones that perform best compared to the optimal setup (see fig. 3.13). However, the latter strategy with the inverse model is computationally more expensive. The question arises whether this effort is rewarded with a shorter time for reaching the desired torque and stiffness.

Figure 3.17 shows a comparison of the stiffness and torque response over time for the two control strategies under analysis: torque/stiffness plus activation overflow (a-c) and torque/stiffness control strategy with inverse model and activation overflow (d-f). In the simulation the desired values are $\tau_{\text{des}} = 0.5$ and $K_{\text{des}} = 0.8$ while the lever is kept at $\alpha = 0$. The torque responses are identical [cmp. fig. 3.17(a) and (d)]. The stiffness response of the strategy with the inverse model is faster because of the additional feed-forward branch [cmp. fig. 3.17(b) and (e)]. In both cases the desired stiffness cannot be reached despite the maximum activation sent to the stiffness muscles and the overflow strategy [cmp. fig. 3.17(c) and (f)].

Further simulations for different fixed joint positions ($\alpha = -\pi/4$ and $\alpha = \pi/4$) as well as for different desired values ($\tau_{\text{des}} = 0$ and $K_{\text{des}} = 0.8$) were analyzed. The resulting response time behavior is similar to that shown here thus confirming that the employment of the inverse model repays with a faster stiffness response time.

3.5 Summary

With the objective to control the torque and the stiffness at the joint, in this chapter a concurrent torque/stiffness control was introduced and tested in a numerical simulation in Matlab/Simulink. As a result, it was shown that concurrent control of torque and stiffness works if no stiffness node is in the vicinity of the operation angle but that the controller is bound to fail if a node is close by. To address this problem, an additional pair of muscles was added to the joint. The use of two pairs of antagonistic muscles for driving the hinge joint adds additional degrees of freedom which can be used in the control strategy for shifting the node away when the angular position of the joint approaches the node. This new control strategy was called *stiffness node control* and was tested in a numerical simulation using Matlab/Simulink. The introduction of this new controller enabled the joint to reach the desired torque and stiffness values even if a node was close by (Section 3.2). Even without the occurrence of a stiffness node, the ability to control the stiffness across the whole range of the joint angular range of motion could be limited due to the joint and muscle configuration. Therefore, in Section 3.3 an

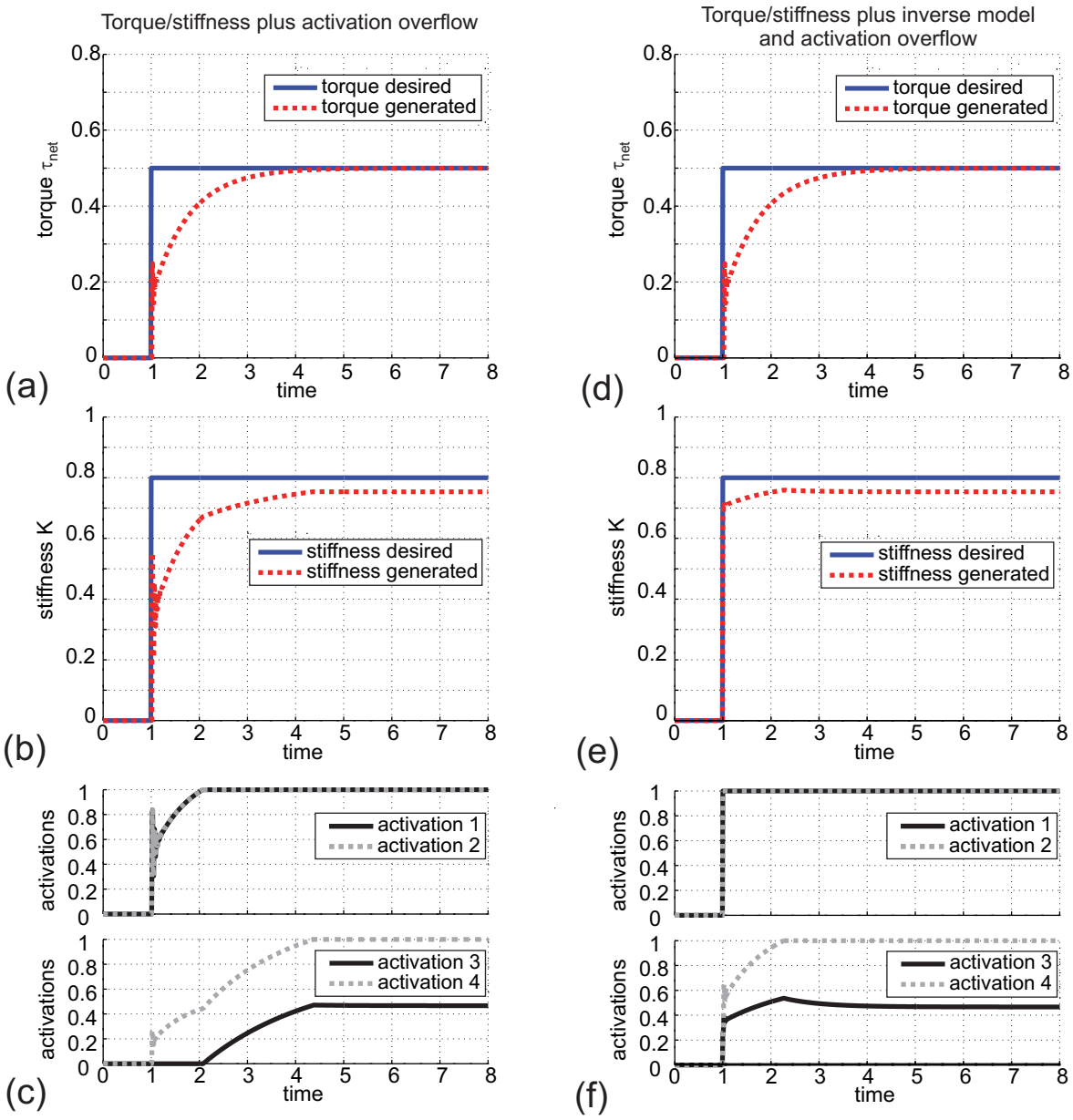

Fig. 3.17: Response time comparison for the two control strategies that best perform: torque/stiffness plus activation overflow [(a)-(c)] and torque/stiffness plus inverse model and activation overflow [(d)-(f)]. The simulation results are shown for $\alpha = 0$. The feed-forward strategy based on the inverse model of the joint in combination with activation overflow has the ability to reach the desired joint stiffness faster than other strategies.

optimization approach was performed to identify a muscle configuration which resulted in the maximal stiffness variation across the angular workspace of the joint. This optimization process delivered activation patterns for all four muscles which resulted in an optimal stiffness variation. However, an appropriate control setup to generate such

a stiffness variation was still unknown. For that reason, based on the optimal muscle parameters, in Section 3.4 several control approaches for the simultaneous control of torque and stiffness were introduced. Torque and stiffness results were compared with the optimal example and it was shown that a concurrent torque/stiffness controller with dedicated muscle pairs for the separate control of torque and stiffness with an additional activation overflow strategy was able to produce maximum and minimum stiffness surfaces comparable to the optimal case. Since the complete joint and muscle models were known, an inverse model approach was tested in order to produce feed-forward control values. This strategy in combination with activation overflow had the ability to control the joint stiffness faster than the other strategies. All strategies were implemented in a dynamics simulation of a hinge joint based on Matlab/Simulink.

Chapter 4

Bio-inspired control laws adopting antagonistic muscle actuation in a simplified elbow joint setup

In Chapter 2 it was shown that a simplified human elbow joint can be modeled with a pulley hinge joint and two antagonistic muscles. The antagonistic musculoskeletal setup was introduced in Section 2.1.3. Adopting biological data, the mechanical impedance properties for such a setup were analyzed (Section 2.2) and it was shown that co-activation for antagonistic muscles is the key to vary stiffness in the angular range of the joint. In Chapter 3 several control schemes were discussed which use co-activation and reciprocal activation for the concurrent control of torque and stiffness. Additionally, an inverse model together with an activation overflow strategy was used to investigate the maximum range of stiffness and torque variation (Section 3.4.3). Although inverse model as well as overflow strategy seems to be plausible approaches to maximize stiffness and torque variation, there is no direct biological justification that the CNS uses such approaches in the control of muscle activation. Therefore, the control schemes of Chapter 3 represent optimal but yet theoretical strategies for stiffness and torque variation.

As in Chapter 3 also this chapter uses a biomechanical setup without stiffness nodes in the nominal working region. However, in the present chapter, only the basic and biologically justified aspects of Chapter 3 (co-activation and reciprocal activation) are used as a starting point to concurrently control stiffness and position (instead of torque). The goal of this chapter is to extend the biologically plausible aspects of Chapter 3 by adding models of the muscle spindles, Golgi tendon organs (GTOs), α-motor neurons (α-MNs) and Renshaw cells, which are known to play a major role in the immediate control of a vertebrate muscle. The control scheme and the biological details are explained in Section 4.2. As preparation for the controller design, in Section 4.1, the stability aspect of muscle-driven joints is briefly revisited. Based on the results of this analysis, an adaptive mechanism for the control of stability during interactions is integrated in the stiffness controller. This chapter concludes with simulation results which demonstrate the ability of the controller to simultaneously regulate position and adapt joint compliance to different external perturbations (Section 4.3).

The scientific results of this chapter were published in the journal *Applied Bionics and*

Biomechanics (Annunziata and Schneider, 2012). The manuscript includes Axel Schneider as co-author.

4.1 Stability analysis of an antagonistically actuated hinge joint setup with a pulley

It was shown that muscles alone mounted in an antagonistic setup provide an intrinsic stability effect at joint level (Giesl et al., 2004; Richardson et al., 2005). In fact, spring-like and viscous-like muscle properties produce zero-delay resistive forces against external perturbations (Raphael et al., 2010). Only for strong perturbations, additional control mechanisms might be required to damp the oscillations and reduce the settling time (Chou and Hannaford, 1997). In particular, as it was pointed out by Giesl and Wagner (2007), although energetically expensive, high co-activations have a stabilizing effect on the joint. The stiffness control scheme presented in this thesis also integrates this aspect and, with the objective to show its effectiveness on the antagonistic joint described above, the stability properties are analyzed when the system is subject to perturbations. First of all, the mathematical condition for finding the equilibrium position is discussed. Then, different cases adopting constant activation levels to the muscles are studied. Simulation results are shown for two situations: *low* and *high* muscle activations.

Consider the nonlinear system:

$$\dot{\mathbf{x}} = \mathbf{f}(\mathbf{x}, \mathbf{t}) \quad , \quad \mathbf{x}(\mathbf{t_0}) = \mathbf{x_0} \in \Re^n \tag{4.1}$$

where $\mathbf{x}$ is the state of the system, $\mathbf{x_0}$ is its initial condition and $t \geq 0$. $\mathbf{x}^*$ is said to be an equilibrium point of (4.1) if $\mathbf{f}(\mathbf{x}^*, \mathbf{t}) \equiv 0$ for all $t \geq 0$.
For the system composed by two antagonistic muscles in a pulley hinge joint of equation (2.11), the unperturbed equilibrium points can be obtained by studying its solutions which correspond to the study of the following system:

$$\begin{cases} \omega & = 0 \\ \tau_{\text{net}}(a_1, a_2, \alpha^*, \omega) - \tau_{\text{G}}(\alpha^*) - \tau_{\text{L}} & = 0 \end{cases} \tag{4.2}$$

where α^* is the equilibrium position. It is important to notice that, once the activation a_1 is selected and the load torque τ_{L} is defined, the system (4.2) can be solved with respect to the only unknown a_2 with the constraint

$$0 \leq a_2 \leq 1 \quad .$$

For the antagonistic joint adopted, let us assume as unperturbed equilibrium position $\alpha^* = -0.4\,\text{rad}$. Two simulations with increasing values of a_1 ($a_1 = 0$, $a_1 = 1$) are performed while a mass (M_L) is attached to the lever to increase the inertia and an external load force (F_L) is applied at its end (see fig. 4.1). Table 4.1 reports the activations

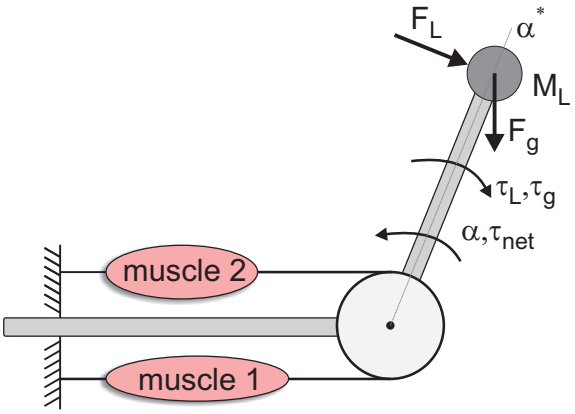

Fig. 4.1: Model of the antagonistic joint setup with the mass attached at the extremity of the lever arm.

Table 4.1: Simulation parameters for the stability analysis of the antagonistic pulley joint setup.

Parameter	Description	Value	Unit
α_0	initial position	0.5	rad
ω_0	initial velocity	5	rad/s
α^*	equilibrium position	-0.4	rad
M_L	load mass	3	kg
F_L	load force	-15	N
τ_L	impulsive load torque	20	Nm
Activation	**Description**	**Low act.**	**High act.**
a_1	activation 1	0	1
a_2	activation 2	0.21	0.98

and the simulation parameters used in the analysis. Joint parameters are taken from Table 2.2 and muscle parameters from Table 2.3. It can be shown through linearization around the equilibrium point that α^* corresponds to a stable equilibrium in both analyzed cases. Each simulation runs for 5 seconds and starts from the initial condition $(\alpha_0,\ \omega_0) \equiv (0.5,\ 5)$. Furthermore, at t = 2 s the joint is subjected to an impulsive torque τ_L (amplitude 20 Nm and duration 20 ms) which simulates a disturbance. By solving the system (4.2) for each value a_1, a corresponding value for a_2 is obtained such that the equilibrium position is kept at α^*. Figure 4.2 depicts the simulation results in the following two cases: *low activations* (a) and *high activations* (b). The plots at the top of the figure show the trajectory of the lever over time and the corresponding stiffness computed using equation (2.14). The plots at the bottom of fig. 4.2 show the vector field together with the trajectory of the lever from the starting value $(\alpha_0,\ \omega_0)$ to

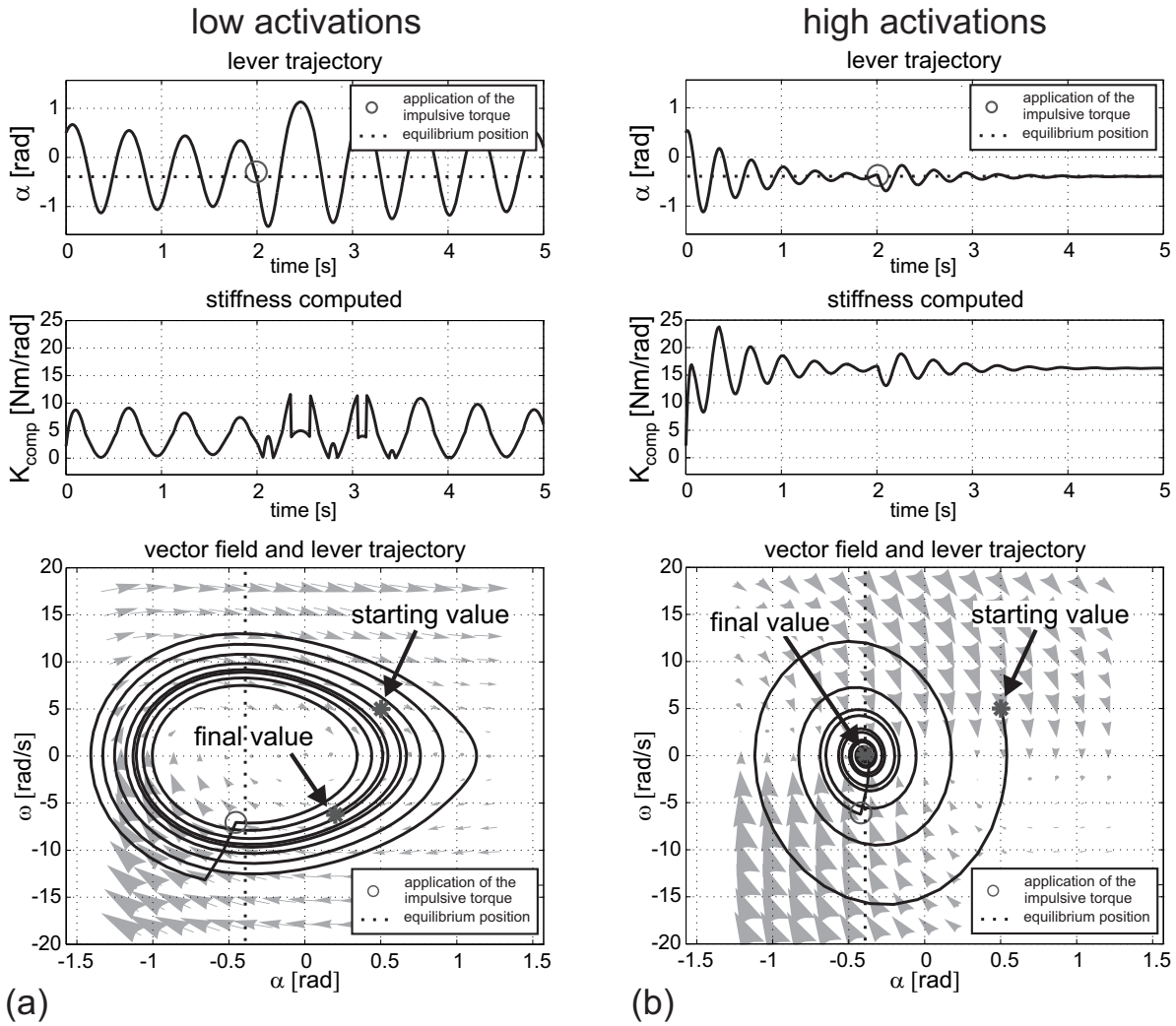

Fig. 4.2: Stability analysis of the musculoskeletal antagonistic hinge joint loaded by external forces for two different activation levels. In the top of the figure, the lever trajectory and the stiffness computed are plotted against time. In the bottom the vector field and the lever trajectory are depicted. (a) depicts the simulation results in the case of muscles with low activations. The equilibrium position is stable but oscillations are high. At t = 2 s an impulsive torque is applied to the lever which increases limb oscillations. (b) same as (a) but for higher activations. Oscillations are more damped and the impulsive torque has a less perturbing effect on the limb. High joint stiffness provides a stabilizing effect at joint level.

the final value reached after 5 seconds of simulation. For *low activations* a low stiffness is generated and the lever, although stable, is only slightly damped and oscillates around the asymptotic equilibrium position [see fig. 4.2(a)]. At t = 2 s the impulsive torque is applied and the system keeps a stable behavior although oscillations around the equilibrium position become higher. In the case of *high activations*, the stiffness is higher

and oscillations are more damped around the equilibrium with respect to the former case [see fig. 4.2(b)]. The system reaches the equilibrium position after 2 seconds. The application of the impulsive torque at t = 2 s has an almost insignificant effect on the lever as the higher stiffness produces a stabilizing effect on the joint which, in turn, is stronger against external disturbances.

4.2 Bio-inspired control strategy for stable compliant joints

In this section, a bio-inspired concurrent control of position and stiffness for the antagonistically actuated hinge joint with two muscles, as described in Section 2.1.3, is designed. With respect to the control schemes presented in Chapter 3, here only the biologically justified aspects of co-activation and reciprocal activation are adopted. This approach provides a basic bio-inspired controller similar to the concurrent torque/stiffness control presented in Section 3.2. This basic controller is then completed with physiological properties and biological models of muscle spindles, GTOs, α-MNs and Renshaw cells, which play a major role in the control of antagonistic vertebrate muscles (Kandel et al., 2000). The objective is to integrate, among others, mechanisms to account for the stability properties shown in Section 4.1 thus providing the mechanical system with the ability to execute tasks also with perturbing loads. In order to verify the performance of the bio-inspired control scheme, simulations are performed in Matlab/Simulink.
The parameters for *muscle* 1 (M_1) and *muscle* 2 (M_2) are listed in Table 2.3 and are based on measurements of the elbow muscles performed by Murray et al. (2000). This setup does not present stiffness nodes in the main working region (see fig. 2.7 for the case of co-activation).

4.2.1 Basic concurrent position/stiffness control

The basic concurrent control of position and stiffness can be divided in two separate mechanisms. A position controller, which is responsible for generating the necessary torque in order to reach the desired position, and a stiffness controller which has the task to reach the desired stiffness and adequately compensate changes in stiffness due to the position controller action. The position controller relies on reciprocal activation of antagonistic muscles. The stiffness controller integrates a stiffness-computation block which implements equation (2.14) and adopts a co-activation strategy. Figure 4.3 depicts the basic *position/stiffness control* for the *antagonistic joint* setup. α_{des} is the desired joint position and K_{des} is the desired stiffness.

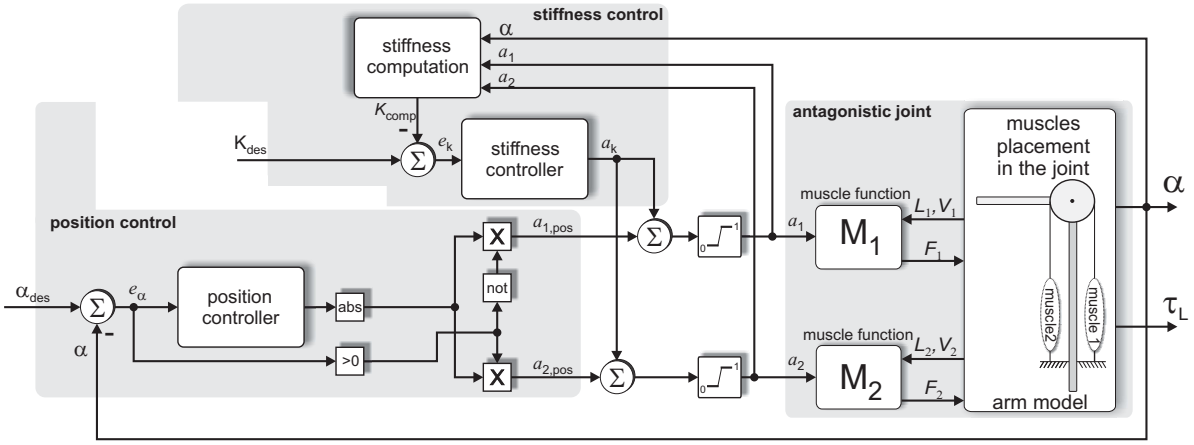

Fig. 4.3: Schematic view of the basic concurrent *position/stiffness control* acting on the *antagonistic joint*. On the right side, two muscles (M_1 and M_2) are placed in an antagonistic joint setup (arm model). Forces F_1 and F_2 are generated based on the actual activation levels (a_1 and a_2) and muscle lengths/velocities (L_1, V_1, L_2, V_2). The position controller on the left side activates either the agonistic or the antagonistic muscle in dependence of the joint position error e_α. The stiffness controller at the top generates the same activation (a_k) for both muscles (co-activation).

4.2.2 Biological feedback system for the control of a single muscle

In order to add to the basic concurrent *position/stiffness* controller further biological mechanisms for the regulation of the joint movement, in this section, the main aspects of a biological feedback system for the control of an antagonistic joint setup are described. It has to be emphasized that this section has no pretensions of being able to present an exhaustive analysis of the biological details related to the movements of vertebrates. Furthermore, to simplify the modeling stage, the total effect of the motor units and receptors for each muscle is embodied in only one unit.

In Section 2.1 the muscle was modeled only as a force generator (Hill-type muscle model). In this section, the analysis is focused not only on the force generation capability of a muscle but also on the embedded sensory cells involved in muscle regulation.
Figure 4.4 shows a simplified depiction of the biological regulation system for a single muscle. The components involved in the sensory transduction are the *muscle spindles*. These are specialized muscle receptors that lie in parallel with the muscle fibers. The *muscle spindle* is depicted as a block with a red frame in fig. 4.4. Each *muscle spindle* is innervated by a small-diameter motor neuron, the γ-motor neuron (MN) to distinguish it from the large-diameter α-MN (depicted with a blue frame in fig. 4.4) that innervates the muscle fibers. The *muscle spindle* consists of two parts. A muscular part, whose state of contraction is controlled by the γ-MN, and a central, elastic part,

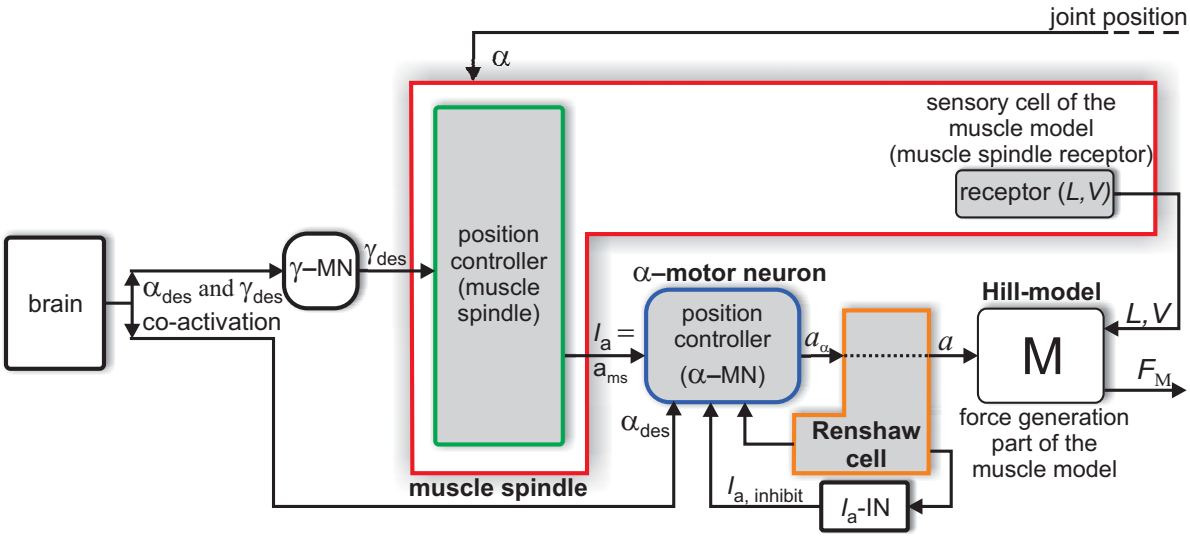

Fig. 4.4: Simplified illustration of a biological regulation strategy for the activation of a muscle in an antagonistic joint setup. The force generation aspect of the muscle is modeled adopting the Hill-type model (on the right). The *muscle spindle* is modeled as position controller and sensor. The command γ_{des}, from the γ-motor neuron, is responsible for producing a shortening in the muscle spindle which corresponds to the desired trajectory at joint level. The α-motor neuron, like the *muscle spindle*, receives an input from the brain as a feed-forward position signal α_{des} (α_{des} and γ_{des} co-activation). The α-motor neuron, together with the *muscle spindle* and *Renshaw cell*, forms a feedback system for the joint position and stiffness. The *Renshaw cell* stabilizes the α-motor neuron's firing rate a_α and produces an inhibitory signal for the I_{a}-IN, to regulate the strength of reciprocal inhibition thus enabling co-activation of antagonistic muscles.

which contains the muscle spindle receptor. The main function of the muscle spindle receptor is to signal changes in the length of the muscle. Since changes in the length of muscles are closely associated with changes in the angles of the joints that the muscles cross, muscle spindles can be used by the CNS to sense relative positions of the limb. Furthermore, the *muscle spindle* reacts to any muscle stretch by increasing the firing rate I_{a} to the α-motor neuron (stretch-reflex loop). The bigger the length-change, the higher the firing rate. The faster the rate of change, the higher the firing rate. When an external load is applied to the joint, the muscle is stretched and, as a consequence, the *muscle spindle* increases the firing rate to the α-MN thus counteracting the load (position controller, depicted as a block with a green frame in fig. 4.4).
The *muscle spindle* does not directly cause the muscle to contract [its firing rate is too small to produce a muscle contraction (Hoult and Cole, 2008)]. Instead, it causes activation of the α-MN which in turn is responsible for direct muscle activation a_α. During voluntary control of muscle length, the α-MN and the γ-MN receive from the brain a reference value corresponding to the expected shortening of the muscle during the move-

ment. Therefore, the fibers that activate the α and γ-MNs undergo parallel stimulation (α_{des} and γ_{des} co-activation) (Kandel et al., 2000; Shadmehr and Wise, 2005) where α_{des} represents a feed-forward position signal from the brain.
In an antagonistic setup, depending on the desired direction of motion, the CNS activates either the agonistic or the antagonistic muscle (reciprocal activation). The activated muscle shortens while the other relaxes. This mechanism is controlled through modulation of *reciprocal inhibition* by the *Renshaw cell*. The *Renshaw cell*, depicted as a block with an orange frame in fig. 4.4, is an inhibitory interneuron (IN) that plays two important roles. Firstly, it stabilizes the α-MN's firing rate a_α thus acting as limiter (Latash, 2008). Secondly, it regulates the strength of reciprocal inhibition to antagonistic motor neurons thus enabling co-contraction (recurrent inhibition) (Graham and Redman, 1993). In this case the *Renshaw cell* inhibits the I_{a}-IN, which decreases its activity and as a consequence the co-activation of antagonistic muscles is obtained.
The system composed by *muscle spindle*, α-MN and *Renshaw cell* can be described as a feedback system for the joint position with feed-forward connection of reference input. Additional sensors are the *Golgi tendon organs* (not shown). They are mechanoreceptors located between muscle and tendon and measure the tension occurring there.

4.2.3 Bio-inspired position controller

In this section, a novel position control strategy that uses antagonistic muscles in combination with bio-inspired control concepts such as reciprocal activation is presented. This strategy integrates also the model of physiological properties and motor neurons (MNs) as described above. The bio-inspired position controller of a single muscle (*muscle 2*) is depicted in fig. 4.5 in form of a block diagram.
Figure 4.5 adopts the same color code of fig. 4.4, thus pointing out the modeling of biological mechanisms in a technical framework. In the following subsections, the description of each block is provided.

Block diagram of the muscle spindle

The *muscle spindle* is modeled in this thesis as transducer, comparator and controller for the angular position. The receptor part of the *muscle spindle* measures the actual muscle length (L) and its rate of change (V). The *muscle spindle* is also a transducer as it transmits these measures to the CNS. Furthermore, it is a controller of the muscle length thus working as position controller. The firing rate depends on the muscle-length and also on the change of the muscle-length. Therefore, the muscle spindle and the reflex connections form a PD feedback control system for the joint position (stretch-reflex loop). In order to implement the spring-like muscle behavior when a load is

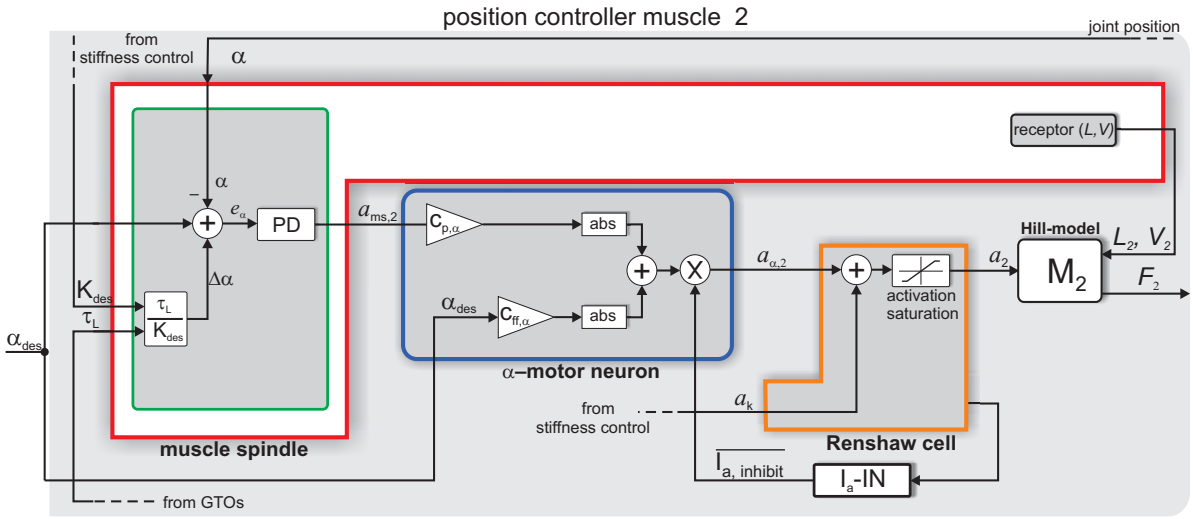

Fig. 4.5: Schematic depiction of the bio-inspired position controller for muscle 2. A reference value is sent to both *muscle spindle* (through the γ-MN, not shown) and α-*motor neuron* (α_{des} and γ_{des} co-activation). A position offset ($\Delta\alpha$) is generated when a load (τ_{L}) is applied to the output and added to the set point. The *muscle spindle* (red frame) works as transducer, comparator and controller for the joint position. The control signal, that is generated in the *muscle spindle*, is amplified by the α-*motor neuron* (blue frame) and added to a feed-forward position signal. The resulting activation $a_{\alpha,2}$ is then summed to the activation coming from the stiffness controller (a_{k}), saturated to 1 (*Renshaw cell*, orange frame) and sent to the muscle. The signal $I_{\text{a,inhibit}}$ is generated by the I_a inhibitory interneuron (I_a-IN block) that, together with the *Renshaw cell* activity, implements the reciprocal inhibition.

applied to the system (McIntyre and Bizzi, 1993), a position offset ($\Delta\alpha$), defined as

$$\Delta\alpha = \frac{\tau_L}{\text{K}_{\text{des}}} \tag{4.3}$$

is added to the position set point α_{des} (where τ_L is the load torque and K_{des} is the desired stiffness). Those mechanisms are modeled in fig. 4.5 as a feedback control loop with a proportional-derivative (PD) controller (blue frame).
When the joint position error e_α is defined as the difference between compliant desired position ($\alpha_{\text{des}} + \Delta\alpha$) and actual position ($\alpha$), i.e.

$$e_\alpha = \alpha_{\text{des}} + \Delta\alpha - \alpha, \tag{4.4}$$

the firing rate of the *muscle spindle* is

$$\begin{aligned} a_{\text{ms},1} &= \text{c}_{\text{p},1} \cdot \text{e}_\alpha(\text{t}) + \text{c}_{\text{d},1} \cdot \tfrac{\text{d}}{\text{dt}}\text{e}_\alpha(\text{t}) \\ a_{\text{ms},2} &= \text{c}_{\text{p},2} \cdot \text{e}_\alpha(\text{t}) + \text{c}_{\text{d},2} \cdot \tfrac{\text{d}}{\text{dt}}\text{e}_\alpha(\text{t}) \end{aligned} \tag{4.5}$$

with c_p and c_d being the proportional and derivative gains of the position controller (PD-controller in the muscle spindle box, the index refers to the muscle).

Block diagram of the α-motor neuron

The *muscle spindle* does not directly cause the muscle to contract. The α-MN is responsible for direct muscle activation. The activation a_{ms} from the *muscle spindle* is amplified in the block $c_{p,\alpha}$ of the α-MN. An additional input of the α-MN is the feed-forward position signal α_{des}. This signal is multiplied by a scaling factor (c_{ff} block) and added to the activation due to the stretch-reflex loop.

Based on the mechanisms described above, the firing rate of each α-MN is

$$\begin{aligned} a_{\alpha,1} &= |c_{ff,\alpha}\ \alpha_{des}| + |c_{p,\alpha}\ a_{ms,1}|\ \ I_{a,inhibit} \\ a_{\alpha,2} &= |c_{ff,\alpha}\ \alpha_{des}| + |c_{p,\alpha}\ a_{ms,2}|\ \ \overline{I_{a,inhibit}} \end{aligned} \tag{4.6}$$

for which either M_1 or M_2 is activated to generate a torque in the desired angular direction and with $c_{ff,\alpha}$ being the feed-forward scaling gain and $c_{p,\alpha}$ being the proportional (amplification) gain of the position controller. The variable $I_{a,inhibit}$ indicates the I_a inhibitory signal and is defined in the next subsection.

Block diagram of I_a-interneuron and Golgi tendon organ

In dependence of the joint position error (e_α) the *reciprocal inhibition* mechanism, activates through the I_a-interneuron (I_a-IN), either the position controller of M_1 or the position controller of M_2. The variable $I_{a,inhibit}$ is defined as

$$I_{a,inhibit} = \begin{cases} 1 & e_\alpha < 0 \\ 0 & e_\alpha \geq 0 \end{cases} .$$

The force feedback is realized with the measure provided by the *Golgi tendon organ* (not shown). In the block diagram of fig. 4.5, all GTOs are assumed to provide the total force at joint level as a feedback signal τ_L to the CNS (Mileusnic and Loeb, 2006).

Block diagram of the Renshaw cell

The *Renshaw cell* is responsible, firstly, for limiting the total activation to the muscle (*activation saturation* block). Therefore, it is depicted in fig. 4.5 with an *activation saturation* block. Secondly, it regulates the strength of reciprocal inhibition to antagonistic motor neurons thus allowing co-activation. This aspect is depicted in fig. 4.5 as additional activation of the muscles provided by a stiffness controller (which is described later). The contribution of the stiffness controller is added through a *sum* block in the *Renshaw cell* box. The description of the stiffness controller is given in the next subsection.

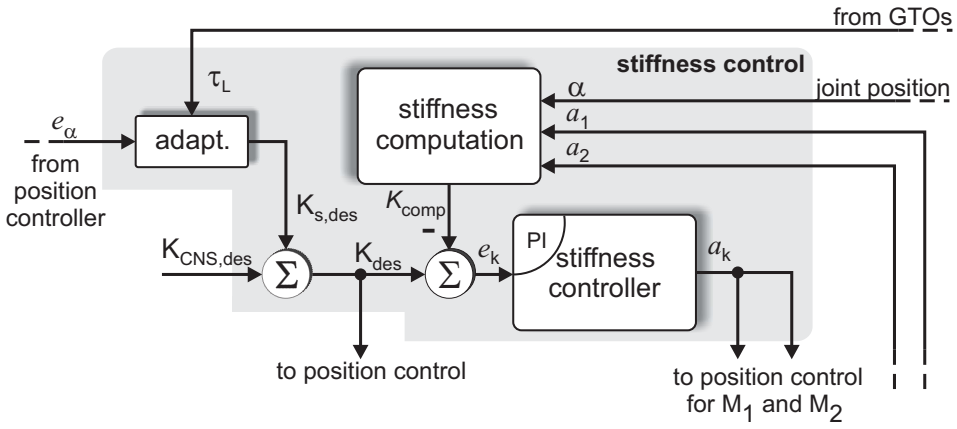

Fig. 4.6: Bio-inspired stiffness control scheme. The stiffness controller is modeled as a PI and its output (a_k) acts with the same strength on both muscles (co-activation). The block *stiffness computation* computes the actual stiffness based on the activations (a_1 and a_2) and the actual joint angle (α). The desired stiffness is the sum of the stiffness reference $K_{CNS,des}$ plus an adaptive part $K_{S,des}$ generated by the block *adapt.* and depending on the actual torque load τ_L and position error e_α.

4.2.4 Bio-inspired stiffness controller

As it was observed by Smith (1996), so far, no real stiffness controller could be found in biological systems. However, in this thesis, an explicit stiffness controller is proposed and its possible connection to the bio-inspired position control mechanism (as introduced before) is explained. The stiffness controller described here implements the balance of excitatory and inhibitory inputs onto the interneurons described in Section 4.2.2. Figure 4.6 depicts the bio-inspired stiffness controller. With respect to the basic stiffness control scheme of fig. 4.3(top box), this controller also integrates the stability aspects described in Section 4.1.

As shown in Section 4.1, when controlling the position, the stiffness is the key to concurrently control stability. For this purpose, the position error e_α is used as a stability measure (Burdet et al., 2006) in an adaptive scheme. The adaptive control block (*adapt.*) receives e_α and τ_L and has the goal to increase the desired stiffness coming from the CNS when an external load is applied. Therefore, the desired stiffness is composed of two parts:

$$K_{des} = K_{CNS,des} + K_{S,des} \tag{4.7}$$

where $K_{CNS,des}$ is the reference stiffness "coming from the brain" while $K_{S,des}$ is the additional stiffness coming from the adaptive block, defined as

$$K_{S,des} = \begin{cases} c_S \int_{t-T}^{t} |e_\alpha(t)| \ dt & \text{if } \tau_L \neq 0 \\ 0 & \text{otherwise} \end{cases} \tag{4.8}$$

with c_S defining the speed of adaptation and T the integration time. In this way, when

the position error becomes high, the desired stiffness increases and as a consequence muscles are more co-activated ensuring a higher stability and accuracy with respect to external perturbations for the joint (Chou and Hannaford, 1997). The stiffness controller is of the proportional-integral type (PI). From the stiffness error

$$e_{\mathrm{k}} = \mathrm{K}_{\mathrm{des}} - K_{\mathrm{comp}} \quad , \tag{4.9}$$

the controller generates the stiffness control value

$$a_{\mathrm{k}} = \mathrm{c}_{\mathrm{p,k}} \cdot e_{\mathrm{k}} + \mathrm{c}_{\mathrm{i,k}} \cdot \int e_{\mathrm{k}} \, \mathrm{dt} \tag{4.10}$$

with the proportional and integral controller gains $\mathrm{c}_{\mathrm{p,k}}$ and $\mathrm{c}_{\mathrm{i,k}}$. Both muscles receive the same activation value a_{k} (co-activation).

4.3 Bio-inspired position/stiffness control and simulation results

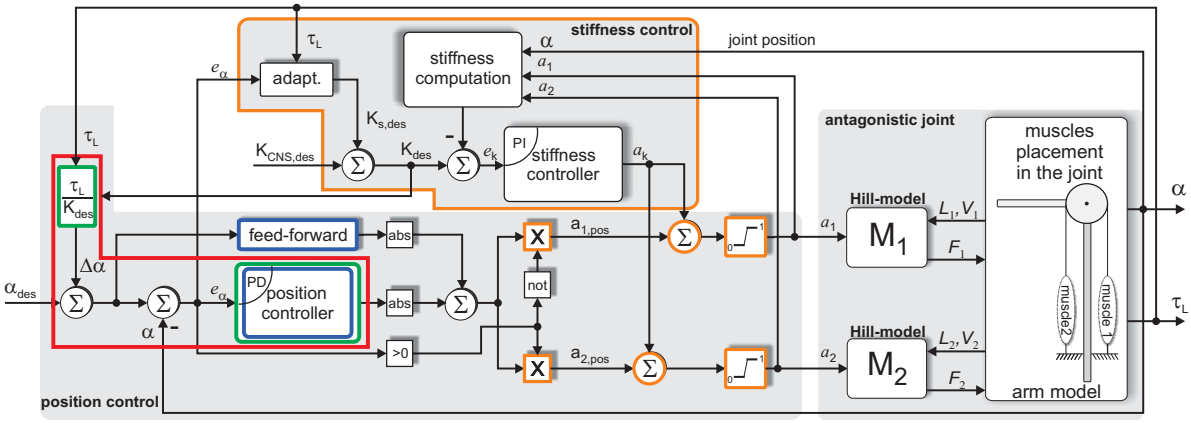

Fig. 4.7: Bio-inspired position/stiffness control scheme adopting the color code of fig. 4.4 and fig. 4.5. In orange are depicted the blocks related to the *Renshaw cell*. The PD position controller corresponds to the *muscle spindle* stretch-reflex loop (green) and α-MN (blue). The feed-forward in position refers to the α-MN. The block for the spring-like muscle behavior when a load is applied corresponds to the muscle-spindle position controller (green).

Figure 4.7 depicts the bio-inspired *position/stiffness* controller as a result of the modeling of biological components and physiological properties shown in Section 4.2. The colors adopted in the figure refer to the blocks described above. The position controller (on the left side) is of the proportional-derivative (PD) type and activates either *muscle 1* (M1) or *muscle 2* (M2) depending on the desired joint position α_{des}. The PD controller

Table 4.2: Simulation parameters for the simulation of the bio-inspired position/stiffness control strategy of the antagonistic pulley joint setup.

Parameter	Description	Value	Unit
$c_{p,1} = c_{p,2}$	proportional gain position contr.	0.05	
$c_{d,1} = c_{d,2}$	derivative gain position contr.	0.001	
$c_{p,\alpha}$	proportional gain pos. contr. (α-MN)	50	
$c_{ff,\alpha}$	scaling gain feed-forward (α-MN)	0.005	
$c_{p,K}$	proportional gain stiffness contr.	0.05	
$c_{i,K}$	integral gain stiffness contr.	6	
c_S	proportional gain adaptive contr.	0.25	
T	integration time	500	ms

implements the feedback regulation of muscles realized by *muscle spindle*, α-MN and *Renshaw cell*. The spring like behavior when an external load is applied as well as the feed-forward for the position are also included. The stiffness controller (top box) activates both muscles at the same time and includes the adaptive mechanism for the stability issues discussed in Section 4.1.

For the hinge joint described in Section 2.1.3, a simulation is performed in order to verify the performances of the bio-inspired *position/stiffness* control scheme and to show that the results comply with those obtained in biological experiments (Milner, 1993; Suzuki et al., 2001). The control scheme is tested in the case of a a contact with an obstacle, which is equivalent to a stiff spring mechanically coupled with the tip of the lever [fig. 4.8(a,b)] and in the presence of different perturbing forces [fig. 4.8(c,d)]. Depending on the frequency of the perturbation, the stiffness is adjusted by the adaptive control mechanism. For low frequency perturbations the joint is compliant, while for rapid perturbations joint stiffness increases and the effect of the external force is reduced (Humphrey and Reed, 1983). A medium level of stiffness is desired as it is considered an optimal value during joint movement (Hasan, 1986). The control scheme and the musculoskeletal joint setup were modeled in Matlab/Simulink® 7.11 (The MathWorks Inc., Natick, MA, USA). Simulation parameters for the controllers are given in Table 4.2.

The test results are depicted in fig. 4.9. The lever arm was commanded to follow a sinusoidal trajectory till $t = 6\,\mathrm{s}$ and then to keep a constant position ($\alpha_{des} = -0.3\,\mathrm{rad}$). The desired stiffness is constant ($K_{des} = 3\,\mathrm{Nm/rad}$). From $t = 2\,\mathrm{s}$ to $t = 4\,\mathrm{s}$, an obstacle ("collision") in the form of a stiff spring ($K_x = 10 \cdot 10^3\,\mathrm{N/m}$), which is mechanically coupled with the tip of the lever, forces the arm to remain at $\alpha = -0.1\,\mathrm{rad}$. Stiffness increases as the "collision" takes place and grows until the obstacle is removed, then it goes back to the desired value. At $t = 4\,\mathrm{s}$ the obstacle is removed and the lever returns to the desired trajectory. From $t = 8\,\mathrm{s}$ to $t = 12\,\mathrm{s}$, a low frequency sinusoidal load τ_L (amplitude 2 Nm and frequency 4 rad/s) is applied to the extremity of the lever arm. The generated compliant behavior (stiffness remains low) makes sure that the link follows the external load. From $t = 12\,\mathrm{s}$ to $t = 16\,\mathrm{s}$, a high frequency sinusoidal

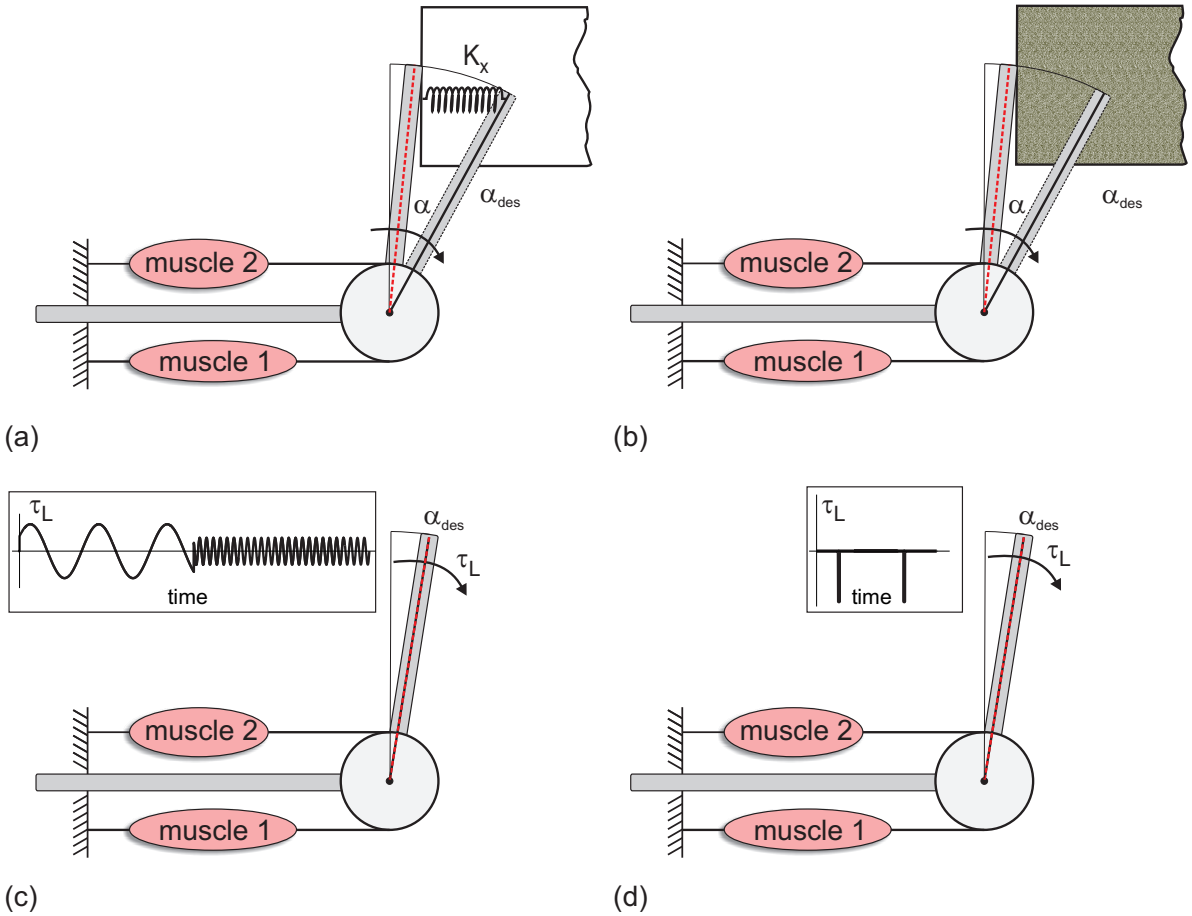

Fig. 4.8: Disturbance produced in simulation to test the bio-inspired control scheme for the antagonistic musculoskeletal setup. In (a) the presence of an obstacle in the desired path is equivalent to a stiff spring connected to the tip of the lever, which does not allow the lever to reach the desired position α_{des} (the potential lever for $\alpha = \alpha_{\text{des}}$ is shown in dashed line). The disturbance in (a) is equivalent to the presence of an obstacle in the desired path [cmp. (b)]. (c) sinusoidal disturbance of low and high frequency, as shown in the inset, are applied to the lever arm. (d) same as (c) but for impulsive disturbances.

perturbation τ_{L} (amplitude 2 Nm and frequency 40 rad/s) is applied to the extremity of the lever arm. In this case, the adaptive controller increases the desired stiffness in order to stabilize the system and to reduce the disturbance on the position due to τ_{L}. From $t = 16$ s to $t = 20$ s, two torque pulses load τ_{L} (amplitude -5 Nm and duration 20 ms) are applied to the extremity of the lever arm. Also in this case, desired joint stiffness increases which produces a stabilizing effect for the limb.

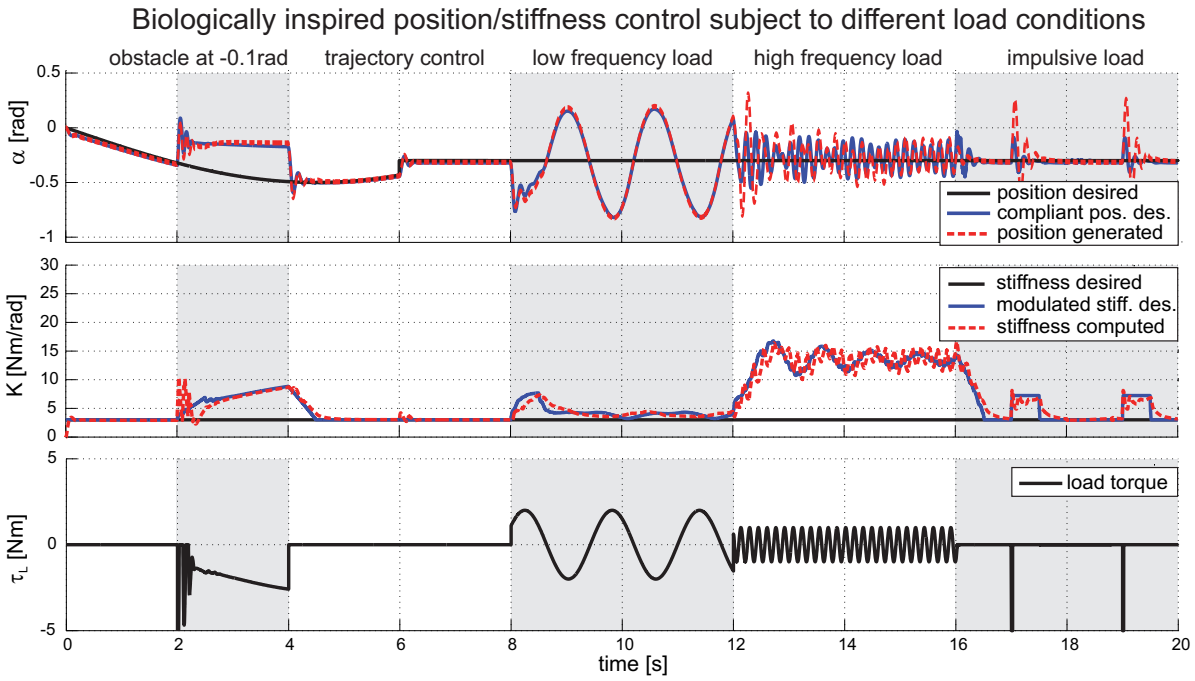

Fig. 4.9: Simulation results of the bio-inspired position control scheme with compliance adaptation in presence of different perturbing torques. According to the perturbation, joint stiffness adapts producing a stabilizing effect at joint level.

4.4 Summary

Different studies on biological systems give evidence that movement and joint impedance can be regulated separately. Reciprocal activation among antagonistic muscles pulling at the same joint results in a net joint torque which is used to control the position. Antagonistic muscle co-activation is used by the nervous system to control the impedance at the joint and to affect the stability of the limb. In this chapter, after a stability analysis performed for increasing muscle co-activations (Section 4.1), a novel position and stiffness control strategy that uses virtual muscles in combination with bio-inspired control concepts such as co-contraction is presented. The novelty of this controller lies in the adoption of nonlinear muscle actuation in an antagonistic arrangement and in the implementation of an adaptive regulation mechanism which models physiological properties (Section 4.2). Simulation results for different disturbances demonstrate that the bio-inspired control approach is able to follow the desired position and adapt joint stiffness according to the perturbation thus producing a stabilizing effect at the joint (Section 4.3). These results are in line with experimental results shown for the human behavior (Milner, 1993; Suzuki et al., 2001).

Chapter 5

Application of the bio-inspired control laws on a compliant rotatory joint drive

In Chapter 4, a novel bio-inspired scheme for controlling position and stiffness of an elbow joint was designed and evaluated in simulation. In this chapter, a rotatory joint drive, developed in our working group, is adopted to test and validate this bio-inspired control strategy. First, the robotics joint drive is introduced (Section 5.1) showing that its design fulfills the safety characteristics addressed by Bicchi and Tonietti (2004) as it presents a lightweight construction and integrates a real elasticity. Then, a dynamics model of the actuator is obtained and its parameters are identified (Section 5.2). Based on the identified model, a cascade control of motor speed and output torque is designed. Finally, the controlled drive is tested, first, using a classic interaction control approach (PD position control), then using the novel bio-inspired scheme (Section 5.3). Experimental results for different external perturbations are shown in Section 5.4.

5.1 Compliant robotics joint drive: design and identification

A simplified human elbow joint with two muscles is shown in fig. 5.1(a, left). α is the joint angle and τ_{net} is the net-torque produced by the virtual muscles pulling at the elbow joint. $J_{\text{arm,model}}$ is the inertia of the forearm. In Chapter 2, a mathematical model of the elbow joint was discussed and different muscle activation schemes were tested to study its dynamic behavior and mechanical impedance. Based on this model, in Chapter 4 a bio-inspired control scheme was designed to activate the muscles with mechanisms found in the CNS of vertebrates, to reach the desired joint position and stiffness.
With the objective to test and validate this bio-inspired control strategy in real experiments, a rotatory lightweight joint drive with inherent elasticity, designed and built by Paskarbeit et al. (2013), was used in this thesis. Figure 5.1(a, right) depicts the robotics joint drive with a lever arm mounted on the output side. Table 5.1 reports the

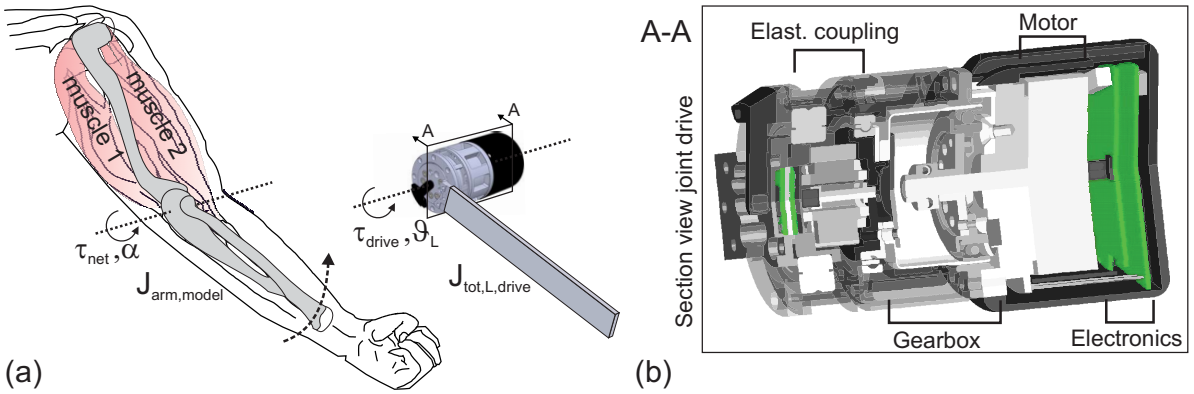

Fig. 5.1: (a) Simplified human elbow joint with two muscles (left) and robotic joint drive with a lever arm (right). (b) Section view of the joint drive in (a). The electronics is shown in green.

technical data of the drive. ϑ_{L} is the joint angle and τ_{drive} is the torque generated at the drive-output. $\mathrm{J}_{\mathrm{tot,L,drive}}$ is the total load side inertia of the joint drive.

The objective is to control the robotics drive such that an equivalent behavior with the simplified model of the human elbow joint is realized. The illustration in fig. 5.2 exemplifies the control strategy idea. Two masses M and m are driven by two forces, F and f, respectively that produce a displacement of the masses X and x. The Newton's equations for the masses are:

$$m\,\ddot{x} = f$$
$$M\,\ddot{X} = F.$$

Assuming that M is the mass of the model that has to be reproduced (subject to a certain force F) and m is the mass of the drive (with f being the force that the controller has to generate), two cases can be considered such that the condition $\ddot{x} = \ddot{X}$ is realized. If $m = M$, the control force f has to equal the force F. If $m \neq M$, the force f has to be $f = \frac{m}{M}F$, i.e. the difference of masses is considered for the evaluation of the control force f.

Table 5.1: Technical data of the rotatory joint drive.

Parameter	Value	Unit
length	~ 90	mm
diameter	~ 52	mm
max torque	~ 15	Nm
weight	~ 0.390	kg
power/weight	$\sim 130^a$	W/kg

[a] upgradable to 350 W/kg

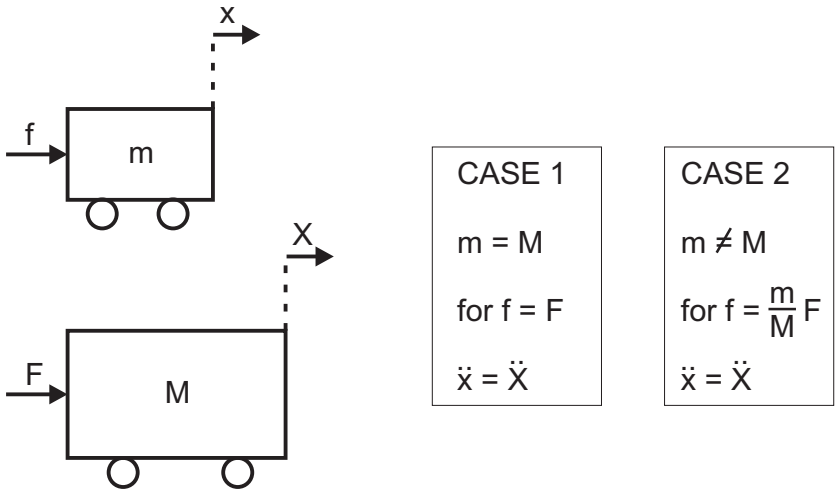

Fig. 5.2: Exemplification of the control strategy idea. On the top, a cart of mass m is subject to a control force f. On the bottom, the cart of mass M is subject to the force F. In order to have $\ddot{x} = \ddot{X}$ two cases can be considered. In *CASE 1*, the two masses are the same and as a consequence the control forces have to be the same. When the two masses are different (*CASE 2*), the control force f has to be modified accordingly.

Referring to fig. 5.1(a, left), for ease of exposition, and without loss of generality, in the following, $J_{arm,model} = J_{tot,L,drive}$ is considered and therefore, to realize an equivalent behavior between the simplified human elbow joint and the robotics drive, the torque τ_{drive} has to equal the net-torque τ_{net}.

Figure 5.1(b) shows a section view of the compliant joint drive. Motor, gearbox, elastomer coupling and electronics are pointed out. In the following section, first the mechatronics components of the actuator will be shortly described. Then, the integrated elasticity in form of an elastomer coupling will be presented together with its torque/torsion model. Finally, the dynamics model of the complete joint drive will be derived.

5.1.1 Mechatronic setup

The compliant robotics joint drive consists of a flat brushless DC motor with external rotor (DC Maxon EC45-flat, 24 V, 50 W), a lightweight harmonic drive gearbox (CPL-2A, size 14, with reduction ratio of 100) and a serial elastic element (elastomer coupling) placed in the output. Absolute rotatory encoders are used to measure the axis angle at different positions. An absolute rotatory encoder iC-MH (from iC-Haus) with high resolution (12 bits) is coupled to the motor and is used for the commutation and speed control. Another absolute rotatory encoder (Austria Microsystems, Model AS5245, 12 bit resolution, absolute) is mounted between the gearbox flexspline and the load and measures the elastomer torsion. A third encoder (AS5245) measures the output shaft position. A miniaturized power- and control-electronics is integrated into the back of the

actuator. The control electronics board utilizes a microcontroller (Atmel ATXMEGA 128A1) which is responsible for processing the multiple sensory inputs and on which the joint control schemes are implemented.

5.1.2 Elastomer coupling model

As it was pointed out in Chapter 1, passive elasticity in the form of a serial elastic element within the robotic joint drive has multiple benefits. First, it protects the gearbox from torque peaks which might occur during collisions with the environment. Second, in a certain bandwidth it is possible to actively control the compliances. For higher frequency contacts (higher than the bandwidth of the controller), the real elastic element reacts in real time with its inherent elastic properties thus attenuating the stroke. Third, it is possible to estimate the torque applied at the output if its torque/torsion model is available. For the elastomer coupling integrated in the joint drive, a complete explanation of its design and its identification procedure is given by Paskarbeit et al. (2013). It needs to be pointed out that, due to the high damping characteristics of the elastomer material used, an hysteresis effect is observable in the torque/torsion curve. The approach for identification and modeling of the elastomer coupling was based on test data. Although the system to identify presented nonlinearities, due to the limited computational capacity of the drive's embedded microcontroller, a linear model of the elastomer coupling was sought[1]. The obtained torque/torsion model was a second order transfer function, and consisted of two parallel spring-damper-subsystems in series and a serial spring. Called ECM(s), the elastomer coupling model in the Laplace transform, the following relation holds true

$$T_S(s) = ECM(s) \cdot \Theta_S(s) \quad , \tag{5.1}$$

with $\Theta_S(s)$ Laplace transform of the elastomer torsion angle and $T_S(s)$ the corresponding transmitted torque.

To test the estimation performances of the elastomer coupling model implemented in the microcontroller, Paskarbeit et al. (2013) performed the following experiment: At the extremity of the lever arm attached at the output shaft of the drive a mass was attached. Rotations of the lever arm with the mass were performed. Ten cycles were carried out for low and high frequency movements. The output torque of the model was compared with the calculated torque around the pivot point. Figure 5.3 depicts the hysteresis curves of the estimated torque plotted over the torsion for low (a) and high frequency (b) load changes, respectively. The gray line represents the calculated torque, while the black line represents the output of the model. As it can be seen, the torque/torsion lumped model is able to account for the hysteresis effect for both high and low load changes frequencies. The identified model is able to reproduce the measured data in a range of $\pm$ 8 Nm. Tests in a higher torque range have not been performed.

[1] With a linear model the complexity of the required calculations is reduced.

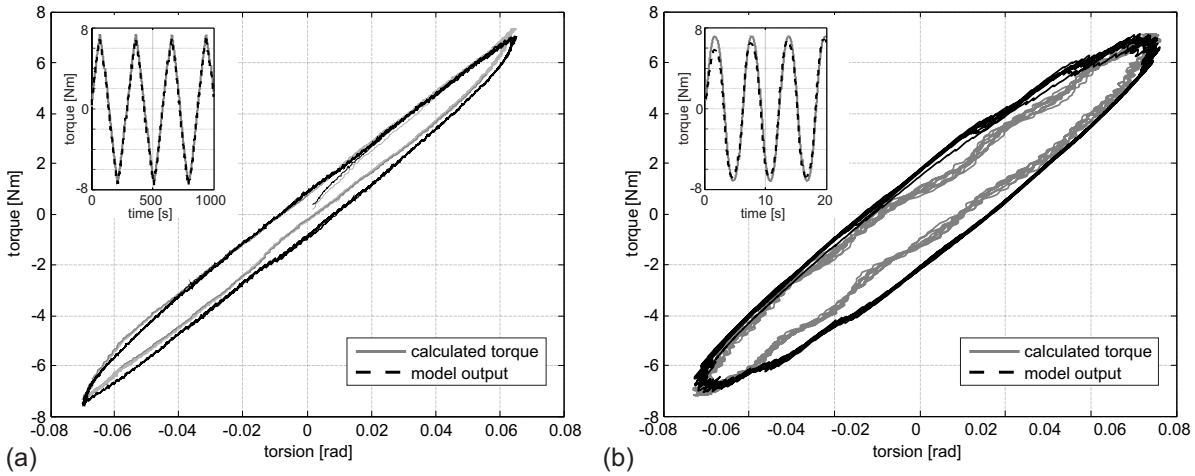

Fig. 5.3: Hysteresis curves of the estimated and calculated torque plotted against the torsion as obtained by Paskarbeit et al. (2013). (a) for low frequency load changes. (b) for high frequency load changes. The insets show a section of the calculated and estimated load plotted over time.

5.1.3 Mechanical model of the compliant joint drive

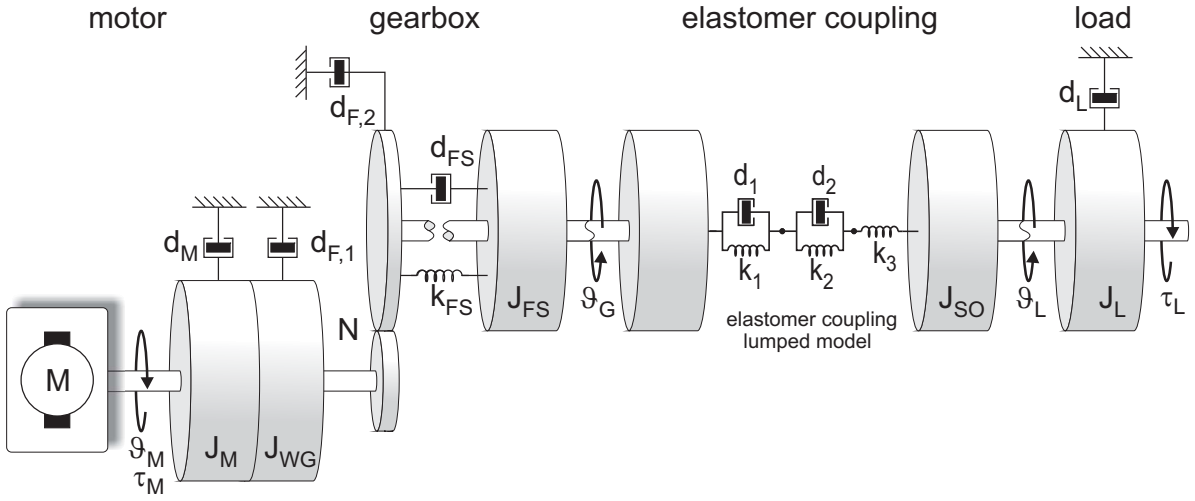

Fig. 5.4: Mechanical model of the compliant joint drive containing the elastomer coupling lumped model.

In this section, the dynamic model of the compliant actuator will be derived. Figure 5.4 shows a schematic depiction of the mechanical parts composing the joint. The motor is connected to the gearbox whose compliant behavior is approximated with a spring-damper model (Taghirad and Bélanger, 1998). The elastomer coupling is integrated between the gearbox and the load and its model is adopted to estimate the transmitted torque in dependence of the elastomer torsion angle (Paskarbeit et al., 2013). Values of the physical parameters in the elastomer coupling model as obtained through identifi-

Table 5.2: Elastomer coupling lumped model parameters.

Parameter	Value	Unit
d_1	124.42	N m s / rad
d_2	771.19	N m s / rad
k_1	217.89	N m / rad
k_2	32.30	N m / rad
k_3	99.52	N m / rad

cation are listed in Table 5.2. The other parameters shown in the mechanical model are described in Table 5.3.

Some assumptions can be made in order to reduce the number of model parameters. The shaft connecting the inertias J_M and J_{WG} is rigid. Therefore, only one total inertia, $J_{tot,M}$, (motor side inertia) which includes motor and wave generator inertias, can be considered in the model. The same holds true for the inertias J_G and J_{SI}, and for J_{SO} and J_L for which the total inertias (gear-elastomer side and load side) $J_{tot,G}$ and $J_{tot,L,drive}$ are adopted, respectively. The resulting system can be divided in a three-mass model (Wernholt and Gunnarsson, 2005). Figure 5.5(a) shows the decomposed model and points out all torques acting on each of the three masses. On the motor side, d_F is the friction parameter which takes into account motor friction (d_M), wave generator friction ($d_{F,1}$) and gear meshing friction ($d_{F,2}$). τ_{DF} is the corresponding friction torque. τ_{MG} is the transmitted torque to the gearbox. On the gear-elastomer side, τ_{GL} is the torque on the low speed-high torque side and τ_S is the torque transmitted by the elastomer coupling from the load. On the load side, τ_{DL} is the friction torque at the load.

For a 1-DoF robotics joint not affected by gravity, the dynamics model of the three-mass model is:

$$\begin{cases} J_{tot,M} \cdot \ddot{\vartheta}_M &= \tau_M - \tau_{MG} - \tau_{DF}(\dot{\vartheta}_M) \\ J_{tot,G} \cdot \ddot{\vartheta}_G &= \tau_{GL} - \tau_S(\vartheta_S, \dot{\vartheta}_S) \\ J_{tot,L,drive} \cdot \ddot{\vartheta}_L &= \tau_S(\vartheta_S, \dot{\vartheta}_S) - \tau_{DL}(\dot{\vartheta}_L) - \tau_L \end{cases} \tag{5.2}$$

with ϑ_S elastomer coupling torsion angle and

$$\tau_{GL} = \tau_{d,FS}\left(\frac{\dot{\vartheta}_M}{N}, \dot{\vartheta}_G\right) + \tau_{k,FS}\left(\frac{\vartheta_M}{N}, \vartheta_G\right) \quad , \tag{5.3}$$

$$\tau_{MG} = \frac{\tau_{GL}}{N} \quad . \tag{5.4}$$

Table 5.3: Mechanical model parameters of the compliant joint drive.

Parameter	Description	Unit
J_M	motor moment of inertia (rotor)	$kg\,m^2$
J_{WG}	gearbox moment of inertia (wave generator)	$kg\,m^2$
J_{FS}	gearbox moment of inertia (flexspline)	$kg\,m^2$
J_{SI}	elast. coupling moment of inertia (input side)	$kg\,m^2$
J_{SO}	elast. coupling moment of inertia (output side)	$kg\,m^2$
J_L	moment of inertia of the load	$kg\,m^2$
ϑ_M	motor position	rad
ϑ_G	gearbox output position	rad
ϑ_L	load position	rad
d_M	friction of the motor	$N\,m\,s\,/\,rad$
$d_{F,1}$	wave generator friction	$N\,m\,s\,/\,rad$
$d_{F,2}$	gear meshing friction	$N\,m\,s\,/\,rad$
d_L	friction of the link	$N\,m\,s\,/\,rad$
d_{FS}	flexspline structural damping	$N\,m\,s\,/\,rad$
k_{FS}	gearbox coefficient of elastic torsion	$N\,m\,/\,rad$
N	gearbox reduction ratio	
τ_M	motor torque	N m
τ_L	load torque	N m

5.2 Identification of the joint drive model parameters

In this section, the model parameters of equations (5.2) are evaluated. Some parameters are directly provided by the manufacturers. Other parameters are obtained from the CAD drawing. Finally, some more parameters have to be directly identified. Different identification procedures could be used. In this work, the identification is performed in time domain and adopting the physical model. In this process, linear and nonlinear optimization techniques are run on measured data. In a later stage, a gray-box identification is performed to fine-tune those parameters in the dynamics model.

5.2.1 Moments of inertia and gearbox torsional stiffness

The total moments of inertias of the three main bodies in the joint drive model are obtained partly from the 3D CAD drawing in SolidWorks® (Dassault Systèmes SolidWorks Corporation) and partly from the knowledge of the values directly specified by the manufacturers (like for the BLDC rotor and gearbox wave generator). The final values are reported in Table 5.4.

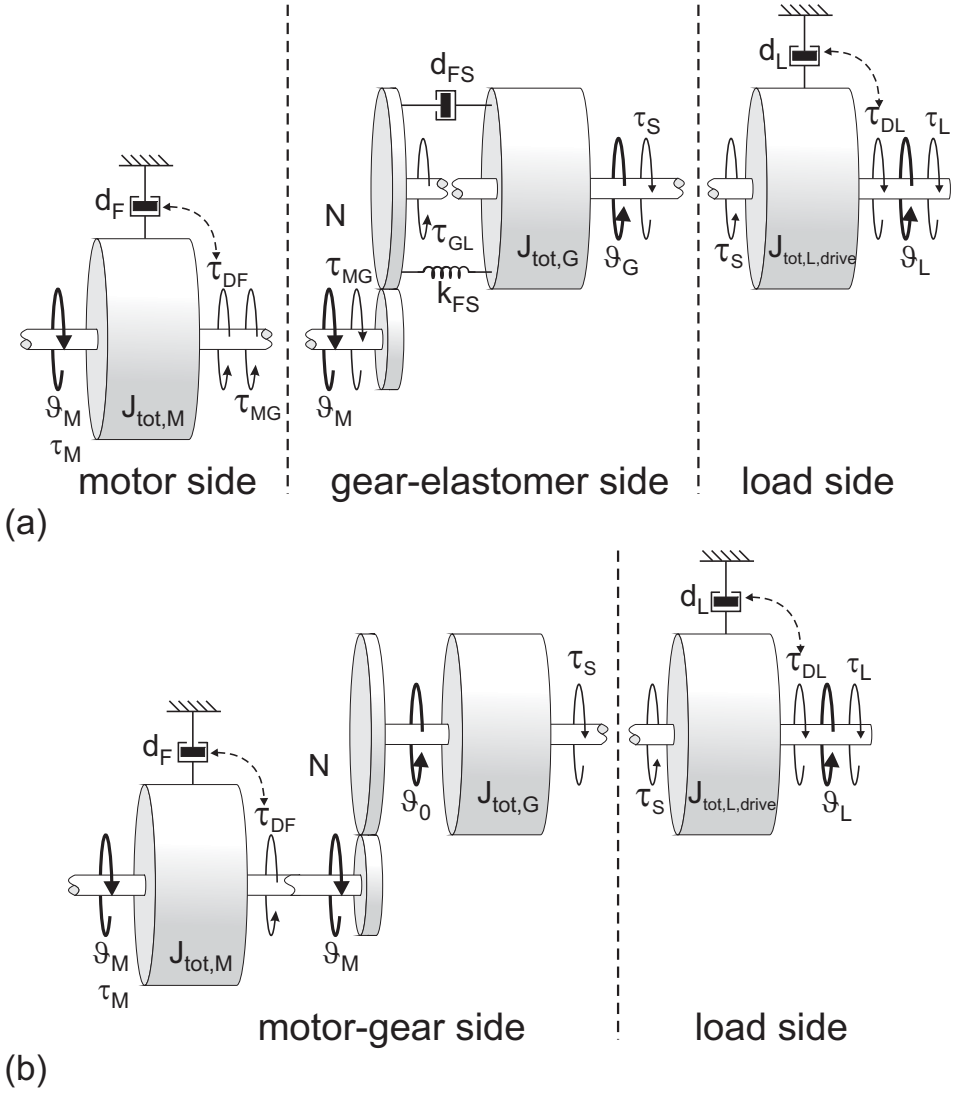

Fig. 5.5: (a) Decomposition scheme of the mechanical model (three-mass model). (b) Same as (a) but for the case of rigid gearbox (two-mass-model).

The gearbox compliance, usually called torsional stiffness, is typically modeled with a piecewise linear function [see Harmonic Drive catalog (Harmonic Drive AG, 2012)]. In this work, it was preferred to adopt a cubic (subscript C) and a liner (subscript L) model:

$$\tau_{\mathrm{k,FS,C}} = \mathrm{k_{FS,1}} \cdot \left(\frac{\vartheta_{\mathrm{M}}}{\mathrm{N}} - \vartheta_{\mathrm{G}} \right) + \mathrm{k_{FS,3}} \cdot \left(\frac{\vartheta_{\mathrm{M}}}{\mathrm{N}} - \vartheta_{\mathrm{G}} \right)^3$$

$$\tau_{\mathrm{k,FS,L}} = \mathrm{k_{FS}} \cdot \left(\frac{\vartheta_{\mathrm{M}}}{\mathrm{N}} - \vartheta_{\mathrm{G}} \right) \quad .$$

Experimental tests were performed with the drive containing only motor and gearbox. Torque measurements were obtained mounting a torque sensor at the gearbox output

Table 5.4: Total moments of inertia evaluation as obtained from the CAD model and catalogs (Harmonic Drive AG, 2012; Maxon Motor AG, 2012).

Parameter	Description	Value·10^{-6}	Unit
$J_{tot,M}$	motor side inertia	15.8	$kg\,m^2$
$J_{tot,G}$	gear-elastomer side inertia	3.7	$kg\,m^2$
$J_{tot,L,drive}$	load side inertia	4.3	$kg\,m^2$

while the other side of the sensor was clamped. Torques in the range of ±8 Nm were measured and nonlinear and linear regressions were applied on measured data to estimate the unknown coefficients of the models. Table 5.5 reports the results from the identification procedure for the cubic and linear model.
The equivalent stiffness of the gearbox flexspline is fifty times higher than the elastic properties of the elastomer coupling (where the equivalent stiffness was ≈ 100 [N m/rad], see Table 5.2). Therefore, for modeling purpose, the elastic properties of the flexspline can be neglected. Similarly, the flexspline damping, d_{FS}, can be neglected too and the gearbox can be considered rigidly coupled to the motor side. As a consequence, the joint model can be further simplified [see fig. 5.5(b)] and the dynamics model of the joint can be reduced to a two-mass-model:

$$\begin{cases} (J_{tot,M} + \frac{J_{tot,G}}{N^2}) \cdot \ddot{\vartheta}_M & = \tau_M - \frac{\tau_S}{N} - \tau_{DF} \\ J_{tot,L,drive} \cdot \ddot{\vartheta}_L & = \tau_S - \tau_{DL} - \tau_L \quad . \end{cases} \tag{5.5}$$

5.2.2 Motor side friction

In the mechanical model of the compliant joint drive, the overall motor side torque friction, τ_{DF}, is composed of three components:

$$\tau_{DF}(\dot{\vartheta}_M) = \tau_{DM} + \tau_{F,1} + \tau_{F,2} \quad ,$$

where τ_{DM} is the motor torque friction, $\tau_{F,1}$ is the gearbox input torque friction and $\tau_{F,2}$ is the gear meshing torque friction.

Table 5.5: Torsional stiffness parameters as obtained after the identification process.

Parameter	Value	Unit
$k_{FS,1}$	4834	N m / rad
$k_{FS,3}$	4710·10^5	N m / rad^3
k_{FS}	5718	N m / rad

The *Rigid Body Dynamics* (RBD) method (Tsai, 1999) is adopted for its identification and two models (linear and nonlinear) are evaluated in this process. The experimental setup is composed of motor and gearbox. A commercially available controller (Elmo Motion Control®) is used to control the motor and collect the experimental data. Inner current and speed controllers are assumed to be very fast compared to the mechanical dynamics[2]. Therefore, the motor speed is assumed to equal the reference speed. For the actuator composed of only a motor and gearbox, the following equation holds true:

$$(\mathrm{J_{tot,M}} + \frac{\mathrm{J_{tot,G}}}{\mathrm{N}^2}) \cdot \ddot{\vartheta}_\mathrm{M} = \tau_\mathrm{M} - \tau_\mathrm{DF} \quad . \tag{5.6}$$

According to the RBD methodology, the input speed has to be constant. Therefore, in the experiment, the reference speed is a piecewise constant function (step function) [see fig. 5.6(a, top)]. Each step lasts 2.5 s. Speed amplitudes range from -30 rad/s to 30 rad/s. From $\dot{\vartheta}_\mathrm{M} \approx const$ follows that $\ddot{\vartheta}_\mathrm{M} \approx 0$ and equation (5.6) yields:

$$\tau_\mathrm{M} \approx \tau_\mathrm{DF} \quad . \tag{5.7}$$

Equation (5.7) forms a regression model in which the parameters in τ_DF are unknown, while the motor torque, τ_M, can be measured[3]. Two friction models are adopted in the identification process. One is a linear model (subscript L) while the other is the classical nonlinear friction model with static and dynamic viscosity [Coulomb plus viscous friction (Townsend and Salisbury, 1987), subscript V]:

$$\tau_\mathrm{DF,L} = \mathrm{F_{vl}} \cdot \dot{\vartheta}_\mathrm{M} \tag{5.8}$$

$$\tau_\mathrm{DF,V} = \mathrm{F_{vd}} \cdot \dot{\vartheta}_\mathrm{M} + \mathrm{F_{vs}} \cdot \ sign(\dot{\vartheta}_\mathrm{M}) \quad . \tag{5.9}$$

Using an iterative least squares algorithm for the regression model, the parameters that best describe the measured data are obtained. Figure 5.6(a) shows the identification data (motor speed and motor torque over time). Figure 5.6(b) depicts the friction characteristic obtained through interpolation of identification data (dashed line) and the friction characteristics of the two identified models (light gray and black line, respectively). Table 5.6 reports the values of the friction coefficients obtained in the identification process. Since the model that describes the measured data best is the nonlinear one, in the following, this model will be adopted.

5.2.3 Parameters optimization through gray-box identification

The model parameters obtained so far are used in this section as starting values for a gray-box identification which runs on the two-mass model of equation (5.5). The

[2]The current loop runs with a sampling time of 70 μs. The velocity loop runs with a sampling time of 140 μs. The motor mechanical time constant is 11.8 ms, which is 84 times higher than the velocity loop time.

[3]The measurement of the motor torque is based on the value of the motor current, directly provided by the controller Elmo Motion Control®.

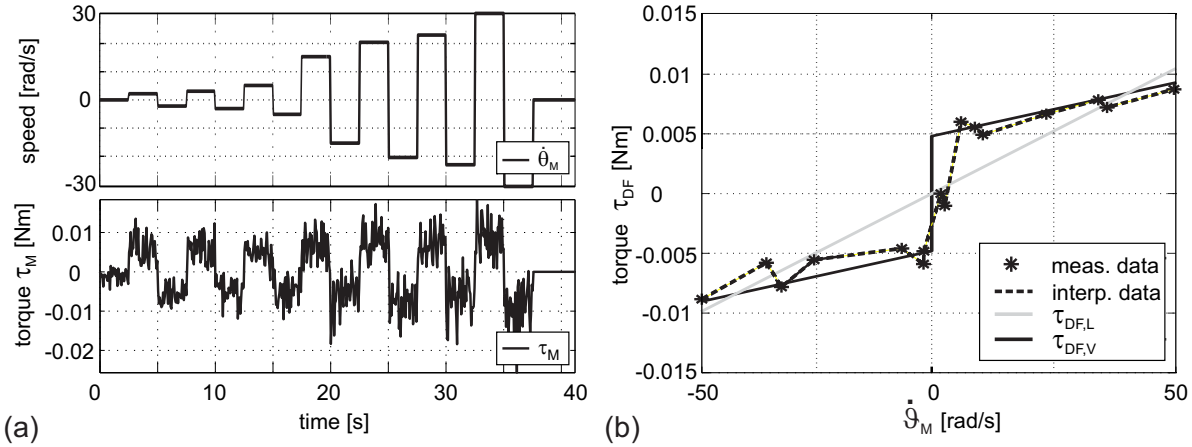

Fig. 5.6: (a) Motor side friction identification data: The reference speed (input signal) is shown on top while the measured motor torque is depicted on the bottom. (b) Star-shaped markers connected by the dashed line represent the data points from (a) assuming that equation (5.7) is valid. The light gray line shows the linear friction characteristic as obtained after parameters identification. The black line shows the same for the nonlinear model.

differential equations from the model are implemented in Matlab/Simulink® and the identification is run using the *Parameter Estimation Tool*™. In order to find the parameters of the system in the model, a *data-driven* modeling approach is pursued. In the experimental phase, the speed controller receives as input a series of periodic speed reference signals while motor current, position and speed values are recorded. In the identification process, these signals are provided to the joint model. For identification purpose, the model is considered to be a 1-input (motor torque), 2-outputs (motor position and speed) system. The objective of the gray-box identification is to find the vector of unknown parameters

$$\boldsymbol{\lambda} = [\mathrm{J_{tot,M}}, \mathrm{J_{tot,G}}, \mathrm{J_{tot,L,drive}}, \mathrm{F_{vd}}, \mathrm{F_{vs}}] \quad ,$$

that minimizes the function

$$V(\boldsymbol{\lambda}) = \frac{1}{\mathrm{n}} \sum_{t=1}^{\mathrm{n}} \epsilon(t, \boldsymbol{\lambda})^2 \quad ,$$

Table 5.6: Values for the friction model parameters.

Parameter	Description	Value	Unit
$\mathrm{F_{vd}}$	dynamic viscous friction coefficient	$1.49 \cdot 10^{-4}$	$\mathrm{N\,m\,s\,/\,rad}$
$\mathrm{F_{vs}}$	static viscous friction coefficient	$3.65 \cdot 10^{-3}$	$\mathrm{N\,m}$
$\mathrm{F_{vl}}$	viscous friction coefficient	$3.47 \cdot 10^{-4}$	$\mathrm{N\,m\,s\,/\,rad}$

Table 5.7: Model parameters values after gray-box identification.

Parameter	Value	Unit
$J_{tot,M}$	$18.64 \cdot 10^{-6}$	$kg\,m^2$
$J_{tot,G}$	$4.35 \cdot 10^{-6}$	$kg\,m^2$
$J_{tot,L,drive}$	$5.21 \cdot 10^{-6}$	$kg\,m^2$
F_{vd}	$1.49 \cdot 10^{-4}$	$N\,m\,s\,/\,rad$
F_{vs}	$4.3 \cdot 10^{-3}$	$N\,m$

where $\epsilon(t, \boldsymbol{\lambda})$ is the prediction error of the model between the measured output $\mathbf{y}$ and the predicted model output $\hat{\mathbf{y}}$:

$$\epsilon(t, \boldsymbol{\lambda}) = \mathbf{y}(t) - \hat{\mathbf{y}}(t, \boldsymbol{\lambda}) \quad .$$

The parameters in $\boldsymbol{\lambda}$ were constrained to vary in a range of 20% with respect to the starting values. Table 5.7 reports the values of the parameters after the identification process. The identified model parameters were validated adopting two arrays of data: *validation data 1* and *validation data 2*. The following results in terms of best fit (BF) were obtained:

$$BF(\text{validation data 1}) = 73.86\ \%$$
$$BF(\text{validation data 2}) = 75.74\ \% \quad .$$

Figure 5.7 shows motor position and speed for the two validation data sets. Measured data is in gray while the values from the model are shown in dashed black line.

5.3 Control of the loaded joint with fast system dynamics

In this section, two control strategies for the control of the interaction of a robotic joint with external forces are analyzed.
The first strategy is the classical compliance control approach in which the elasticity is mimicked by control (i.e. the control is designed to achieve a desired compliant behavior in the interaction with the environment) (Chiaverini et al., 1999; Hogan, 1985). The second is the approach presented in Chapter 4 in which the control of the interaction is based on the use of muscle models and virtual antagonistic joint geometries. The controller implements control strategies as found in the Central Nervous System of vertebrates for the achievement of a bio-inspired position/stiffness control. In the first case, the interaction is typically modulated via position control: a position control loop is closed in order to provide the joint with the desired stiffness and damping. Figure 5.8(a) depicts a classical position control based on a virtual spring-damper desired behavior.

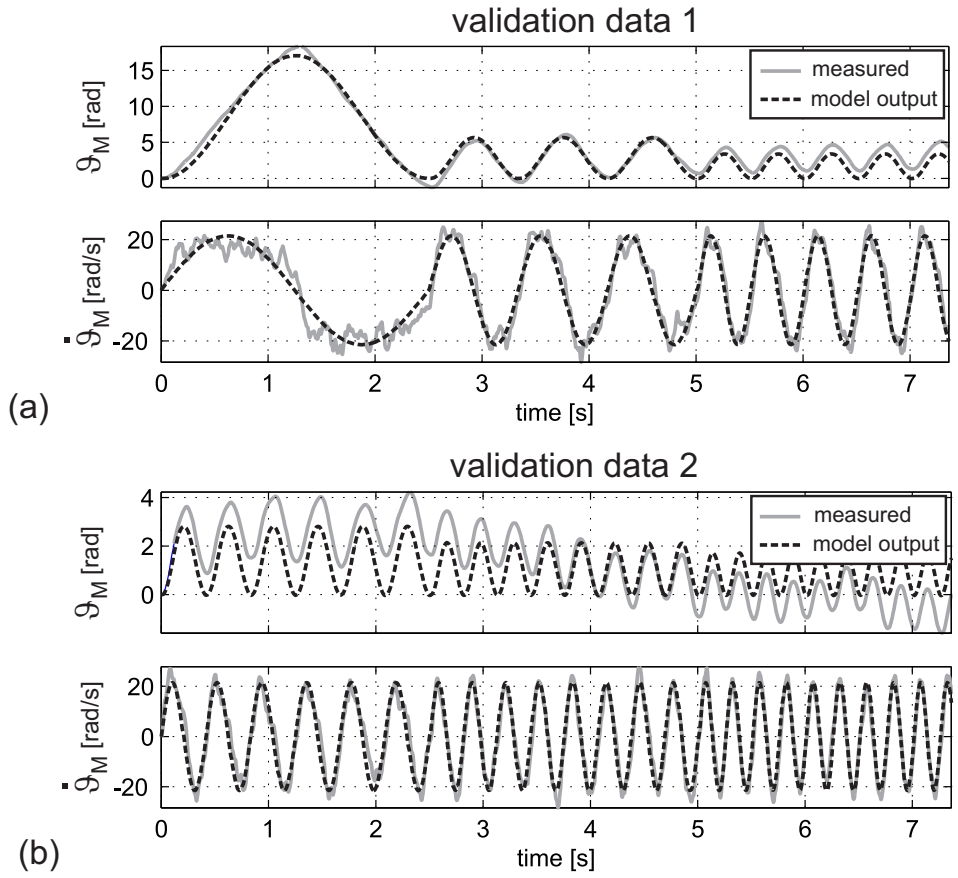

Fig. 5.7: (a) Results of the gray-box identification run for the model of the joint drive on the *validation data* 1. The gray solid line shows the measured data (motor position and velocity) while the black dashed line depicts the data as obtained from the simulation of the dynamics model. (b) Same as (a) but for *validation data* 2.

Given a desired spring constant (k_{des}) and damping constant (d_{des}), the control loop is closed on the joint drive position, ϑ_L, in order to reach the desired position, $\vartheta_{L,des}$. The classical approach will be implemented and used as reference and for comparison in the analysis of the experimental results with the second control approach.

The schematic of the second approach is depicted in fig. 5.8(b). In either case, the output value of the controller is a desired torque τ_{des}.

Both interaction control approaches are tested in this section on the compliant joint drive presented in Section 5.1 and Section 5.2. Figure 5.8(c) depicts a schematic representation of the joint drive (on the top) and the control scheme implemented in this thesis (on the bottom).
The top of the figure shows the mechanical components: the brushless DC motor (BLDC), the harmonic drive gearbox (HD), the elastomer coupling and the lever arm. High resolution rotary encoders for measuring the position of the motor shaft ϑ_M, the

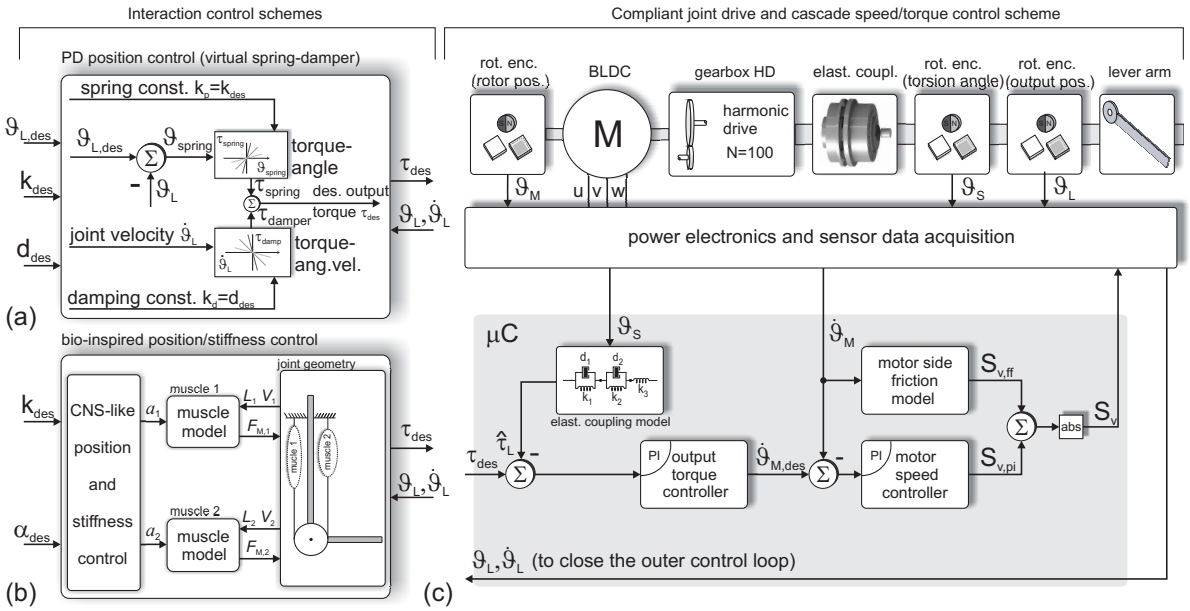

Fig. 5.8: (a) PD position control based on a virtual spring-damper system. (b) Schematic depiction of the bio-inspired control of position and stiffness as presented in Chapter 4. (c) Schematic view of the mechatronics system: the compliant actuator (on the top) and the control setup (on the bottom).

torsion ϑ_S of the elastomer and the output position ϑ_L are also included. The control and power electronics are responsible for the control of the motor, for the acquisition of the sensors signals (positions, motor temperature, phase currents, etc.) and for the communication with external controllers via a differential bus system.

A microcontroller (μC), shown at the bottom of the figure, contains the actuator control strategy. A cascade control approach was implemented. The innermost control loop (PI-controller) is closed on the motor speed thus realizing a velocity sourced - Serial Elastic Actuator whose reliability was shown by Wyeth (2006).
A *motor side friction model* takes advantage of the identification results described in Section 5.2.2 and generates a feed-forward control signal to compensate the friction at the motor side.
The *elastomer coupling model* block implements the torque/torsion behavior of the elastomer coupling. Based on the torsion angle, ϑ_S, a torque estimation, $\hat{\tau}_L$, of the actual torque applied at the load can be obtained. A torque control loop is then closed on the estimated torque (PI-controller). The desired torque, τ_{des}, for the controller, could be provided either by a classical position control or by a bio-inspired control approach as explained above.

For the description of the control strategy, it is referred to a classical generic control architecture with negative feedback, as depicted in fig. 5.9. C is the control system and G is the plant to control. r is the reference, u is the control signal, y is the plant output and e is the error between the reference and the feedback signal.

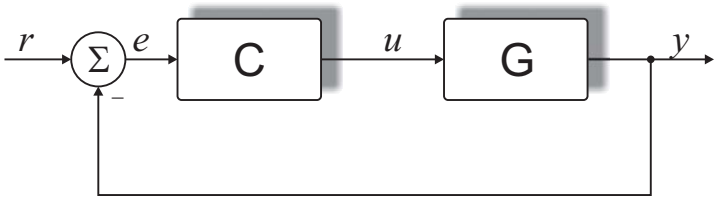

Fig. 5.9: Generic control architecture with negative feedback.

Assuming the nonlinearity on the motor side friction completely compensated[4] in the following, the system to control is LTI[5] and therefore the description in terms of transfer functions (t.f.) and Laplace transforms can be considered. As a consequence, $G(s)$ indicates the t.f. of the system to control and $C(s)$ refers to the controller t.f.. Furthermore, the open loop t.f. is indicated with $F(s) = C(s) \cdot G(s)$, the t.f. from the reference signal to the control signal with $Q(s) = \frac{C(s)}{1+F(s)}$ and the closed-loop t.f. with $W(s) = \frac{F(s)}{1+F(s)}$. For each of them, the subscript indicates to which loop they refer: ω is the velocity loop, τ is the torque loop and p is the position loop.

5.3.1 Motor speed control and friction compensation

The control of the motor speed is realized adopting the Pulse-Width Modulation (PWM) strategy. The control loop runs with a frequency of 20 kHz while the commutation of the electronics with a frequency of 10 kHz. The duty cycles to the power electronics are scaled with the output of the rotor speed controller S_{v} [see fig. 5.8(c)]. Aside from a feedback loop, a feed-forward control contribution is based on the identification of the motor side friction obtained in Section 5.2.2. The feed-forward control signal for friction compensation is [cmp. to equation (5.9) and refer to fig. 5.8(c)]:

$$S_{\mathrm{v,ff}} = \mathrm{F_{vd}} \cdot \dot{\vartheta}_{\mathrm{M}} + \mathrm{F_{vs}} \cdot sign(\dot{\vartheta}_{\mathrm{M}}) \quad .$$

Figure 5.10 shows a schematic depiction of the innermost control loop (motor speed loop), that uses the transfer function names as introduced above. $G_\omega(s)$ is the system between the torque control and the motor speed. $C_\omega(s)$ is the motor speed controller. $F_\omega(s)$ is the open-loop transfer function between the reference $\dot{\vartheta}_{\mathrm{M,des}}$ and the control variable $\dot{\vartheta}_{\mathrm{M}}$.

The desired performances for the motor speed feedback control loop are, for a step input, a zero steady-state error and an overshoot $\mathrm{M_p} \leq 20$ % with a settling time[6] $t_{\mathrm{s}} \leq 100$ ms. A controller that satisfies the specification on the steady-state error is a PI-controller

[4] See Section 5.3.1 for details.

[5] Linear Time Invariant.

[6] The settling time, t_{s}, here is defined as the time the motor speed takes to get within 5% of the steady-state value, or to 95% of the steady-state value and stay within that 5%.

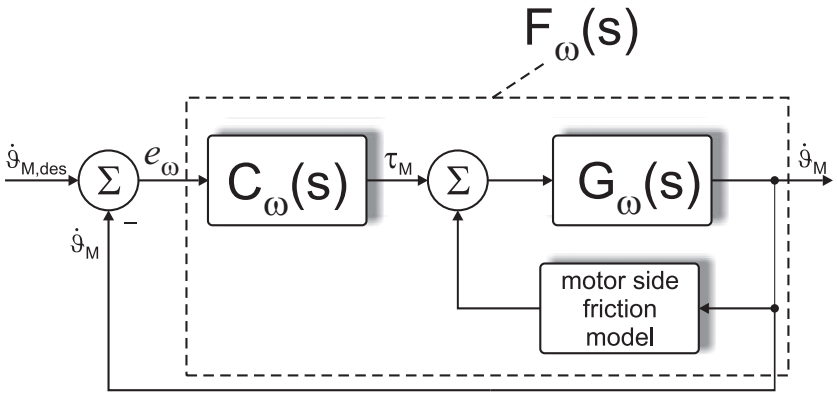

Fig. 5.10: Block diagram of the motor speed control loop with motor side friction compensation.

with the following t.f.:

$$C_\omega(s) \;=\; \mathrm{k}_\omega + \frac{\mathrm{i}_\omega}{\mathrm{s}} \;=\; \frac{\mathrm{k}_\omega}{\mathrm{s}}\,(\mathrm{s} + \frac{\mathrm{i}_\omega}{\mathrm{k}_\omega}) \tag{5.10}$$

which has a pole in the origin and a zero in $\frac{\mathrm{i}_\omega}{\mathrm{k}_\omega}$. The rotor speed error is:

$$e_\omega = \dot{\vartheta}_{\mathrm{M,des}} - \dot{\vartheta}_{\mathrm{M}} \quad .$$

The objective is to find the control parameters in $C_\omega(s)$ such that the requirements are fulfilled. The conditions on overshoot and settling time result in a damping ratio $\zeta = 0.45$ which corresponds to a phase margin[7] $\varphi_{\mathrm{M}} \approx 45°$ and a closed-loop bandwidth lower than 200 rad/s. Based on these requirements, the zero $\frac{\mathrm{i}_\omega}{\mathrm{k}_\omega}$ of equation (5.10) was placed at 100 rad/s. For the selection of the controller gain k_ω, a condition on the maximum value of the control signal was taken into consideration. Referring to fig. 5.8(c), the output of the motor speed controller is the PI contribution $S_{\mathrm{v,pi}}$. The signal $S_{\mathrm{v,pi}}$, together with $S_{\mathrm{v,ff}}$, is the scaling factor for the duty cycles in the power electronics that controls the motor. The maximum value should be selected such that the maximum motor torque, $\tau_{\mathrm{M,max}}$, is not exceeded. This condition reflects on the design of the t.f. $Q_\omega(s)$ and can be evaluated applying the *Initial and Final Value Theorems*.

Figure 5.11 depicts the Bode diagram for the rotor speed control design. Since the dominant behavior of the motor side dynamics system $G_\omega(s)$ is one of a first order system, for a desired speed $\dot{\vartheta}_{\mathrm{M,des}}$, the control signal τ_{M} at start and at steady-state can be approximated as:

$$\lim_{\omega\to\infty} Q(j\,\omega) = k_\omega\,\dot{\vartheta}_{\mathrm{M,des}} \quad \text{and} \quad \lim_{\omega\to 0} Q(j\,\omega) = \frac{\dot{\vartheta}_{\mathrm{M,des}}}{G_\omega(j\omega)}$$

[7]For phase margins below 70°, the approximation $\zeta = \frac{\varphi_{\mathrm{M}}}{100}$ holds true.

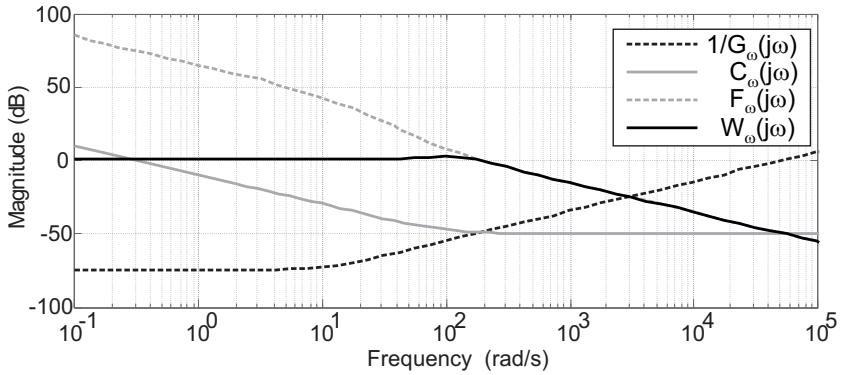

Fig. 5.11: Bode diagram of the transfer functions characterizing the motor speed control loop design.

for which, given the maximum[8] $\dot{\vartheta}_{\mathrm{M,des}}$ and taken into consideration that $1/G_\omega(j\,0) \approx -60$ dB (see dashed black line in fig. 5.11), the conditions above set limits on the value of k_ω.

Table 5.8 reports the values of the control parameters. The discrete version of the motor speed controller was implemented in the microcontroller with a control loop time of 1 ms. Figure 5.12(a) shows the measured control signal τ_M and the fulfillment of the design requirements. Figure 5.12(b) depicts the step response of the motor speed controller in simulation (dashed black line) and in the experiment (solid gray line).

5.3.2 Output torque control design

An outer feedback control loop is closed on the estimation of the load torque, $\hat{\tau}_\mathrm{L}$, coming from the *elastomer coupling model* block. Indicating the desired torque with τ_des, the

Table 5.8: Parameters for the cascade control strategy of the compliant joint drive.

Parameter	Description	Value
k_ω	proportional gain	0.00312
i_ω	integral gain	0.312
k_τ	proportional gain	10
i_τ	integral gain	300
k_p	proportional gain	0.001 ... 200
d_p	derivative gain	0.001 ... 10

[8]From the Maxon Motors catalogue (Maxon Motor AG, 2012) results: max $\dot{\vartheta}_\mathrm{M}$=700 rad/s.

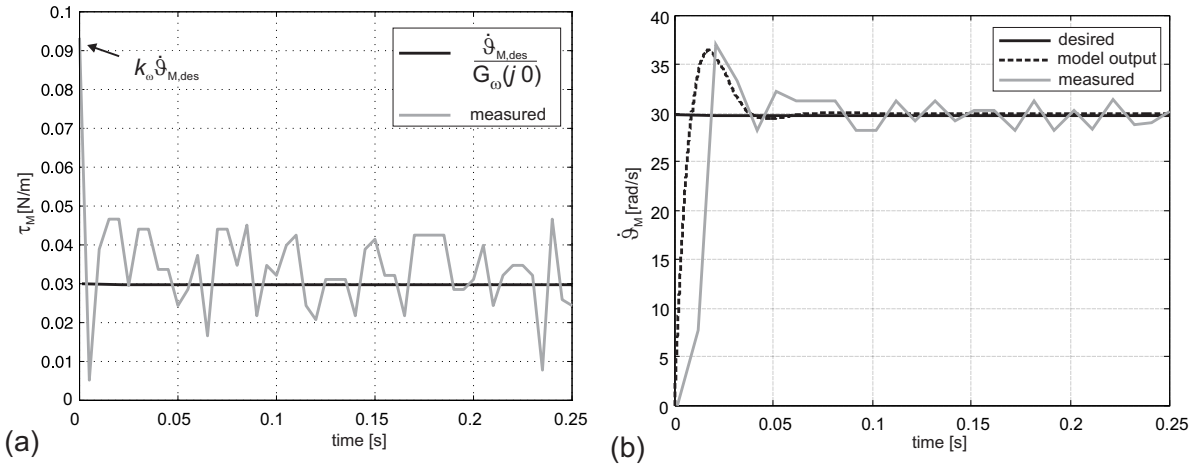

Fig. 5.12: (a) Measured control signal for an input of $\dot{\vartheta}_{\mathrm{M,des}}$=30 rad/s (gray line) and expected steady-state control signal value (black line). At start and at steady-state, the mathematical results are obtained adopting the *Initial and Final Value Theorems*. (b) Step response of the motor speed control loop. The desired speed is depicted in solid black line. Simulated and measured step responses are shown in dashed black and solid gray line, respectively.

torque error is:

$$e_\tau = \tau_{\mathrm{des}} - \hat{\tau}_{\mathrm{L}} \quad .$$

The torque controller is also of PI-type and the t.f. is:

$$C_\tau(s) \;=\; \mathrm{k}_\tau + \frac{\mathrm{i}_\tau}{\mathrm{s}} \;=\; \frac{\mathrm{k}_\tau}{\mathrm{s}}\,(\mathrm{s} + \frac{\mathrm{i}_\tau}{\mathrm{k}_\tau}) \quad . \tag{5.11}$$

The parameters of the controller were selected in order to have a bandwidth around 30 rad/s and for a step response a settling time $t_{\mathrm{s}} \leq 0.5$ s without overshoot. An important condition for the selection of the control parameters was the stability of the closed-loop t.f. $W_\tau(s)$. The seventh order denominator of the t.f. between τ_{des} and $\hat{\tau}_{\mathrm{L}}$ was analyzed and the *Routh-Hurwitz stability criterion* was adopted to check the stability conditions for different torque control parameters. Results show that for a given controller gain k_τ, the stability criterion sets limits on the integral parameter i_τ. A graphical evaluation of the stability conditions is shown for two different sets of parameters (stable and unstable set) with the root locus and the Bode diagram of the open loop t.f. $F_\tau(s)$ in fig. 5.13. The constraint on the settling time turns into a forbidden area in the imaginary plane (light gray area). The stable case is depicted in black. The bandwidth is 27 rad/s and the phase margin is $\varphi_{\mathrm{M}} > 100\,^\circ$. For increasing integral gain, the bandwidth increases but the phase margin reduces till the system reaches the stability limits. The second set of parameters presents the integral part which is double (gray lines). In this case the *Routh-Hurwitz stability criterion* is not satisfied ($\varphi_{\mathrm{M}} < 0\,^\circ$) and the system is unstable. The control parameters corresponding

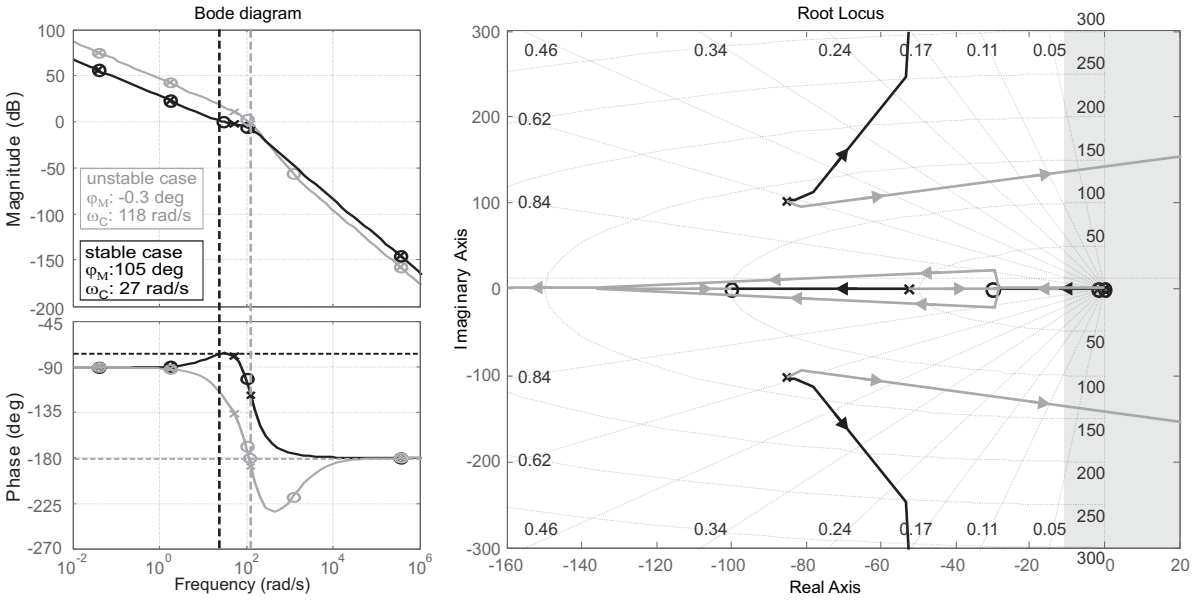

Fig. 5.13: On the left, the Bode plot of the open loop t.f. $F_\tau(s)$ in the stable case (black line) and unstable case (gray line) is depicted. Dashed vertical lines indicate the crossover frequency ω_C in the two cases. Dashed horizontal lines indicate the phase margin ϕ_M. On the right, the corresponding root locus diagram is shown.

to the stable case in the figure, are reported in Table 5.8. In order to separate the dynamic response times between this loop and the inner control loop so that they do not interact with each other, the torque control loop is implemented four times slower than the rotor speed loop.

5.3.3 Output position control

The outermost control loop in the cascade control strategy generates the desired torque, τ_{des}, for the output torque controller. Typically, the outermost controller works on the output shaft position of the drive and therefore is directly related to the interaction of the joint with the environment. Indicating the position error as

$$e_{\text{p}} = \vartheta_{\text{L,des}} - \dot{\vartheta}_{\text{L}}$$

and adopting a PD position controller, the desired torque is:

$$\tau_{\text{des}} \;=\; \text{k}_{\text{p}} \cdot e_{\text{p}} - \text{d}_{\text{p}} \cdot \dot{\vartheta}_{\text{L}} \quad . \tag{5.12}$$

The control parameters can be selected based on a second order mass-spring-damper system. The proportional factor, k_{p}, corresponds to the desired spring stiffness k_{des} and the derivative part, d_{p}, to the desired damping d_{des}. In the interaction of the robot joint

drive with the environment, the controller can be designed to have either fast and stiff responses or slow and compliant behaviors based on the desired requirements. Table 5.8 reports the range of stable values for the two parameters in the controller.

The interaction with the environment can be also controlled with the bio-inspired position/stiffness control strategy as presented in Chapter 4. The generation of activations to the virtual antagonistic muscles allows joint position and stiffness to be independently controlled. The desired torque is a nonlinear function of the muscle lengths, velocities and activations and corresponds to [cmp. to equation (2.13)]:

$$\tau_{\text{des}} = [F_{\text{M},2}(\Delta L_{\text{eff},2}, V_2, a_2(t)) - F_{\text{M},1}(\Delta L_{\text{eff},1}, V_1, a_1(t))]\,\text{r} \quad . \tag{5.13}$$

In either case the position controller is implemented in the microcontroller with a loop time of 6 ms.

Both interaction control approaches guarantee an active control of the mechanical impedance. However, the question does arise as to how the bandwidth of the impedance controller looks like in the two cases. In the following, the mechanical impedance is analyzed first, when the bio-inspired approach is used and then when the PD control approach is adopted.

5.3.4 Mechanical impedance analysis

Real elasticity directly integrated into the joint and the ability to actively control the joint compliance are considered to be the key elements for safe interaction (Albu-Schäffer et al., 2007; Bicchi and Tonietti, 2004). In order to analyze the interaction of the drive with external perturbations, the study has to concentrate on the output mechanical impedance, i.e. the measure of how much the system resists to movements when an external force is acting on it. The analysis of the mechanical impedance is typically performed in the frequency domain and is defined as (Lobontiu, 2010):

$$Z_{\text{L}}(s) = -\left.\frac{T_{\text{L}}}{s \cdot \Theta_{\text{L}}}\right|_{\text{s}=j\omega} \tag{5.14}$$

which states that the impedance magnitude at a certain frequency is provided by the disturbance, normalized by angular displacement and disturbance frequency. Low impedance corresponds to a compliant behavior. High impedance refers to a higher stiffness of the system under perturbation. While for low frequencies an impedance controller can be designed to produce the desired behavior, for high frequencies this ability reduces due to bandwidth limitations.

In this section the objective is to analyze the mechanical impedance and deduce in which frequency range the impedance can be controlled. The intrinsic joint impedance can be evaluated first. In this case it is assumed that the joint is not controlled i.e., the

motor is not powered. Therefore, only the output side equation in system (5.5) has to be considered:

$$-\tau_{\mathrm{L}} = \mathrm{J}_{\mathrm{tot,L,drive}} \cdot \ddot{\vartheta}_{\mathrm{L}} + \tau_{\mathrm{DL}} - \tau_{\mathrm{S}} \quad . \tag{5.15}$$

Using a linear friction model for τ_{DL} and applying the Laplace transform, equation (5.15) becomes:

$$-T_{\mathrm{L}} = \mathrm{J}_{\mathrm{tot,L,drive}} \cdot \mathrm{s}^2 \cdot \Theta_{\mathrm{L}} + \mathrm{d}_{\mathrm{L}} \cdot s \cdot \Theta_{\mathrm{L}} - T_{\mathrm{S}} \quad .$$

Substituting the result above in equation (5.14), the intrinsic joint impedance results

$$Z_{\mathrm{L}}(s) = \frac{\mathrm{J}_{\mathrm{tot,L,drive}} \cdot s^2 \cdot \Theta_{\mathrm{L}} + \mathrm{d}_{\mathrm{L}} \cdot s \cdot \Theta_{\mathrm{L}} - T_{\mathrm{S}}}{s \cdot \Theta_{\mathrm{L}}} \quad .$$

Taking into account equation (5.1) with $\Theta_{\mathrm{S}} = -\Theta_{\mathrm{L}}$ (the motor is assumed to remain steady) the impedance is:

$$Z_{\mathrm{L}}(s) = \left(\mathrm{J}_{\mathrm{tot,L,drive}} \cdot s + \mathrm{d}_{\mathrm{L}} + \frac{ECM(s)}{s} \right) \Bigg|_{\mathrm{s}=j\omega} \quad . \tag{5.16}$$

The joint mechanical impedance exhibited at the output when the motor is not controlled is a combination of three components: output inertia, output friction and elastomer coupling compliance. The friction component does not change with the frequency and therefore its contribution sets limits on the minimal obtainable impedance. The inertia is directly proportional to ω and therefore its contribution increases with the frequency. A high inertia reduces the impedance bandwidth. This result shows how important is to have low inertia and friction. The integrated elasticity limits the high-frequency impedance to its intrinsic stiffness: a very compliant passive element protects the gearbox over a wide frequency range; a stiff one increases the intrinsic impedance but contributes to a higher active control bandwidth (Zinn et al., 2004).

When the motor is controlled, the impedance transfer function is a 8^{th} order system. Instead of examining the poles and zeros of the 8^{th} order t.f., in this thesis, for ease of exposition, it has been preferred to estimate the obtainable impedance range in simulation adopting Matlab/Simulink. With this objective, the cascade control strategy and the model of the joint drive were implemented in Simulink. Following the definition of impedance, in the simulation, the load torque is set as input and the joint speed as output. The impedance range is evaluated both for the bio-inspired strategy and for the PD control strategy.

Figure 5.14(a) depicts the impedance range obtained when the bio-inspired control strategy is adopted for the control of the compliant joint drive (dark gray area). The minimum impedance is determined by the friction load. The maximum impedance is obtained for maximum co-activation. A higher impedance would be achieved adopting higher maximum muscle forces and removing the torque saturation. The light gray area shows the impedance range that would be obtained if the drive system with its friction,

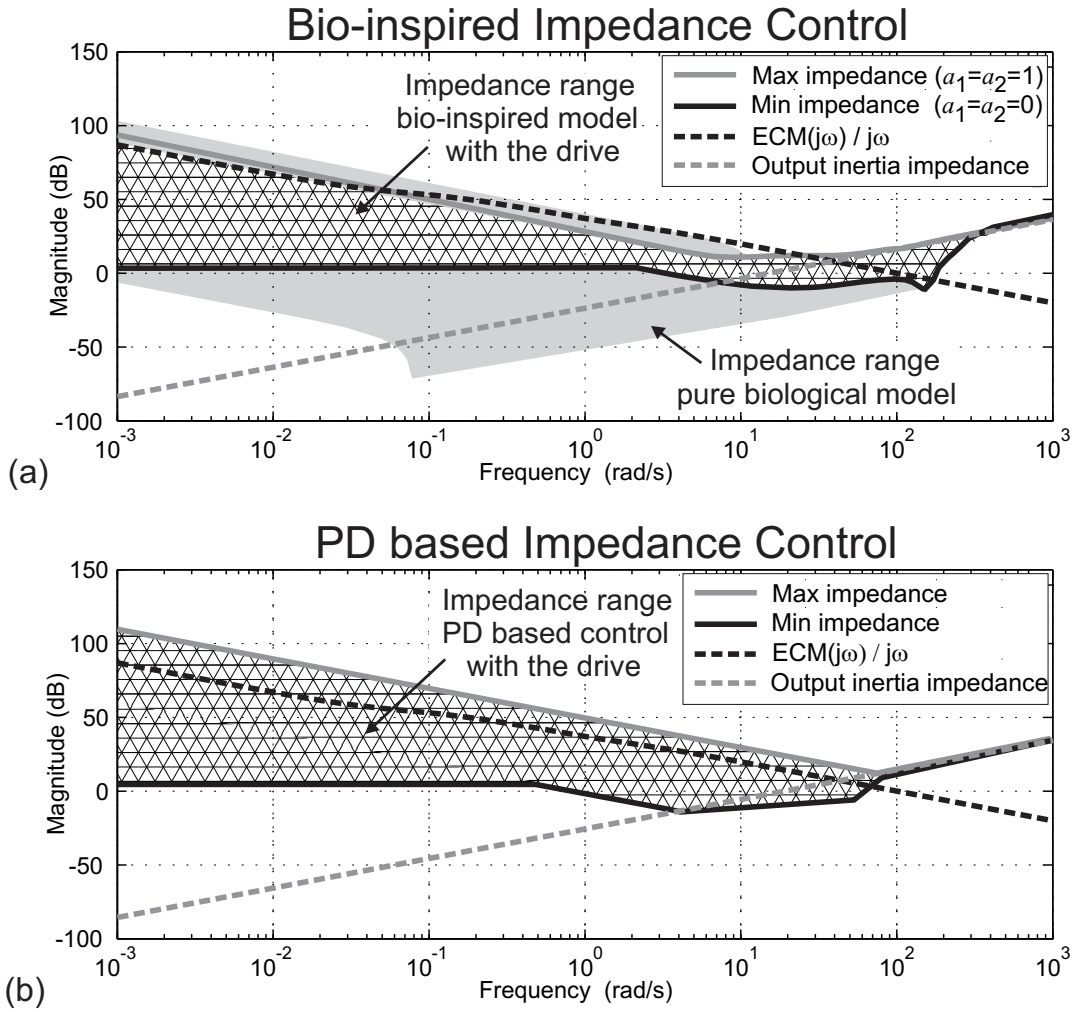

Fig. 5.14: (a) The area filled with triangles indicates the obtainable impedance range when the bio-inspired control strategy is adopted as outermost control loop of the compliant joint drive. The gray area shows the impedance range obtained in simulation with the model of the human elbow joint without the drive. (b) The area filled with triangles indicates the obtainable impedance range when the PD position control approach is adopted to control the joint impedance.

inertia and control delays was not present.
Figure 5.14(b) shows the achievable impedance range (dark gray area) when the PD position control strategy is adopted. The impedance behavior can be modulated by changing the controller parameters k_p and d_p. The minimum impedance is limited by the friction load. The maximum impedance is achieved in correspondence of the highest k_p for which the system remains stable. For low frequencies the actuator is able to generate the desired stiffness. For higher frequencies the impedance matches the output inertia (gray dashed line).

The PD based approach reaches a *Max impedance* higher than that using the *Bio-inspired* strategy till 60 rad/s. The impedance controlled with the *Bio-inspired* strategy is controllable till 300 rad/s. The minimum impedance is comparable. In both diagrams, the impedance of the integrated elastomer coupling is depicted as black dashed line. It can be shown that as long as the generated impedance lies below the elastomer coupling impedance, the system is passive and therefore stable[9] (Vallery et al., 2007). This means that if passivity is desired, the robotics joint drive should not produce a stiffness higher than that integrated (passive elastic element). According to this result, a very stiff elastic element should be favored. However, as discussed above, a more compliant element would ensure a safer interaction. This result shows how the choice of the elastic element is always a trade-off.

5.4 Experimental results

This section shows the experimental results obtained by adopting first the PD position control strategy for the interaction of the lever arm with external forces, and then the results in the case the interaction is controlled based on a bio-inspired simultaneous control of position and stiffness. In all the experiments, a user generates the disturbances on the lever arm [see fig. 5.15].

5.4.1 PD position control (as reference)

A classical PD position control is implemented on the technical joint drive to evaluate its interaction performances and will be used as reference to compare its results with the bio-inspired approach. In this case the modulation of the impedance is realized by changing the control parameters.
Three experimental tests have been realized. Figure 5.16 shows the experimental results when the system is not disturbed and it is commanded to track an alternating desired position. At start k_p is set to 10, which corresponds to a very compliant system. At t=5 s, k_p is increased to 100 (gray background). The damping parameter k_d is set to 0.1. The top of the figure shows the desired torque obtained as output from the PD control scheme (dashed gray line) and the estimated load torque at the joint (solid black line). On the bottom of the figure, the position results are shown. For low stiffness and for every alternating desired positions, the torque reaches the desired one with a long transitory and the arm goes slowly to the desired alternating positions. For high stiffness the torque saturation (at ± 8 Nm) is reached, which reduces the response time.

[9] An important characteristic of passive systems is that they are phase bounded, i.e. the phase shift is always within (-90, 90.). The phase shift of a stable SISO passive system in response to a sinusoidal input is always within [-90, 90]. As long as the generated impedance lies below the elastomer coupling impedance, the phase of the impedance frequency response has values within (-90, 90)

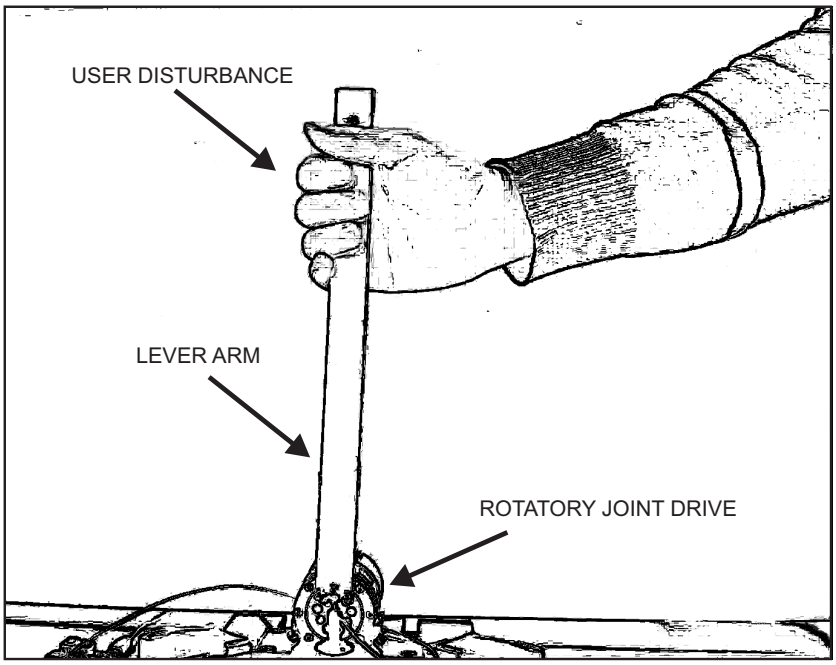

Fig. 5.15: Hand-drawn sketch of the rotatory robotics joint drive with a lever arm and a user interacting with it. In order to test the control schemes presented in this thesis, the user generates disturbances at the lever. The drive is controlled to display a desired stiffness while keeping a certain joint position.

Nevertheless, the system reacts faster in torque and the desired alternating positions are also reached faster.

In fig. 5.17 the situation is shown in which the lever arm tracks a constant desired position $\vartheta_{\mathrm{L,des}}$=-0.3 rad while a low frequency disturbance is applied to the lever. At start the lever is compliant. At t=5 s the proportional parameter becomes higher and the system performs stiffer: although higher load torque is applied, the lever arm keeps the desired position.

In the experimental results shown in fig. 5.18, the system is subject to high frequency disturbances. At start (low k_p), the control bandwidth is too low and the output inertia dominates the system behavior [cmp. fig. 5.14(b)]. For higher k_p, the control bandwidth increases and the system exhibits the desired stiff behavior (the lever is slightly perturbed).

5.4.2 Bio-inspired interaction control

In this section the experimental results of a concurrent control of position and stiffness adopting the bio-inspired control approach acting on two antagonistic virtual muscles and working in combination with the technical joint drive is analyzed. Four different

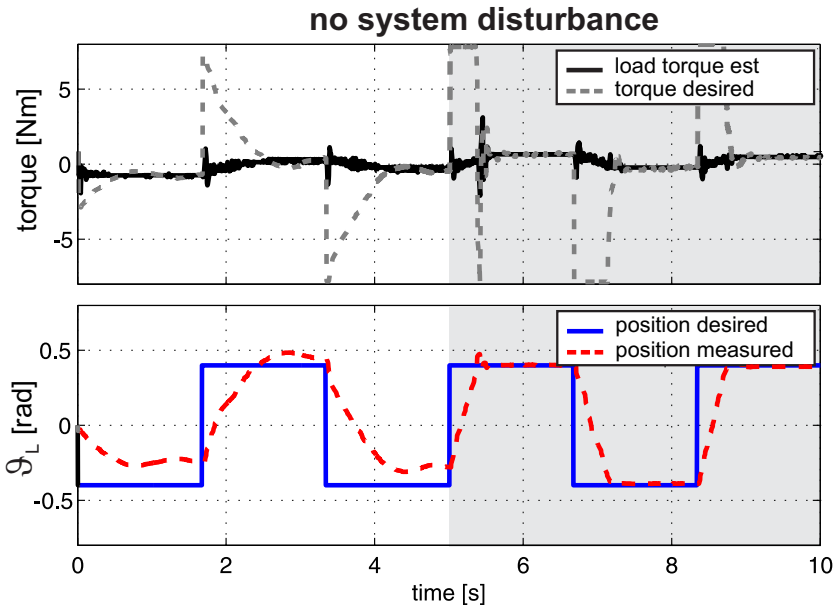

Fig. 5.16: Experimental results adopting the PD position control in absence of external disturbances. At start k_p=10. At t=5 s the proportional parameter is increased to k_p=100 (gray background). The torque controller behavior is depicted on the top of the figure. On the bottom are shown the desired and measured joint positions.

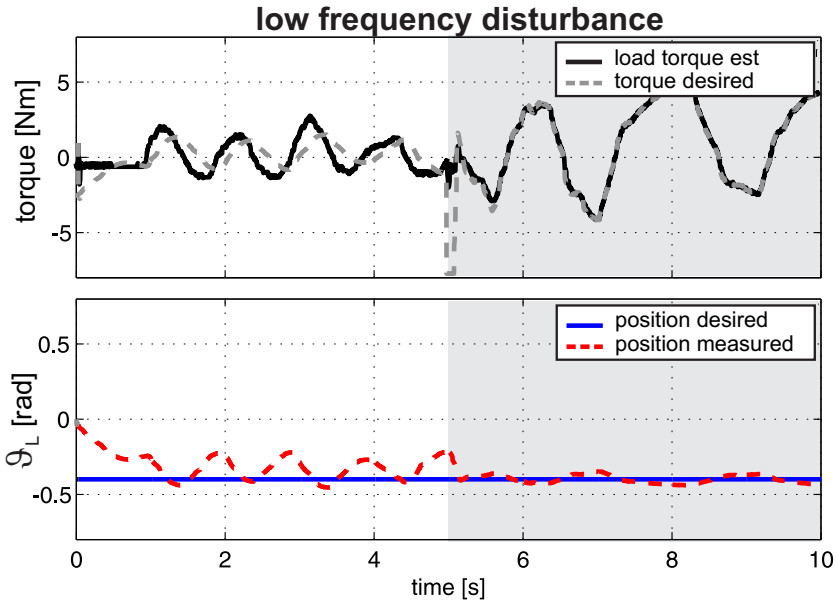

Fig. 5.17: Experimental results adopting the PD position control in presence of a low frequency disturbance applied at the lever arm. At start k_p=10. At t=5 s the proportional parameter is increased to k_p=100 (gray background).

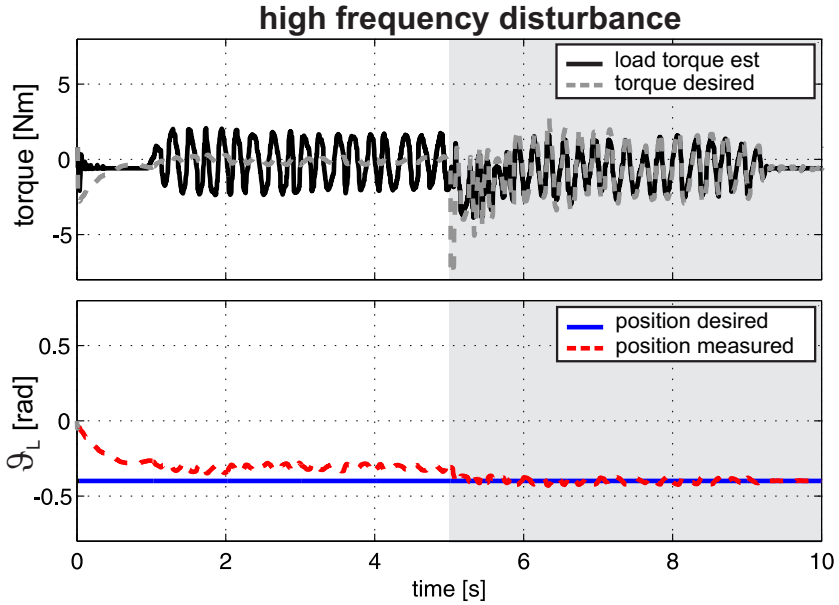

Fig. 5.18: Experimental results adopting the PD position control for a high frequency disturbance applied at the lever arm. At start k_p=10. At t=5 s the proportional parameter is increased to k_p=100 (gray background).

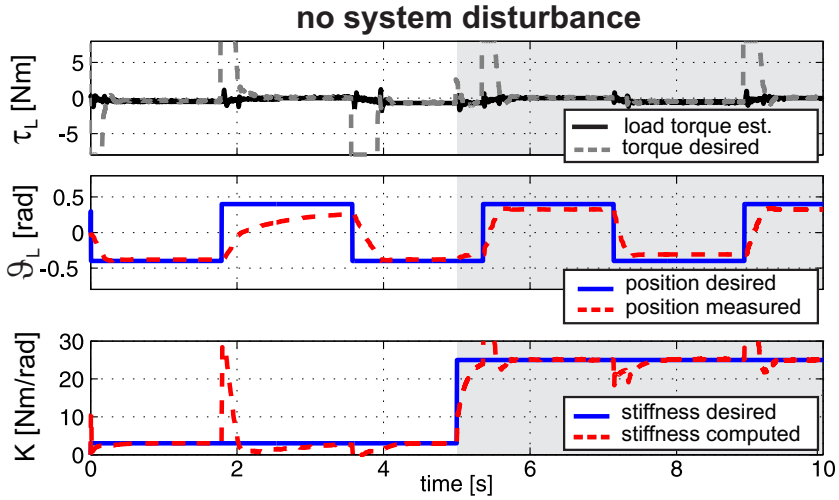

Fig. 5.19: Experimental results adopting the bio-inspired position/stiffness control when the system is required to track a desired alternating step position and no external disturbances are applied at the joint. At start the desired stiffness is 3 Nm/rad. At t=5 s it turns to 25 Nm/rad (gray background).

experimental situations are evaluated. It will be shown that the experimental results are comparable with the simulation results shown in fig. 4.9.

Figure 5.19 shows the first experiment. Like in fig. 5.16, the desired stiffness at start

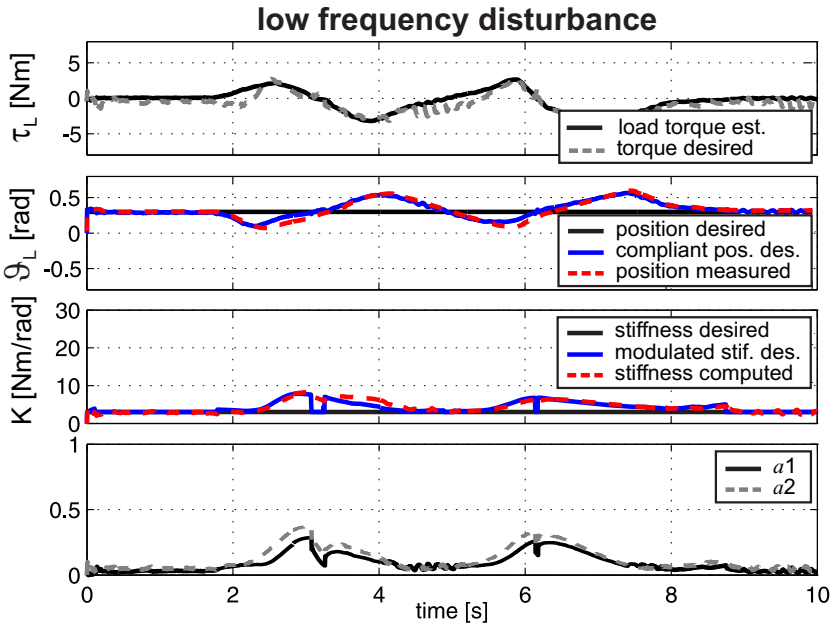

Fig. 5.20: Experimental results adopting the bio-inspired position/stiffness control approach for a low frequency disturbance applied to the arm. The system reacts elastically and follows the desired compliant position.

is low (k_{des}=3 Nm); at t=5 s it increases (k_{des}=25 Nm). The lever arm is required to track a desired alternating position $\vartheta_{L,des}$ of magnitude -0.4 rad and 0.4 rad. No disturbances are applied at the extremity of the lever arm. For low desired stiffness, the desired position $\vartheta_{L,des}$=-0.4 rad is reached successfully while position $\vartheta_{L,des}$=0.4 rad cannot be reached. The asymmetric behavior in -0.4 rad and 0.4 rad is a consequence of the non-symmetric stiffness–joint angle characteristic (see fig. 2.7). At t=5 s, the desired stiffness increases. The system successfully reaches both desired position and stiffness and the lever reacts faster in position. The behavior here is similar to the one obtained with the PD-control approach (cmp. fig. 5.16).

In the following experiments, the interaction behavior of the robotics joint drive for different disturbances will be shown. The main difference with the PD control schema proposed above is that the bio-inspired approach is able to adapt its behavior according to the disturbance: The control system regulates the position and, in dependence of the perturbation frequency, adapts the joint impedance automatically.

Like in the simulation test of Section 4.3, in these experiments, a low constant desired stiffness (k_{des}=3 Nm) is considered.

In fig. 5.20 low frequency perturbations are applied to the extremity of the lever and the desired position is modified (compliant desired position: $\alpha_{des}+\Delta\alpha$, cmp. fig. 4.7) such that the link follows the trajectory imposed by the external load. As the position error increases due to the applied load, the adaptive block (of the bio-inspired control) increases the desired stiffness as long as the error remains high. When the error reduces,

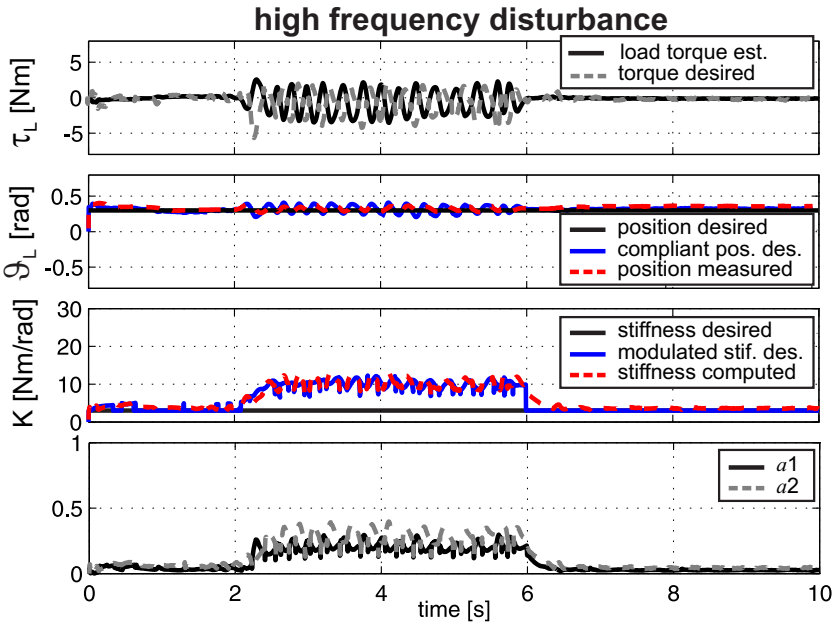

Fig. 5.21: Experimental results adopting the bio-inspired position/stiffness control approach for high frequency disturbances applied at the lever arm. The desired stiffness automatically increases thus reducing the compliance of the system with respect to the load.

the stiffness decreases back to the desired value. The same behavior was obtained in simulation [see fig. 4.9 (low frequency load)].

Figure 5.21 shows the results for high frequency perturbations. The adaptive control, acting on the stiffness set-point, automatically modulates the desired impedance: it makes sure that the desired stiffness increases thus providing higher stability to the joint and reducing the disturbance effects. In this case too, the obtained result is in line with the simulation [see fig. 4.9 (high frequency load)]. Humans show the same behavior as we increase voluntary muscle activation to move faster or to move against a load (Milner, 1993). Therefore, the bio-inspired control mechanism is able to regulate the position and, in dependence of the perturbation frequency, simultaneously adapt the joint impedance. For rapid perturbations, stiffness increases thus reducing the effect of the external torque on the lever. For low frequency perturbations, the joint is compliant.

Figure 5.22 depicts the test results when impulsive disturbances are applied at the lever arm. Also in this case, desired joint stiffness increases when the disturbance is applied thus producing a stabilizing effect for the link [compare with fig. 4.9 (impulsive load)].

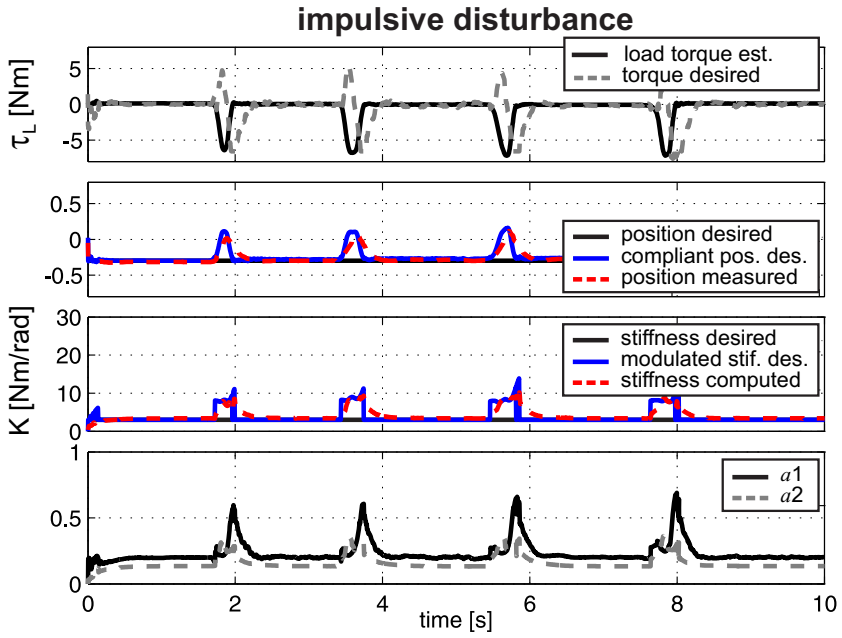

Fig. 5.22: Experimental results of the bio-inspired position/stiffness control approach for impulsive disturbances. The system reacts elastically and automatically increases the desired stiffness thus providing the joint with higher stability.

5.5 Summary

A lightweight, intrinsically compliant rotatory joint drive was adopted in this chapter to validate the bio-inspired control scheme introduced in Chapter 4. Besides the lightweight construction, the novelty of the drive lies is the integration into the joint of a sensorized elastomer between the gearbox and the output link. An absolute rotary position encoder is incorporated into the coupling and used to measure its torsion when an external load is applied. This measurement can be supplied to its model to have an estimation of the load torque which, in turn, can be used to implement a torque control scheme. The complete compliant robotics drive was described as a two-mass model (Section 5.1) and a system identification approach was pursued to obtain the values of the mechanical model parameters (Section 5.2). A cascade speed-torque control scheme for the drive was designed in Section 5.3. To control the joint drive interaction with the environment, either a classical PD position controller or the bio-inspired strategy as proposed in Section 4.2 could be adopted. Experimental results for both control schemes were reported in Section 5.4 under different perturbation conditions. Results showed that stiff and compliant interactions could be generated for different external perturbations. Due to the selection of maximum muscle forces, the maximum impedance with the bio-inspired control approach was lower than that achieved with the PD strategy. Nevertheless, in order to have an intrinsically stable system, the generated impedance has to lie below the elastomer coupling impedance (passivity property). Assuming this

condition, a comparison of the impedance ranges (fig. 5.14) showed that the two ranges are comparable for frequencies up to 60 rad/s. Furthermore, the joint drive controlled with the bio-inspired scheme was able to reach the desired position and automatically adapt joint compliance according to the disturbance like humans do.

Chapter 6

Discussion

In the coming years, the interaction of robots with humans, especially in collaborative and co-work operations, is expected to grow. Also in social applications ranging from elderly care to entertainment, the use of robotic arms is increasingly likely foreseeable. Furthermore, the construction of robotics devices in fields like prosthetics and orthotics is expanding too. In all these applications, the robots are required to interact with an unknown environment. Safe behavior is the most important feature during interaction (Groothuis et al., 2013). This basically means to protect the robot as well as its environment in case of collisions. It goes without saying that stiff systems or robots in which the control implementation presents limitations such as instability or physical failure, cannot be adopted for the interaction with an unknown environment.
In this thesis, it was investigated the design, test and validation of biologically inspired control concepts for robotics applications interacting with unknown environments. The achievements, possible limitations, and possible future works are summarized in the following sections.

6.1 Bio-inspired control achievements

The objective of this work was to control a compliant rotatory joint drive for orthotics and prosthetics applications thus reproducing the human arm behavior. Starting from Hogan's claim (Hogan, 1984), for which co-activation of antagonistic muscles is used by the CNS to adapt the mechanical impedance at the joint, we designed and implemented the active control of the mechanical impedance on a lightweight, inherently compliant actuator, adopting bio-inspired control concepts like antagonistic muscle co-activation and reciprocal activation.

The CNS-like control laws were designed based on physiological models and properties of biological systems. Virtual antagonistic muscles based on the Hill-type model and a simplified pulley joint geometry were adopted for the design of the antagonistic musculoskeletal setup resembling the human elbow joint. Muscle and joint parameters for the model were adopted based on real measurements.
The level of abstraction pursued in this thesis for the modeling design, corresponded to a reasonable compromise between biological details and simplified mechanism and it

allowed to examine physiologically control strategies in simulation for position control and compliance regulation.

Our simulation results suggest that the bio-inspired control scheme is able to successfully regulate joint position and compliance simultaneously in an antagonistically actuated joint setup. Additionally, the control of compliance is achieved through stiffness adaptation for different external perturbations and ensures stability.

The technical actuator adopted for the experiments integrates passive elasticity in form of a sensorized elastomer coupling, which provides intrinsical compliance at the joint and the ability to attenuate shocks due to unexpected impacts.

In order to reach a bio-equivalent behavior, the actuator that was actually used in the experiments was completely hidden to the impedance control process by canceling out the drive specific dynamic effects, thus equipping the joint with the intended muscle dynamics.

The bio-inspired controlled drive was tested for different load situations. Experimental outcomes confirmed the results obtained in simulation. The system successfully reaches the desired position while modulating the impedance. Furthermore, as long as the rendered impedance lies below the intrinsic stiffness of the pure elastomer coupling, the system is stable due to its passivity properties.

The results of this work can be compared to the findings obtained by Yang et al. (2011). Important differences lie in the implementation of the muscle models, the computation of joint stiffness and the resulting control scheme with adaptive modulation of joint impedance. Furthermore, our findings are based on the expression of the stiffness produced by antagonistic muscles driving a hinge joint and on the intrinsic properties determined by the nonlinear spring-like behavior of muscles.

6.2 Musculoskeletal model and its limitations

The model of the human elbow presented in this thesis is composed by two antagonistic muscles and a joint geometry. For the design of such a musculoskeletal setup, some assumptions have been made which are addressed in the following.
Each muscle was implemented adopting the Hill-type muscle model. In this model, the active force-length relation was approximated with a quadratic function which allowed a closed mathematical description of the stiffness at the joint. The quadratic approximation is inadequate if elongation of fibers above 130% of their optimum length occurs (Woittiez et al., 1984). Nevertheless, it was shown in Section 2.3.1 that the simplified expressions as used for the stiffness computation in this work can be easily replaced by Gaussian relations without loss of the stiffness characteristics and controllers abilities discussed here (Annunziata et al., 2010). Alternatively, the Gaussian representation could be approximated more closely e.g. by using splines or piecewise linear functions

which, however, would increase the number of cases in the mathematical description of regions, node positions etc. (Section 2.3.3).

The muscle model used in this thesis does not include the contribution of tendon compliance. In fact, it is assumed that the tendon is a serial elastic element of high stiffness. Certainly, as it was shown in Section 2.3.5, the introduction of a compliant tendon increases the stiffness range for increasing co-activation. However, properties and results discussed in this work like stiffness nodes and regions of low stiffness variation are still valid.

The muscle was modeled as a force generator which produces a force according to its level of activation. If integrated into a joint setup within a skeletal configuration, the muscle force acts on the joint as a torque via an effective lever arm. The joint configuration can have different levels of complexity regarding the changes of the effective lever arms. In this study, the angle-dependent variations of the lever arm were neglected which was equivalent to the introduction of a hinge joint with a pulley (Section 2.1.2).

Aside from the derivation of the joint stiffness in a closed form, the simplification assumptions discussed above allowed to simplify the stiffness analysis. This achievement played a crucial role for the evaluation of the stability issues discussed in Section 4.1 as well as for the implementation of the stiffness control loop according to actual muscle activations, joint position and velocity, shown in Chapter 3 and Chapter 4.

6.3 Implications of stiffness node analysis

Co-activation of antagonistic muscles pulling at a joint, allow, in general, the ability to change the joint stiffness. Nevertheless, it was shown in Section 2.3 that depending on the parameters of the joint and muscles, joint positions can be found for which the stiffness can not be changed (stiffness nodes). In that study, parameters were selected on purpose to illustrate the problem and show that situations can be generated for which stiffness nodes occur. On the way to finding real biological examples in which stiffness nodes exist, in this section, the femoral-tibia (FT) joint of a locust adopting real biological data is investigated. It will be shown that when the antagonistic muscles are co-activated, a stiffness node occurs in the main working range.

Figure 6.1(a) depicts a FT joint. The lines connecting the muscles to the skeletal apparatus represent the extensor (top) and flexor (bottom) tendons. The flexor tendon rides on top of a lump. The dark gray stick in the middle represents the femur. As the joint rotates, the extensor and flexor remain parallel to each other and the femur. The moment arms vary as a function of the joint angle α. The musculoskeletal parameters adopted for the stiffness analysis are taken from measured data as reported by Zakotnik et al. (2006) and derived by Heitler (1974). The main operating FT joint range of motion is approximately [-1,1] rad. Figure 6.1(b) shows the stiffness at the FT joint when the antagonistic muscles are co-activated plotted over the main joint range of motion.

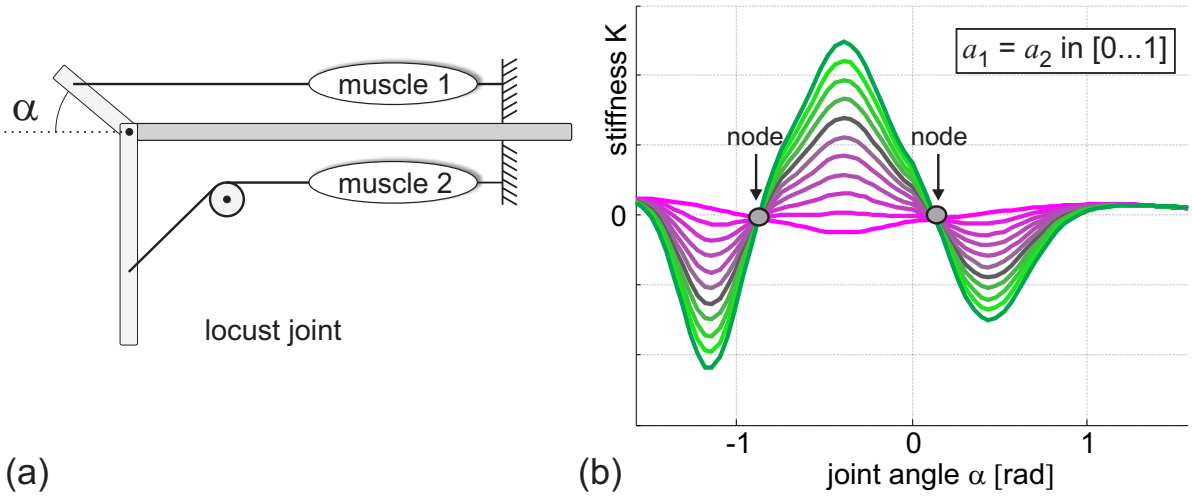

Fig. 6.1: (a) Locust femoral-tibia joint. (b) Joint stiffness plotted against the joint angle adopting the locust joint geometry as in (a) and for perfect co-activation. Highest co-activation is depicted in green. For two joint angles stiffness nodes occur.

Two stiffness nodes occur. While the stiffness node at α=-0.87 rad is almost at the extremity of the joint working range thus not influencing the locust operation, the other node, at α=0.13 rad, is almost in the middle of the joint working range. Between the two nodes, the stiffness increases for increasing co-activation (in green is depicted the stiffness for highest co-activation).
It has to be investigated if reflexes serve as compensation mechanisms for stiffness nodes or if stiffness nodes are integrated in the movement strategies of animals instead. For instance, simulations using the locust joint geometry and recorded data during aimed limb movements, such as reaching and grooming (Zakotnik et al., 2006), have shown that, while during unloaded cases the FT joint angle crosses the angular value for which the stiffness node occurs, in the loaded case, in which stiffness variability is required, the locust movement is such that the FT joint angle is confined between the two nodes thus taking advantage of full stiffness range variability.
In addition to reflexes, friction and damping effects due to connective tissue also influence the force and movement generation in biological systems. Especially in insects, passive joint damping can dominate the overall movement capabilities (Garcia et al., 2000; Zakotnik et al., 2006) up to a complete maintenance of a given body posture without muscle activation. These bio-mechanical factors, however, could only impair the active change of joint stiffness if they were – at least partly – depending on muscle activation, e.g. stiffness change due to muscle bulging.

6.4 Implications of a multi-muscle setup

It was shown that stiffness variability of muscle-driven antagonistic hinge joints is associated with co-contraction. This ability, however, if combined with a torque controller, could be limited due to the occurrence of stiffness nodes. Since the generation of torque and stiffness is always coupled for joints with only two antagonistic muscles, additional degrees of freedom must be added to decouple the control of torque and stiffness. Therefore, two more antagonistic muscles were added to the setup. Though, even without stiffness nodes, muscle and joint configurations exist which allow only small variations of stiffness across the working range (Section 3.2.1). This led to the more general question what an optimal joint setup based on four muscles would have to look like to maximize the stiffness variability across a defined working range. To answer this question, a brute-force optimization algorithm was run in Section 3.3. The goal of this optimization was to seek a musculoskeletal setup able to generate high stiffness variability in a certain angular region and a defined torque range. Optimization results showed that out of the four muscles, two short antagonistic muscles and two long antagonistic muscles satisfied the requirements. The short muscles, due to their increased slope of the torque curve, which results in a big change of stiffness for activation changes, can be related to the stiffness control while the long muscles to the torque control. Based on this optimal setup, different control approaches were tested and compared to the maximal and minimal stiffness that could be reached in principle by a perfect controller. The introduction of an overflow strategy could vastly increase the performance of a very basic torque and co-activation based stiffness controller combination. This combined control approach exceeds even the results of an inverse model controller. However, by joining the simple stiffness and torque controllers with the inverse model and overflow strategies, the response time could be decreased due to the feed-forward nature of the inverse model.

In biological systems, joints are often driven by more than two muscles. It can be assumed that controllers in the nervous system have to cope both with the actuator redundancy and with the nonlinear muscle dynamics. Therefore, in a bio-mimetic transfer to technical systems the implementation of multi-muscle configurations seems to be advisable.

The four-muscle setup as used in this study for an optimal stiffness variation over a defined joint angular and torque range as well as for concurrent prevention of stiffness nodes, could be implemented following different strategies. One strategy is to generate the net-torque of all muscles by means of a single technical actuator as it was proposed in Chapter 5. In this case, muscles would be emulated within the controller framework of the actuator. Another strategy could aim at merging subgroups of muscles (e.g. the long muscles) in a shared actuator which for example could make use of a push-pull mode if suitable. This approach however, would decrease the level of independence gained through the proposed optimal setup with several muscles.

6.5 Implications of the stability analysis for the muscle-driven hinge joint

The adaptive tuning of impedance parameters subject to unknown dynamically changing environments is an important research topic in the robotics community. Biological systems, physically interacting with environments, simultaneously control impedance and movement during the interaction. This hypothesis is the basis for the stiffness modulation scheme and adaptive approach as presented in this work. Compared to impedance learning strategies (Kadiallah et al., 2012), in which algorithms are implemented with the objective to learn to perform a certain task, impedance adaptation schemes have some advantages although might be more difficult to implement. The main advantage lies in the fact that the robot does not need to repeat the operation in order to learn what is the desired impedance. Though, the difficulty is in the development of an adaptive algorithm which is based on a variable acting as a measure of the interaction performance. In most cases the selection of such variable is difficult, especially in the case of dynamically changing environments.

The stability analysis performed through simulations (Section 4.1) showed that, even for a stable equilibrium, the co-activation level affects the reaction of the joint to external perturbations in terms of oscillations and settling time. This concept leads to the more general question what an optimal joint stiffness should be with respect to different external task conditions. With the objective to modulate joint compliance with respect to unknown external perturbations, in this thesis, a stability measure based on the position error was adopted for the implementation of the adaptive block in the stiffness control scheme (Section 4.2.3).

Adaptation of joint stiffness during perturbations made sure that the system was able to counter-act external forces, keep its stability and reduce the perturbing effects on the joint. For low frequency perturbations the joint is compliant, while for rapid perturbations stiffness increases so as reducing the unstabilizing effect of the external torque on the lever. This result is in line with the human behavior as it was shown that humans stiffen the joint to increase stability, to move faster or to move against a load (Milner, 1993; Suzuki et al., 2001).

6.6 Advantages for other research and future work

In this thesis different aspects of control theory as well as biology have been presented. Each of these aspects might induce further research in both the design of control concepts and in the biological field.

The first interesting aspect that would be nice to further analyze concerns the occurrence of stiffness nodes in biological systems. It can be expected that animals have not

optimized their stiffness variability across the full working range of a joint but rather specialized their joint dynamics to specific tasks as it was discussed in Section 6.3.

A closely related aspect is that of the optimization approach to reach an optimal musculoskeletal joint setup and a node free joint range of motion (Section 3.3). The simple optimization approach shown in this study could also be used to adjust the working range to that of a certain biological example if necessary. The performance of the control approaches of this study could then be compared with the performance of the animal.

Besides for physiological research, the control schemes presented in this thesis are relevant for technical actuation if nonlinear, antagonistically acting, compliant actuators are used for joint control. This might for example be the case in limb actuation with pneumatic, McKibben or fluidic muscles (Boblan et al., 2004; Sardellitti et al., 2010). In such systems – for example in an arm setup – the occurrence of stiffness nodes at those joint positions where object interactions or collisions occur would enforce one specific stiffness which could be unpleasantly high. The conditions for the existence of stiffness nodes and their position in the main working range are associated with muscle activation, which for pneumatic muscles would correspond to the input pressure to the actuators.

Solutions to the stiffness nodes problem have been proposed in Chapter 3. A node controller, able to manipulate the muscle activations and thus shift the stiffness nodes was designed in Section 3.2.3. With this controller, it is possible to reach a desired stiffness and a desired torque simultaneously for situations in which a pure co-activation approach fails due to stiffness nodes. Besides the node controller, also a suitable choice of muscle length and other joint parameters can be used to constrain the occurrence of stiffness nodes (Section 3.3).

A further aspect is that in the future, the use of bio-inspired control approaches could be advantageous not only to make human-machine interaction safer but also to make it more intuitive; for example, applications which combine technical and biological systems in fields like prosthetics and orthotics may take advantage of the control schemes modeled in this thesis thanks to the mutual embodiment of *drive oriented* control signals and *user oriented* biological commands. Also in these cases, a bio-equivalent actuation system is desirable which presumably would have to cope with inadequate stiffness regulation due to nodes.

Bibliography

Albu-Schäffer, A., Ott, C., and Hirzinger, G. (2007). A unified passivity based control framework for position, torque and impedance control of flexible joint robots. *The International Journal of Robotics Research*, 26(1):23–39. 5, 104

Alexander, R. M. (1988). *Elastic Mechanisms in Animal Movement*. Cambridge: Cambridge University Press. 36

Annunziata, S., Paskarbeit, J., and Schneider, A. (2010). Concurrent torque and stiffness control in an antagonistically actuated hinge joint is impaired by stiffness nodes. In *Proceedings of the 1st International Conference on Applied Bionics and Biomechanics (ICABB 2010)*. 3, 116

Annunziata, S., Paskarbeit, J., and Schneider, A. (2011). Novel bioinspired control approaches to increase the stiffness variability in multi-muscle driven joints. *Bioinspiration & Biomimetics*, 6(4). 045003. 3, 41

Annunziata, S. and Schneider, A. (2012). Physiologically based control laws featuring antagonistic muscle co-activation for stable compliant joint drives. *Applied Bionics and Biomechanics*, 9(3):249–266. 3, 70

Bayo, E. (1987). A finite element approach to control the end-point motion of a single link flexible robot. *Journal of Robotic Systems*, 4(1):63–75. 62

Bennett, D., Hollerbach, J., Xu, Y., and Hunter, I. (1992). Time-varying stiffness of human elbow joint during cyclic voluntary movement. *Experimental Brain Research*, 88:433–442. 18, 19

Bicchi, A. and Tonietti, G. (2004). Fast and soft arm tactics: Dealing with the safety-performance trade-off in robot arms design and control. *IEEE Robotics and Automation Magazine*, 11(2):22–33. 85, 104

Boblan, I., Bannasch, R., Schwenk, H., Prietzel, F., Miertsch, L., and Schulz, A. (2004). A human-like robot hand and arm with fluidic muscles: Biologically inspired construction and functionality. In Iida, F., Pfeifer, R., Steels, L., and Kuniyoshi, Y., editors, *Embodied Artificial Intelligence*, volume 3139 of *Lecture Notes in Computer Science*, pages 160–179. Springer Berlin Heidelberg. 121

Buchanan, T. S., Lloyd, D. G., Manal, K., and Besier, T. F. (2004). Neuromusculoskeletal modeling: estimation of muscle forces and joint moments and movements from measurements of neural command. *J Appl Biomech.*, 20(4):367–395. 13

Burdet, E., Tee, K. P., Mareels, I., Milner, T. E., Chew, C. M., Franklin, D. W., Osu, R., and Kawato, M. (2006). Stability and motor adaptation in human arm movements. *Biological Cybernetics*, 94(1):20–32. 8, 79

Burkholder, T. J. and Lieber, R. L. (2001). Sarcomere length operating range of vertebrate muscles during movement. *The Journal of Experimental Biology*, 204(9):1529–1536. 14, 22, 36

Carter, R., Crago, P., and Gorman, P. (1993). Nonlinear stretch reflex interaction during cocontraction. *Journal of Neurophysiology*, 69(3):943–952. 21

Cheung, E. and Lumelsky, V. J. (1989). Proximity sensing in robot manipulator motion planning: system and implementation issues. *Robotics and Automation, IEEE Transactions on*, 5(6):740–751. 4

Chiaverini, S., Siciliano, B., and Villani, L. (1999). A survey of robot interaction control schemes with experimental comparison. *Mechatronics, IEEE/ASME Transactions on*, 4(3):273–285. 4, 96

Chou, P. C. and Hannaford, B. (1997). Study of human forearm posture maintenance with a physiologically based robotic arm and spinal level neural controller. *Biological Cybernetics*, 76(4):285–298. 8, 70, 80

Coleman, T. F. and Li, Y. (1992). On the convergence of reflective newton methods for large-scale nonlinear minimization subject to bounds. Technical report, Ithaca, NY, USA. 56

Crisp, J. D. C. (1972). Properties of tendon and skin. In Fung, Y. C., Perrone, N., and Anliker, M., editors, *Biomechanics: Its Foundations and Objectives*, pages 141–179. Prentice-Hall, Englewood Cliffs NJ. 22, 36

Cui, L., Perreault, E. J., Maas, H., and Sandercock, T. (2008). Modeling short-range stiffness of feline lower hindlimb muscles. *Journal of Biomechanics*, 41(9):1945–1952. 22

Daerden, F. and Lefeber, D. (2001). The concept and design of pleated pneumatic artificial muscles. *International Journal of Fluid Power*, 2(3):41–50. 6

Feldman, A. G. (1980). Superposition of motor programs–II. Rapid forearm flexion in man. *Neuroscience*, 5(1):91–95. 21

Feldman, A. G. (2008). Threshold position control signifies a common spatial frame of reference for motor action and kinesthesia. *Brain Research Bulletin*, 75(5):497–499. 12

Franklin, D. W., Burdet, E., Tee, K. P., Osu, R., Chew, C.-M., Milner, T. E., and Kawato, M. (2008). CNS learns stable, accurate, and efficient movements using a simple algorithm. *Journal of Neuroscience*, 28(44):11165–11173. iii, 1, 9, 21

Garcia, M., Kuo, A., Peattie, A., Wang, P., and Full, R. (2000). Damping and size: Insights and biological inspiration. In *Proceedings of the First International Symposium on Adaptive Motion of Animals and Machines*, Montreal, Canada. 118

Geyer, H., Seyfarth, A., and Blickhan, R. (2003). Positive force feedback in bouncing gaits? *Proceedings of the Royal Society of London Series B-Biological Sciences*, 270(1529):2173–2183. 12, 13, 14

Giesl, P., Meisel, D., Scheurle, J., and Wagner, H. (2004). Stability analysis of the elbow with a load. *Journal of Theoretical Biology*, 228(1):115–125. 70

Giesl, P. and Wagner, H. (2007). Lyapunov function and the basin of attraction for a single-joint muscle-skeletal model. *Journal of Mathematical Biology*, 54(4):453–464. 70

Graham, B. P. and Redman, S. J. (1993). Dynamic behaviour of a model of the muscle stretch reflex. *Neural Networks*, 6(7):947–962. 76

Gribble, P. L., Mullin, L. I., Cothros, N., and Mattar, A. (2003). Role of cocontraction in arm movement accuracy. *Journal of Neurophysiology*, 89(5):2396–2405. 8, 21

Gribble, P. L., Ostry, D. J., Sanguineti, V., and Laboissière, R. (1998). Are complex control signals required for human arm movement? *Journal of Neurophysiology*, 79(3):1409–1424. 13, 16, 21

Groothuis, S. S., Rusticelli, G., Zucchelli, A., Stramigioli, S., and Carloni, R. (2012). The vsaUT-II: A novel rotational variable stiffness actuator. In *Proceedings of the International Conference on Robotics and Automation, St. Paul, USA*, pages 3355–3360. IEEE Robotics and Automation Society. 7

Groothuis, S. S., Stramigioli, S., and Carloni, R. (2013). Lending a helping hand: toward novel assistive robotic arms. *IEEE Robotics and Automation Magazine*, 20(1):20–29. 115

Harmonic Drive AG (2012). www.harmonicdrive.de/english/downloads/catalogues. 92, 93

Hasan, Z. (1986). Optimized movement trajectories and joint stiffness in unperturbed, inertially loaded movements. *Biological Cybernetics*, 53(6):373–382. 81

Heitler, W. (1974). The locust jump. *Journal of comparative physiology*, 89(1):93–104. 117

Hill, A. V. (1938). The heat of shortening and the dynamic constants of muscle. *Proceedings of the Royal Society of London Series B-Biological Sciences*, 126(843):136–195. 12

Hogan, N. (1984). Adaptive control of mechanical impedance by coactivation of antagonist muscles. *Transactions on Automatic Control*, 29(8):681–690. 8, 12, 21, 26, 115

Hogan, N. (1985). Impedance control - an approach to manipulation 1. theory. *Journal of Dynamic Systems Measurement and Control-Transactions of the ASME*, 107(1):1–7. iii, 1, 4, 96

Honda (2008). Walking Assist Device. http://corporate.honda.com/innovation/walk-assist/. 4

Hoult, W. and Cole, D. J. (2008). A neuromuscular model featuring co-activation for use in driver simulation. *Vehicle System Dynamics*, 46(1):175–189. 8, 75

Hu, X., Murray, W. M., and Perreault, E. J. (2011). Muscle short-range stiffness can be used to estimate the endpoint stiffness of the human arm. *Journal of Neurophysiology*, 105(4):1633–1641. 22

Humphrey, D. R. and Reed, D. J. (1983). Separate cortical systems for control of joint movement and joint stiffness: reciprocal activation and coactivation of antagonist muscles. *Motor Control Mechanisms in Health and Disease*, 39(1):347–372. 21, 81

Hurst, J. W., Chestnutt, J. E., and Rizzi, A. A. (2004). An actuator with physically variable stiffness for highly dynamic legged locomotion. In *Proceedings of the International Conference on Robotics and Automation*, volume 5, pages 4662–4667. IEEE Robotics and Automation Society. 6

Johannes, M. S., D.Bigelow, J., Burck, J. M., Harshbarger, S. D., Kozlowski, M. V., and van Doren, T. (2011). An overview of the developmental process for the modular prosthetic limb. *Johns Hopkins APL Technical Digest*, 30(3):207–216. 3

Kadiallah, A., Franklin, D. W., and Burdet, E. (2012). Generalization in adaptation to stable and unstable dynamics. *PLoS One*, 7(10):e45075. 120

Kandel, E., Schwartz, J., and Jessell, T. (2000). *Principles of Neural Science.*, pages 714–736. McGraw-Hill Medical,4 edition. 73, 76

Katayama, M. and Kawato, M. (1993). Virtual trajectory and stiffness ellipse during multijoint arm movement predicted by neural inverse models. *Biological Cybernetics*, 69(5):353–362. 18, 24

Kearney, R. E. and Hunter, I. W. (1990). System identification of human joint dynamics. *Critical Reviews in Biomedical Engineering*, 18(1):55–87. 21

Kistemaker, D. and Rozendaal, L. (2011). In vivo dynamics of the musculoskeletal system cannot be adequately described using a stiffness-damping-inertia model. *PLoS ONE*, 6(5). 21

Lacquaniti, F., Licata, F., and Soechting, J. F. (1982). The mechanical behavior of the human forearm in response to transient perturbations. *Biological Cybernetics*, 44(1):35–46. 18, 19

Laffranchi, M., Tsagarakis, N., and Caldwell, D. (2011). A compact compliant actuator (compact™) with variable physical damping. In *Proceedings of the International Conference on Robotics and Automation*, pages 4644–4650. IEEE Robotics and Automation Society. 7

Laffranchi, M., Tsagarakis, N., and Caldwell, D. (2012). CompAct Arm™: a Compliant Manipulator with Intrinsic Variable Physical Damping . In *Proceedings of Robotics: Science and Systems*, Sydney, Australia. 7

Latash, M. L. (2008). *Neurophysiological Basis of Movement. Second Edition.*, pages 67–72. Human Kinetics: Urbana, IL. 76

Latash, M. L. and Zatsiorsky, V. M. (1993). Joint stiffness: Myth or reality? *Human Movement Science*, 12. 22

Liberating Technologies, Inc. (2012). LTI Boston Arm Systems. http://www.liberatingtech.com. 3

Lobontiu, N. (2010). *System Dynamics for Engineering Students: Concepts and applications*. Academic Press, New York, NY, USA, 1st edition. 104

Mason, M. (1981). Compliance and force control for computer controlled manipulators. *IEEE Transactions on Systems, Man and Cybernetics*, SMC-11(6):418–432. 4

Maxon Motor AG (2012). www.maxonmotor.com/maxon/view/catalog/. 93, 101

McIntyre, J. and Bizzi, E. (1993). Servo hypotheses for the biological control of movement. *Journal of Motor Behavior*, 25(3):93–202. 77

Migliore, S. A., Brown, E. A., and DeWeerth, S. P. (2005). Biologically inspired joint stiffness control. In *Proceedings of the International Conference on Robotics and Automation.*, pages 4508–4513. IEEE Robotics and Automation Society. 6

Migliore, S. A., Brown, E. A., and DeWeerth, S. P. (2007). Novel nonlinear elastic actuators for passively controlling robotic joint compliance. *Journal Of Mechanical Design*, 129(4):406–412. 8

Mileusnic, P. M. and Loeb, G. E. (2006). Mathematical Models of Proprioceptors. II. Structure and Function of the Golgi Tendon Organ. *Journal of Neurophysiology*, 96(4):1789–1802. 78

Milner, T. E. (1993). Dependence of elbow viscoelastic behavior on speed and loading in voluntary movements. *Experimental Brain Research*, 93(1):177–180. 81, 83, 112, 120

Milner, T. E. and Cloutier, C. (1998). Damping of the wrist joint during voluntary movement. *Experimental Brain Research*, 122(3):309–317. 21, 23

Mitrovic, D., Klanke, S., Osu, R., Kawato, M., and Vijayakumar, S. (2009). Impedance control as an emergent mechanism from minimising uncertainty. 9

Murray, W. M., Buchanan, T. S., and Delp, S. L. (2000). The isometric functional capacity of muscles that cross the elbow. *Journal of Biomechanics*, 33(8):943–952. 19, 73

Murray, W. M., Delp, S. L., and Buchanan, T. S. (1995). Variation of muscle moment arms with elbow and forearm position. *Journal of Biomechanics*, 28(5):513–525. 16

Paskarbeit, J., Annunziata, S., Basa, D., and Schneider, A. (2013). A self-contained, elastic joint drive for robotics applications based on a sensorized elastomer coupling - design and identification. *Sensors and Actuators A: Physical*, 199:56–66. 85, 88, 89

Popescu, F., Hidler, J. M., and Rymer, W. Z. (2003). Elbow impedance during goal-directed movements. *Experimental Brain Research*, 152(1):17–28. 21

Pratt, G. and Williamson, M. (1995). Series elastic actuators. *Proceedings of the IEEE/RSJ International Conference on Intelligent Robots and Systems*, 1:399–406. 6

Raphael, G., Tsianos, G. A., and Loeb, G. E. (2010). Spinal-like regulator facilitates control of a two-degree-of-freedom wrist. *Journal of Neuroscience*, 30(28):9431–9444. 70

Readman, M. C. (1994). *Flexible Joint Robots*. CRC press, Inc, New York. 5

Richardson, A., Tresch, M., Bizzi, E., and Slotine, J.-J. (2005). Stability analysis of nonlinear muscle dynamics using contraction theory. In *Proceedings of the 27th Annual IEEE Engineering in Medicine and Biology Conference*, pages 4986–4989. 70

Sardellitti, I., Medrano-Cerda, G., Tsagarakis, N., Jafari, A., and Caldwell, D. (2012). A position and stiffness control strategy for variable stiffness actuators. In *International Conference on Robotics and Automation*, pages 2785–2791. IEEE. 7

Sardellitti, I., Palli, G., Tsagarakis, N. G., and Caldwell, D. G. (2010). Antagonistically actuated compliant joint: Torque and stiffness control. In *IEEE/RSJ International Conference on Intelligent Robots and Systems*, pages 1909–1914. 7, 121

Serres, S. J. and Milner, T. E. (1991). Wrist muscle activation patterns and stiffness associated with stable and unstable mechanical loads. *Experimental Brain Research*, 86(2):451–458. 21

Shadmehr, R. and Wise, S. P. (2005). *The Computational Neurobiology of Reaching and Pointing: A Foundation for Motor Learning*. MIT Press, Cambridge MA. 76

Siciliano, B. and Khatib, O., editors (2008). *Springer Handbook of Robotics*, pages 165–166. Springer, Berlin, Heidelberg. 5, 22

Smith, A. M. (1996). Does the cerebellum learn strategies for the optimal time-varying control of joint stiffness? *Behavioral and Brain Sciences*, 19(3):399–410. 79

Stroeve, S. H. (1999). Impedance characteristics of a neuromusculoskeletal model of the human arm I. Posture control. *Biological Cybernetics*, pages 475–494. 24

Suzuki, M., Shiller, D. M., Gribble, P. L., and Ostry, D. J. (2001). Relationship between cocontraction, movement kinematics and phasic muscle activity in single-joint arm movement. *Experimental Brain Research*, 140(2):171–181. 8, 21, 81, 83, 120

Taghirad, H. and Bélanger, P. (1998). Modelling and parameter identification of harmonic drive systems. *Journal of dynamic systems, measurement, and control*, 120(4):439–444. 89

Tonietti, G., Schiavi, R., and Bicchi, A. (2005). Design and control of a variable stiffness actuator for safe and fast physical human/robot interaction. In *Proceedings of the International Conference on Robotics and Automation*, pages 526–531. IEEE. 6

Townsend, W. and Salisbury, J., J. (1987). The effect of coulomb friction and stiction on force control. In *Robotics and Automation. Proceedings. 1987 IEEE International Conference on*, volume 4, pages 883–889. 94

Tsai, L. W. (1999). *Robot Analysis and Design: The Mechanics of Serial and Parallel Manipulators*. John Wiley & Sons, Inc., New York, NY, USA, 1st edition. 94

Vallery, H., Ekkelenkamp, R., van der Kooij, H., and Buss, M. (2007). Passive and accurate torque control of series elastic actuators. In *Intelligent Robots and Systems, 2007. IROS 2007. IEEE/RSJ International Conference on*, pages 3534–3538. 107

Vallery, H., Veneman, J., van Asseldonk, E., Ekkelenkamp, R., Buss, M., and van der Kooij, H. (2008). Compliant actuation of rehabilitation robots. *Robotics Automation Magazine, IEEE*, 15(3):60–69. 4

Virk, G. S. and Nyoman, I. (University of Technology Sydney, Australia, 2013). Exoskeleton for assisting human walking. pages 117–124. 4

Wernholt, E. and Gunnarsson, S. (2005). Nonlinear grey-box identification of industrial robots containing flexibilities. In *Proceedings of the 16th IFAC World Congress*, pages 59–59. 90

Woittiez, R. D., Huijing, P. A., Boom, H. B., and Rozendal, R. H. (1984). A three-dimensional muscle model: a quantified relation between form and function of skeletal muscles. *Journal of Morphology*, 182(1):95–113. 13, 116

Wyeth, G. (2006). Control issues for velocity sourced series elastic actuators. In MacDonald, B., editor, *Australasian Conference on Robotics and Automation*, Auckland. Australian Robotics and Automation Association Inc. 98

Yamazaki, Y., Ohkuwa, T., Itoh, H., and Suzuki, M. (1994). Reciprocal activation and coactivation in antagonistic muscles during rapid goal-directed movements. *Brain Research Bulletin*, 34(6):587–593. 21

Yang, C., Ganesh, G., Haddadin, S., Perusal, S., Albu-Schäffer, A., and Burdet, E. (2011). Human-like adaptation of force and impedance in stable and unstable interactions. *IEEE Transactions on Robotics*, 27(5):918–930. iii, 1, 116

Zajac, F. E. (1989). Muscle and tendon:properties, models, scaling, and application to biomechanics and motor control. *Critical Reviews in Biomedical Engineering*, 17(4):359–411. 12, 13, 14, 37

Zakotnik, J., Matheson, T., and Dürr, V. (2006). Co-contraction and passive forces facilitate load compensation of aimed limb movements. *The Journal of Neuroscience*, 26(19):4995–5007. 117, 118

Zinn, M., Khatib, O., Roth, B., and Salisbury, J. (2004). Playing it safe [human-friendly robots]. *Robotics Automation Magazine, IEEE*, 11(2):12–21. 6, 7, 105

Zollo, L., Siciliano, B., Laschi, C., Teti, G., and Dario, P. (2003). An experimental study on compliance control for a redundant personal robot arm. *Robotics and Autonomous Systems*, 44(2):101–129. 5